UNIVERSITY OF LIVERPOOL

Fast Folding Dynamics of Proteins and Peptides

Thesis submitted in accordance with the requirements of the University of Liverpool for the degree of Doctor of Philosophy by

Renee Peta-Gaye Whynes

9/29/2010

ABSTRACT

The dynamics of protein folding has become a major area of research interest today, particularly in biophysical chemistry. The first steps of protein folding have been reported to occur on the 100-ns time scale, made possible by with the development of several experimental techniques. For this research, laser induced temperature jumps coupled to infrared spectroscopy were used for observing the fast folding dynamics of a small protein and a peptide on the nanosecond time scale by probing changes in the amide I band, which is sensitive to secondary structure. This research project also describes the development and demonstration of a new photochemical triggering technique for protein folding.

Peptide and poly-ethylene glycol-capped gold nanoparticles were tested and used as heat transducers for inducing temperature jumps in protein and peptide samples. The results demonstrate that, for the typical concentration used in our temperature jump measurements, the nanoparticles do not affect the helix-coil transition of proteins and peptides. We also describe a new method for subtracting the pressure relief artifact observed after a ns-temperature jump. Application of this method allows us to identify a hidden phase on the nanosecond time scale in the temperature jump induced dynamics of a small protein.

The effect of pD and temperature on the fast folding dynamics of a small protein (BBL) was studied. The results show, for the first time, that the protein exhibits three distinct phases; two nanosecond phases and a microsecond phase. However, we found that the nanosecond components are not easily distinguished due to similarities in the time constants.

Finally, this research project also describes the development of a new photo-triggering method which is based on a photocleavage reaction that generates the desired functional group from an inactive caged one upon photolysis, namely the photocleavage reaction of a peptide that is covalently bonded to 4,5-dimethoxy-2-nitrobenzyl. Our experimental results show, that cleavage of the backbone peptide is very fast, so that the photo-triggering technique is valid for observing the fast dynamics of peptides and proteins on the nanosecond/microsecond timescale.

ACKNOWLEDGEMENTS

I can remember my dad saying, “Of all the things in life, knowledge, wisdom and understanding should be the essence of life.” Inspired by these words I am trying to lead a life of wisdom and understanding the phenomenon of life.

I would first like to thank God for this accomplishment. I would never have finished this journey without his unseen love and compassion. I would then like to thank my parents for their love and support. They have been very supportive throughout my PhD years.

I would like to thank my supervisor Dr. Martin Volk for letting me be a part of his research group. He has been very encouraging, cooperative and patient with me over the 4 years of my research work. He once told me that I came too far to quit and that a quitter never wins. Those words meant so much to me.

Thanks to Dr. Eyal Arbely, Dr. James Gaynor and Dr. Jaroslava Mikšovská for their collaboration.

I would like to thank my group, Chris and Teresa for their help and friendship. They have been very helpful and supportive throughout the 4 years of my PhD. Also, I am happy for the many friends I have made at the university, especially Natalia. You all have been a substantial source when all seems down and out. I would also like to thank my friend Dr. Titi Aina for been a true friend over the years. Her constant motivation helped me to see the light at the end of the tunnel.

Finally, I would like to thank Kenny for been there all the way with his shoulders for me to cry on, even across the Atlantic Ocean. He’s always there no matter the time to answer my calls and listen to my constant whining…failed experiments, no motivation, bad weather, tired…the list goes on and on. Thank you so much for your patience! It meant so much to me!

Last but not least, a huge thank you to my brothers and sisters. Thank you all for your encouragements.

ABBREVIATIONS

CALNN	
CT_8	
3-D	Three Dimensional
AR_4	$Ac\text{-}AAAAA\text{-}(AAARA)_4A\text{-}NH_2$
ATP	Adenosine 5′-Tri-Phosphate
BBL	GSQNNDALSPAIRRLLAEHNLDAAIKGTGVGGRLTREDVEKHLAKA
BF	Basic Fuchsin
BG	Background
CaF_2	Calcium Fluoride
CD	Circular Dichroism
CMBA	4-Chloro-2-Nitrobenzaldehyde
CV	Crystal Violet
cw-IR	Continuous Wave Infrared
DMBA	4,5-Methoxy-2-Nitrobenzaldehyde
FMNA	4-Formyl-6-Methoxy-3-Nitrophenoxyacetic Acid
FT-IR	Fourier Transform Infrared Spectroscopy
FWHM	Full Width Half Maximum
IC	Internal Conversion
LFP	Laser Flash Photolysis
MCT	Mercury Cadmium Telluride
NBA	o-Nitrobenzaldehyde
NMA	N-methylacetamide
Nd:YAG	Neodeyium: Yttrium Aluminium Garnate
NP	Nanoparticle
PAC	Photo-Acoustic Calorimetric
PEG	Poly-Ethylene Glycol
pNIPAM	poly(n-isopropylacrylamide)
RF	Radio Frequency
TJ	Temperature Jump
TR-IR	Time Resolved Infrared Spectroscopy

TFA	Trifluoroacetic Acid
UVRR	Ultraviolet Resonance Raman
UV/vis	Ultraviolet/visible

Table of Contents

List of Figures

List of Tables

List of Schemes

CHAPTER 1: INTRODUCTION

1.1 Background

Proteins and peptides are essential in biological processes[1, 2]. They are polymers of amino acids linked by amide bonds between the amino group of one amino acid and the carboxyl group of the neighboring amino acid. It is well known that proteins are synthesized by polymerization of the amino acids in the order specified by the sequence of nucleotides in a gene. However, this sequence of amino acid could fold into many different structures, but only one will give rise to the functional protein. Even though a protein can achieve many different conformations, most proteins fold rapidly into their native state. In 1960, Levinthal[3] demonstrated that if a protein consists of a polypeptide chain of 100 residues, it would take ~10^{50} years to randomly acquire all the possible conformations to find its folded structure. However, the observed timescale on which many proteins fold to their native conformations are on the order of a few seconds or even faster. Therefore, the question still remains how a protein folds to its native structure.

Protein structures are very complex and for this reason they are classed into four levels of structural organization: their primary, secondary, tertiary and quaternary structure. The primary structure is the chemical structure of the polypeptide chain, i.e. the sequence of amino acids, and the secondary structure is the local spatial arrangement (stabilized by hydrogen bonds) of the polypeptide backbone. For more structural complexity, the tertiary structure refers to the three-dimensional structure of the entire polypeptide and the quaternary structure refers to the association of two or more peptide chains in the complete protein[1, 2].

It is widely believed that the first stage of a protein folding to its full structure is the formation of secondary structure (α-helices, β-sheets and turns). Mutations in the secondary structure of proteins cause a variety of neurological diseases, such as Alzheimer's, Prion, cystic fibrosis, and Parkinson disease[2, 4-10]. Therefore, understanding the dynamics of the protein folding process may provide insights into why these diseases occur. With this in mind, protein folding has become a topic of interest in recent years.

The protein folding process is very complex; the investigation of how proteins obtain their unique native conformation has resulted in the development of several models. These models include the framework model, the hydrophobic collapse model, and the nucleation condensation model.

The framework model was proposed by Ptitsyn in 1973[11]. Experimental observations indicate that protein folding begins with the formation of local secondary structure (α-helices, β-sheets and turns). The secondary structural elements then assemble into tertiary structure by diffusion and collision.

Another model suggested is the hydrophobic collapse model[12-14]. The initial stage of protein folding in the hydrophobic collapse model is extremely rapid and consists of a uniform collapse of the polypeptide by burying the hydrophobic side chains. The hydrophobic side chains are directed towards the interior of the peptide and the water molecules are expelled from its hydrophobic core[15]. The secondary structure and tertiary structure are formed within the compact aggregate on the short time scale.

Finally, the nucleation condensation model was developed by Fersht in the mid 1990's[16, 17]. The initial stage, the formation of a semi-stable protein folding nucleus with native secondary structure by only a few residues, is slow. The structure then propagates out from this nucleus, rapidly forming the full structure.

Experimental investigations are required to distinguish between these different models, particularly work on the fastest processes of folding. As stated above, some of this evidence points towards the fast formation of secondary structure and slower final folding, i.e. the framework model, as the dominant mode of folding. This thesis aims to contribute to this growing amount of work on the fastest processes of protein folding.

1.2 Secondary Structure of Proteins and Peptides

As mentioned above, the secondary structure of the peptide or protein is the local arrangement of the amino acid residues in relation to each other, or more specifically, the relative positions of hydrogen bonded N—H groups and C═O groups. The ability of the peptide to adopt different secondary structural motifs is due to freedom of rotation around the backbone bonds to the α-carbon atoms[2].

The main secondary structural features of interest are the α-helix (Figure 1.1), β-sheet (Figure 1.2) and the random coil structure. The α-helix was discovered in 1951 by Linus Pauling through model building[18]. It is normally right-handed with 3.6 residues per turn and a pitch of 5.4 Å. The α-helix shows hydrogen bonding from residue i to residue i+4.

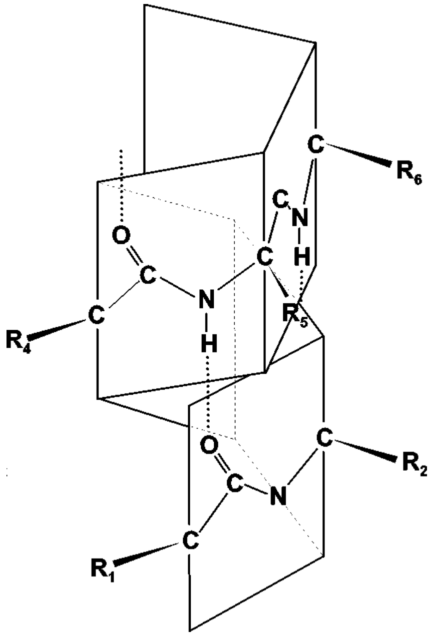

Figure 1. 1: The α-helix configuration[19, 20]. Dotted lines represent hydrogen bonds.

The β-sheet was also discovered by Linus Pauling[18]. β-sheets form intra-peptide hydrogen bonds between residues that are further apart than in the α-helix or between different peptide chains (see Figure 1.2).

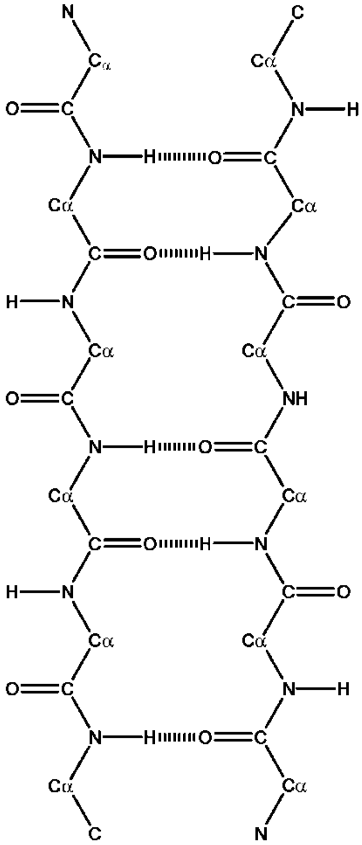

Figure 1. 2: The anti-parallel β-sheet configuration[2]. Dashed lines indicate hydrogen bonds.

Finally, random coil structures do not have any regular hydrogen bonding between amino acid residues and the segments are randomly arranged. Due to the absence of any stabilizing interactions, the polypeptide backbone simply adopts all possible conformations randomly.

1.3 Experimental Techniques for Studying Protein Folding

Fluorescence spectroscopy, circular dichroism (CD) spectroscopy, ultra-violet resonance Raman (UVRR) spectroscopy and infrared (IR) spectroscopy have been used to probe structural changes in proteins and peptides (e.g. during folding). Descriptions of these techniques are given below.

Fluorescence spectroscopy has been used to probe global kinetics of folding and the formation of specific tertiary contacts[21-23]. This technique is particularly useful for proteins with aromatic amino acid residues which function as intrinsic probes and provide a wide range of protein structural and dynamical information. This method relies on an intensity change or a shift of the fluorescence spectrum when the fluorescent group is buried within a folded protein as opposed to being exposed to the surrounding solvent. Alternatively, intra-peptide fluorescence quenching can be used, for example, model peptides which are designed with a tryptophan at position 1 and a histidine at position 5, which quenches the tryptophan fluorescence when the residues are in close contact in the helical configuration[24]. Therefore, fluorescence can provide site specific information about the structure of the protein or peptide.

Circular dichroism (CD) spectroscopy measures the different absorbance of left and right hand circularly polarized light. CD spectroscopy in the far–UV (180 – 240 nm) gives information on the secondary structure of the polypeptide backbone[25-27].

Ultra-violet resonance Raman (UVRR) spectroscopy has been used to study the conformation of proteins and peptides. This is because the frequencies and intensities of the amide vibration bands (I, II, III) and the C_α—H bending vibrations depend on the secondary structure [28-41].

Finally, infrared spectroscopy is widely used for investigating the secondary structure of proteins and peptides[42-50]. This technique is used here since it allows for the observation of structural changes on the nanosecond time scales[51]. Infrared spectra of proteins in aqueous solution are obtained with high signal-to-noise ratio and they contain relatively strong absorption bands associated with the peptide bond.

The infrared spectra of proteins and polypeptides contain 9 characteristic regions which are referred to as the amide bands[52]. The amide I, II and III bands are the major bands of the protein infrared spectrum. In this research, the amide I band will be used, since its absorbance is stronger than that of amide III and better characterized than the amide II.

The amide I band is the result of the carbonyl stretch (C═O) coupled to a C—N stretch and an in-phase N—H bend. These account for 75%, 10%, and 15% of the vibrational energy, respectively. The amide I vibration is sensitive to solvent and intrapeptide hydrogen bonding of the backbone carbonyl and amide groups and inter-residue coupling[52] which makes the amide I band sensitive to secondary structure. Another fundamental mechanism that causes the amide I vibration sensitive the secondary structure is transition dipole coupling. Transition dipole coupling is a resonance interaction between the oscillating dipoles of neighboring amide groups and the coupling depends upon their relative orientation and their distance[53]. Transition dipole coupling has two effects, namely exciton transfer and exciton splitting. Also, the amide I vibrations are sensitive to local electric field which leads to field induced changes in the IR absorption spectrum. This field induced changes is known as the vibrational stark effects[54].

The position of the amide I band has been shown to be invariant to the exact organic solvent used, provided that the secondary structure is unchanged[55]. However, this is not the case when proteins are in an aqueous medium. The nature of the intrapeptide hydrogen bond is altered when the peptide is dissolved in water, and the solvent has access to the backbone; it is no longer a linear bond. Also, water has a strong absorption in the infrared region that overlaps the amide I band. For this reason, proteins are normally prepared in D_2O solution where the overlapping aqueous band is shifted to lower frequencies in the infrared spectrum. But complications still arise on the dissolution of the peptide in D_2O in which hydrogen/deuterium (H/D) exchange of solvent accessible amide protons takes place. Since deuterium is heavier than hydrogen, the N-D bending vibration is slower and does not couple effectively to the carbonyl stretch vibrations, altering the nature of the amide I vibration. Thus, the amide I′ band (where ′ refers to the deuterated form of the peptide) is positioned at lower frequencies. Another factor contributing to this shift against the frequencies observed in organic solvents is the solvation effect due to the formation of deuterium bonds between the peptide and the solvent.

The position of the amide I band can be assigned to a particular secondary structure (α-helix, β-sheet, or turn) based on findings reported in literature[48, 51, 52, 56-64] (see Table 1.1).

Table 1. 1: Frequency assignments for the amide I′ band in D_2O of the most common secondary structures found in proteins and peptides

Assignment	Wavenumbers (cm^{-1})	References
α-helix	1626 - 1645	48, 51, 52, 55-61, 63
β-sheet	1629, 1675	48, 61, 64
random coil	1642 - 1655, 1665 - 1675	48, 59, 60, 63, 64
3_{10}-helix	1637	32
β-turn	1668, 1675,1686	48, 64

In some helical peptides, the amide I′ band was found to have contributions at 1654 cm^{-1} and between 1630 and 1640 cm^{-1}. Both were assigned to the α-helix. This is because some of the amide protons were exposed to the solvent, and underwent H/D exchange, causing the amide I′ to shift to lower frequencies. However, certain protons are not accessible to solvent and thus their amide I vibration remains at the higher frequency[51, 65].

Furthermore, evidence also suggests that the position of the amide I band is dependent on temperature. Graff et al[59] showed that a shift of the α-helical amide I band of 0.1 $cm^{-1}/^{o}C$ occurs upon heating and a similar increase in the frequency of the random coil absorbance band.

1.4 Methods for Initiating Protein Folding

Understanding the dynamics of the folding process is important for elucidating the mechanism by which protein folding proceeds. For this reason, several methods have been developed over the years for the fast initiation of the (un)folding process.

Early methods used for fast initiation of protein folding are stopped-flow or rapid mixing techniques. These methods work by rapidly changing the concentration of denaturant or by altering the pH of the solution. While these techniques are applicable for any protein or peptide, the rapid mixing or stopped-flow techniques limit these studies to the ms-timescale and thus cannot be used to study the α-helix unfolding of proteins and peptides which occurs much faster, on the ns- and µs-time scale. Thus, considerable effort was made to improve the time resolution to ~45 µs using a continuous-flow technique[66-68]. However, this technique is still not fast enough to study fast protein folding.

Relaxation techniques such as dielectric relaxation and ultrasonic attenuation generally involve the change of an extrinsic variable such as pressure. These techniques were used in earlier studies to investigate the helix – coil transition of α-helical homopolymers, yielding relaxation time constants in the range of ns to ms[69-71]. However, these methods provide only indirect conclusions on the folding dynamics of proteins.

Photochemical trigger methods have also been used to trigger folding and unfolding of peptides and proteins. These methods include photodissociation of carbon monoxide from a heme cofactor[72], electron transfer to a heme[73], pH jump[74], azobenzene isomerisation[75] and photodissociation of an aromatic disulfide bond[54, 76]. These techniques have the advantage of initiating protein folding on a fast timescale (ps) using short laser flashes. Nevertheless, these methods are highly specialized and can only be applied to specific proteins.

The development of a new photo-triggering method which is based on a photocleavage reaction that generates the desired functional group from an inactive caged one upon photolysis[77, 78] is investigated in this thesis. Tatsu et al[79] and more recently by Rhee et al[80] studied the photocleavage reaction of a peptide backbone caged with a nitrobenzyl derivative (see further discussion in Chapter 5 of this thesis). In this research we determine whether this technique based on a nitrobenzyl-caged peptide backbone is a suitable method for initiating fast protein folding processes.

A fast temperature jump method is another technique that allows for the fast initiation of protein folding/unfolding. For laser-induced temperature jumps, a short laser pulse is focused into the sample. The laser pulse energy is absorbed by an inert dye which undergoes fast internal conversion or directly by the solvent and generates a homogenous increase of the temperature on the time scale of the laser pulse (nanoseconds). The major advantage of temperature jumps over the other methods are that protein folding dynamics can be observed under native conditions and that the method relies on temperature-induced folding or unfolding, and is consequently applicable to a broad range of proteins or peptides[58, 81-84]. Temperature jumps combined with a variety of spectroscopic techniques, such as ultraviolet resonance Raman (UVRR) spectroscopy[32-35], fluorescence spectroscopy[24, 85, 86], and time resolved infrared (TR-IR) spectroscopy[64, 87-91] have been used to directly observe the fast folding dynamics of proteins and peptides. In this thesis, temperature jumps coupled with TR-IR spectroscopy were used to study the fast folding dynamics of an alanine-based peptide, AR_4 (Chapter 3) and a small protein, WT-BBL (Chapter 4).

1.5 Outlook on Thesis

This thesis provides details of the fast folding dynamics of a protein and the dynamics of the photoreaction of a peptide backbone caged with a nitrobenzyl derivative. Furthermore, it was shown that gold nanoparticles are good heat transducers for the induction of laser-pulse induced temperature jumps.

In detail, the thesis addresses the following:

Chapter 2 gives a detailed description of the temperature jump setup used for carrying out this PhD work. In addition, Chapter 2 describes a new method for subtracting the pressure relief artifact observed after temperature jumps, especially at higher temperatures. A detailed description of the method used for data analysis is also given.

Chapter 3 describes the use of indirect heating for inducing temperature jumps. This chapter for the first time introduces the use of gold nanoparticles as fast heat transducers. We also studied the effect of the presence of gold nanoparticles on the folding dynamics of a short alanine-based peptide.

In Chapter 4, we used the temperature jump technique coupled with TR-IR spectroscopy to obtain information on the folding dynamics of the WT-BBL protein.

In Chapter 5, we studied the photocleavage reaction of a peptide backbone covalently bonded to 4,5-dimethoxy-2-nitrobenzyl for triggering fast protein folding. This chapter provides dynamic results on the release rate of the backbone caged peptide from the 2-nitrobenzyl derivative.

CHAPTER 2: EXPERIMENTAL SETUP

2.1 Temperature Jump Setup

2.1.1 Pump Laser

Temperature jump measurements were undertaken using a Quantel Brilliant nanosecond Q-switched 10 Hz Nd:YAG laser with a pulse duration of 5 ns. The Nd:YAG laser has the capability of delivering ~360 mJ at 1064 nm, ~180 mJ at 532 nm and ~90 mJ at 355 nm. The Nd:YAG laser is one of the most widely used solid state lasers. The active medium is a host crystal of yttrium aluminum garnet which contains neodymium ions (Nd^{3+}) which are pumped by a flash lamp. This system is advantageous over others, being a four level laser, which makes it possible to easily achieve population inversion. The Nd:YAG laser cavity is fitted with a Q-switch that allows for the build-up of high population inversion when the switch is closed. When the switch is opened, the built-up energy is suddenly released and converted into a laser pulse of high energy but short duration.

The Nd:YAG laser operates at a wavelength of 1064 nm, which is frequency doubled to give an intense pulse at 532 nm by passing through crystalline potassium dihydrogen phosphate (KDP). The 532 nm light is referred to as the second harmonic (SH). The high intensity IR light drives the lowest order non-linear polarizability of the KDP crystal so that coherent light at double the frequency/half the wavelength is emitted.

The third harmonic (355 nm) is also used during my experimental investigation. This frequency can be achieved by doubling followed by sum frequency generation of both waves in another KDP crystal.

2.1.2 Pump Beam: Temperature Jump Induction

A schematic of the temperature jump set up and the optics are shown in Figure 2.1 and Table 2.1, respectively. The beam leaving the Nd:YAG laser at 1064 nm is converted to 532 nm and reflected by mirror 3 (M3), mirror 4 (M4) and mirror 5 (M5). A beam splitter is then used to split the incoming beam in two halves by passing ~50% of the light (beam 1) and reflecting ~50% of the light (beam 2). Beam 1 from the beam splitter is focused by Lens 4 (L4) which focuses the beam just before the sample while beam 2 is reflected by mirror 6 (M6) and mirror 7 (M7) onto Lens (L5). L5 focuses the beam behind the sample. The two beams are collinear and are located at the same position in the sample cell for homogeneous heating of the sample and they are almost parallel to the probe beam. The energy at the sample (sum of beam 1 and beam 2) is ~1.5 mJ. It is important to mention that the pulse energies from beam 1 and beam 2 were adjusted so the induced temperature jump (ΔT) is identical for both beams. This was done by placing glass slides either before L4 or M6. The laser light energy is absorbed into the sample by heat transducing dye molecules, peptide-capped gold nanoparticles (CALNN-NP and CT_8-NP) or poly-ethylene glycol-capped gold nanoparticles (PEG-NP) (see Chapter 3).

When the third harmonic is used for the investigation of photochemical reactions of a nitrobenzyl moiety (see Chapter 5), only a single beam (beam 1) was used to induce absorbance changes in the sample. The approximate energy at the sample is ~0.6 mJ.

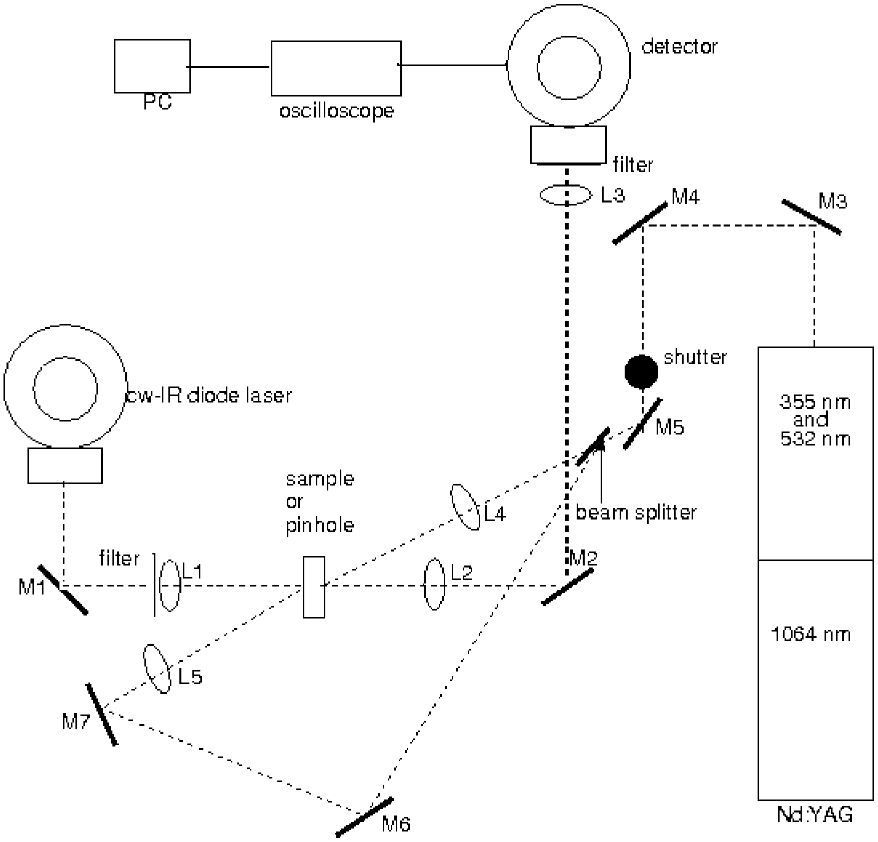

Figure 2. 1: Schematic representation of pump-probe laser temperature jump setup

Table 2. 1: Specification of optics used in temperature jump setup

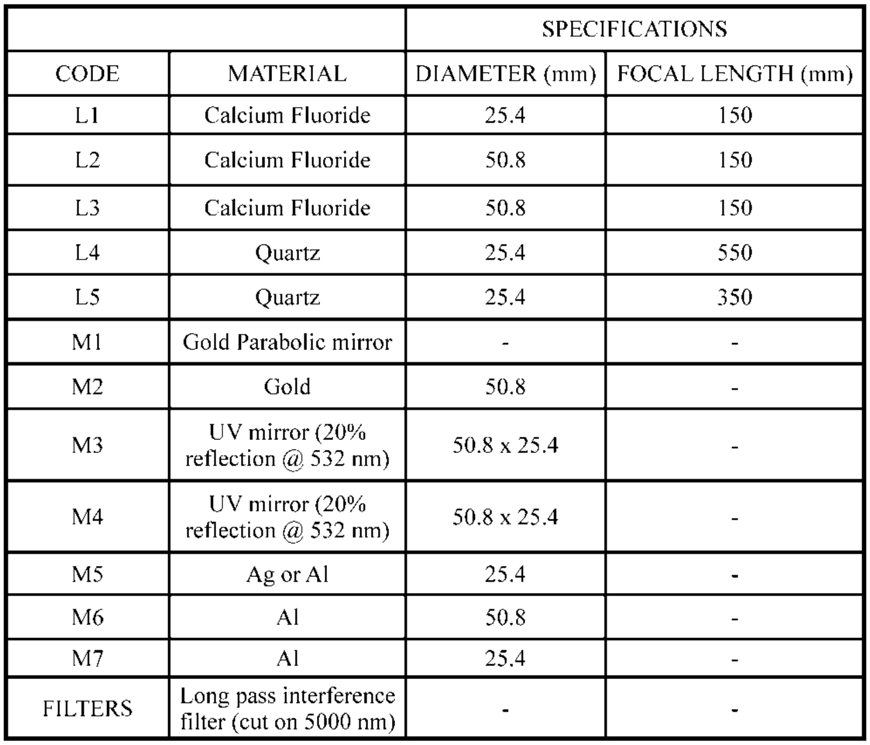

		SPECIFICATIONS	
CODE	MATERIAL	DIAMETER (mm)	FOCAL LENGTH (mm)
L1	Calcium Fluoride	25.4	150
L2	Calcium Fluoride	50.8	150
L3	Calcium Fluoride	50.8	150
L4	Quartz	25.4	550
L5	Quartz	25.4	350
M1	Gold Parabolic mirror	-	-
M2	Gold	50.8	-
M3	UV mirror (20% reflection @ 532 nm)	50.8 x 25.4	-
M4	UV mirror (20% reflection @ 532 nm)	50.8 x 25.4	-
M5	Ag or Al	25.4	-
M6	Al	50.8	-
M7	Al	25.4	-
FILTERS	Long pass interference filter (cut on 5000 nm)	-	-

2.1.3 Optimization of Pump Beam

The pump beam is the beam leaving the Nd:YAG laser. To ensure that the probe beam is focused tightly on the center of the pump beam, the pump beam was adjusted to be ~10 times larger than that of the probe beam focus (~50 µm). This was done by adjusting the positions of L4 and L5. The pump beam diameter was measured by means of the razor blade method.

The razor blade was placed on a mount at the sample position. The razor blade was moved in 50 µm steps in the horizontal or vertical direction and the intensity of the transmitted pump beam was measured using a silicon diode detector (Thorlabs, Det210, rise time 1 ns) at each position. The first derivative of the signal was plotted to obtain the shape of the pump beam profile. These same measurements were done for beam 2 to obtain its profile. The full width half-maximum (FWHM) of the horizontal and vertical profile for beam 1 was 660 and 570 µm, respectively (see Figure 2.2) at the sample position. The beam profile for beam 2 is similar to that of beam 1; hence the results are not shown.

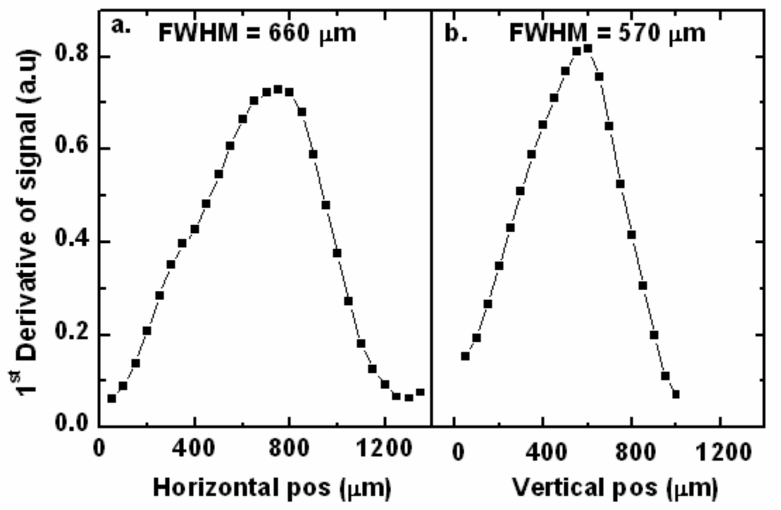

Figure 2. 2: Horizontal (a.) and vertical (b.) profiles of the pump beam for beam 1. See text for method.

2.1.4 Probe Laser

The schematic of the temperature jump setup shown above includes the probe laser setup. The beam leaving the cw-IR tunable lead salt diode laser (Mütek TLS 150, 1560 – 1640 cm^{-1}) is collimated by a parabolic mirror (M1). This mirror is essential because it avoids spherical and chromatic aberrations that would distort the beam and because the beam diverges rapidly after leaving the chip of the laser. The collimated beam from the parabolic mirror is focused by Lens (L1) into the sample. The beam is then collimated by L2 and is reflected by mirror 2 (M2) through Lens 3 (L3) into the detector (see chapter 2.1.7). The intensity of the beam is recorded in the oscilloscope and transferred to the computer for analysis.

The emission spectra of the probe laser were calibrated using a Mattson Galaxy (model number: GL-5020 E) FT-IR spectrometer which was placed on the optical table next to the probe laser. Below is a schematic of the setup.

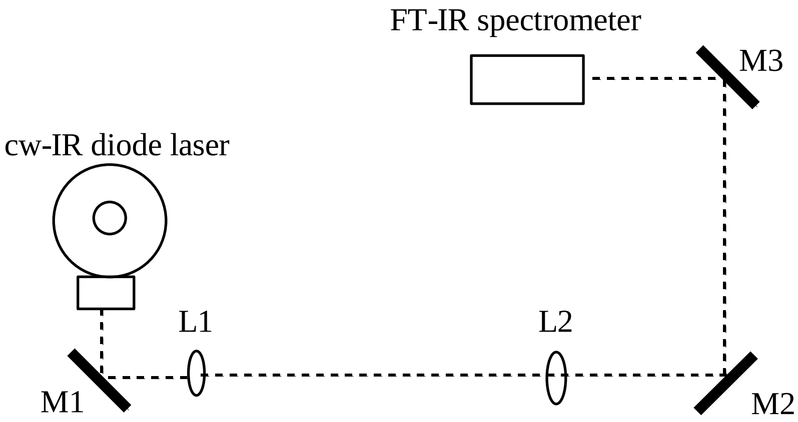

Figure 2. 3: Schematic of the calibration setup

For our calibration purposes, the resolution of the FT-IR spectrometer was set to 1 cm^{-1}. As shown in the diagram above, it was ensured that the tunable cw-IR diode laser beam was focused on the FT-IR detector inside the spectrometer by adjustment in M2 and M3. The IR diode laser beam was coupled into the spectrometer collinear with the HeNe tracer beam after removal of the spectrometer cover and the globar IR source. The emission range of the cw-IR diode laser was measured by the FT-IR spectrometer. Here, the diode laser was tuned to the maximum current (529 mA) and the temperature varied from 80 K to 103 K (0.1 K steps). The emission spectra of the cw-IR diode laser were recorded for each setting and the best single modes at a range of wavelengths were selected for use in the time-resolved experiments.

2.1.5 Optimization of Probe Beam

The probe beam is the beam leaving the cw-infrared diode laser. A high beam quality is important when a small focus of the beam is required. A pinhole was used for optimizing the probe beam. This was to ensure that the probe beam diameter is significantly smaller than the pump beam diameter.

Before fixing the 100 µm pinhole in place, the maximum detector signal was obtained for the standard wavelength 1631 cm^{-1} to be ~800 mV by adjustment of M2 and L3. The intensity of the beam going to the detector had to be reduced because the detector should not be used above 300 mV due to detector non-linearity[92]. The pinhole was then placed in the position of the sample and adjusted with micrometer screws in the horizontal and vertical position followed by fine adjustment of M2 and L3 until the maximum signal was transmitted. After the maximum signal was obtained, the 100 µm pinhole remained in place for the optimization of the probe beam profile.

L1 was used to focus the beam onto the pinhole/sample. It is fitted with micrometer screws in the x, y and z direction (where z is along the beam path). The position of L1 was optimized by changing the micrometer screws in the z direction (in 500 µm steps) and slight adjustment in the x and y direction as well as fine adjustments of M2 and L3. It was found that the optimum z position of L1 (i.e. maximum transmission through the pinhole) at 1584 cm^{-1} was ~1.2 mm closer to the sample than at 1631 cm^{-1}. With this in mind, to achieve optimum focusing of the probe beam onto the sample, for all the wavelengths ranging from 1570 cm^{-1} to 1640 cm^{-1}, the z-position of L1 (along the beam) had to be adjusted when changing the wavelength, where the correct position was obtained by linear interpolation of the 1584 and 1631 cm^{-1} settings .

The beam profile for the optimum position of L1 was obtained using the razor blade method. The razor blade was moved across the beam at the sample position in 10 µm steps and the detector signal was measured and recorded. The first derivative of the signal measured was taken and plotted to obtain the beam profile. The full width at half-maximum (FWHM) at 1631 cm^{-1} was 40 and 51 µm for the horizontal and vertical position, respectively (see Figure 2.4).

The beam profiles were also tested at different distances from the focus. This was done by changing the z-position of L1 to 1 mm and 2 mm closer and away from the razor blade, respectively (results not shown). It was found that the FWHM in the horizontal and vertical direction was measurably larger for 2 mm away from the optimum position of L1.

Profiles were also taken at 1584 cm^{-1} (results not shown). The shape and size of the probe beam profile were similar to the probe beam profile at 1631 cm^{-1}.

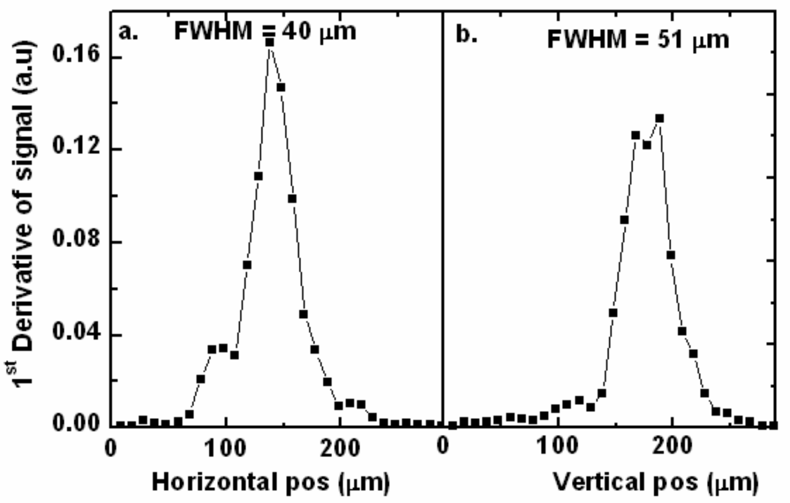

Figure 2. 4: Horizontal (a.) and vertical (b.) profiles of the probe beam at the sample for the optimum position of L1 at 1631 cm^{-1}.

2.1.6 Overlap of Pump and Probe Beam

In doing temperature jump measurements, it is important to have a good overlap between the pump and the probe beam. This is to ensure that the probed sample volume is homogeneously heated. Initially, it is ensured that the diameter of the pump beam is significantly larger than that of the probe beam (see chapters 2.1.3 and 2.1.5). Once this was achieved, optimizing the pump/probe overlap was easily achieved.

Firstly, a 100 µm pinhole was placed on a mount that was fitted with micrometer screws (used for fine adjustment of pinhole) in the x and y directions. The pinhole was moved in small steps until the IR beam was transmitted. Once this was achieved, beam 1 from the YAG laser was positioned on the pinhole by adjustment in L4. By doing so, a rough overlap was obtained for the pump and the probe beam.

Secondly, the pinhole was removed and the sample was put in its place. With beam 2 blocked, the size of the temperature jump was optimized by fine adjustment of M5 and L4 for beam 1. Finally, beam 2 was unblocked and its alignment optimized with M7 until the size of the temperature jump was at its maximum.

2.1.7 Detection

The IR signal is collected for detection by a liquid-N$_2$-cooled fast mercury cadmium telluride (MCT) detector (Kolmar KMPV50-0.5-J2, rise time 15 ns (see below)). The responsivity of the detector is constant when light below a certain intensity is absorbed; above this, saturation causes a decrease in the detector responsivity. A method was developed by Pozo Ramajo[92] to test the linearity of the detector. The results showed that the detector is not linear when the signal is higher than 300 mV. Therefore, in doing temperature jump measurements, care has to be taken to reduce the signal to below 300 mV. This was done by placing a D_2O sample (50 µm path length) or CaF_2 windows in front of the detector.

Previously, S.A. Petty[19] observed a signal from scattered light impinging on the detector at the moment when the temperature jump was induced. This artifact was minimized by placing long pass interference filters (5000 nm cut-on) before L1 so as to eliminate any of the scattered pump light being focused onto the IR diode laser and after L3 so as to eliminate any of the pump light being focused onto the detector. Even after this addition of filters, an electronic artifact still remains on the 10 ns timescale[19, 20]. This artifact was reduced by the addition of a 50 Ω resistor between the n-side of the detector diode and the power supply. This modification slowed the rise time of the detector to 10 ns and increased the rise time of the temperature jump signal to 13.5 ns. Later results by Pozo Ramajo[92] showed that the overshoot was still present and it was suppressed even further by replacing the 50 Ω resistor with a 57 Ω resistor. This replacement of the resistor increased the overall rise time of the detector to 15 ns.

Even after modification of the detector, a residual electronic overshoot artifact still remains. Pozo Ramajo[92] investigated whether this artifact was intrinsic to the setup or a direct response from D_2O. This was carried out by placing a germanium window with a thickness of 2 mm at the sample position. The results showed that the germanium window is more or less transparent for the probe light at 1601 cm^{-1}. When the germanium window was illuminated with the pump light, electron rearrangements occurred in the germanium leading to promotion of some electrons from the valence band to the conductance band. Consequently, photons were absorbed at 1601 cm^{-1} by electrons in either the valence band or the conductance band, resulting in a decrease in the IR signal.

Pozo Ramajo[92] recorded measurements with different pump energies. For all, the initial overshoot was present and identical to measurements taken in D_2O. Therefore, the initial overshoot was found to be due to the detector system and not from heating of D_2O. Moreover, the artifact was found to be only 1% of the total absorbance change and to decay on the 10 ns timescale.

The detector is connected to a 300 MHz digital oscilloscope (Tektronix TDS 3032) via its DC output, which has a bandwidth of 50 MHz and a responsivity of 2.48 x 10^4 V/W before modification of the detector[92]. The oscilloscope is triggered by a reflection of the 532/355 nm light from the Nd:YAG laser, detected by a fast silicon diode detector (Thorlabs DET210, rise time 1 ns). Measurements were taken with 64 or 512 single scans that were averaged by the oscilloscope before being transferred through an IEEE connection to a PC, where they were analyzed.

2.2 Temperature Jump Analysis

When doing temperature jump measurements (TJ), radio frequency (RF) electric noise from the Nd:YAG laser is induced in the detector. The amount of RF noise collected by the detector was minimized by wrapping the power supply cable and the other cables with wire mesh and by the addition of capacitors and filters to the power supply.

To further reduce the RF noise, background (BG) subtraction was applied to the TJ measurements. The BG measurements were obtained by recording several single scans (64 or 512 single scans) and averaging them in the oscilloscope when the shutter (ThorLabs, SH05, beam shutter) is closed. As shown in Figure 2.1, the shutter is placed between M4 and M5 and its purpose is to avoid irradiating the sample when no measurements are in progress. On the other hand, TJ measurements were taken when the shutter is open (allowing for the induction of temperature jumps) with the recording of several single scans (64 or 512 single scans) averaged in the oscilloscope. This allows us to observe the change in absorbance of the sample. The BG and TJ measurements were taken in the order of TJ1, BG1, BG2, TJ2 etc, to compensate for potential drift of the RF noise.

With the probe beam blocked and shutter closed, a negative offset signal was observed (~-100 mV). Thus, it was necessary to measure the offset signal and add it to the observed signals so as to obtain the real temperature jump signal. Once the measurements have been transferred to the computer, the signal was converted into absorbance change ($\Delta A(t)$) using the equation below:

$$\Delta A(t) = -\log \frac{I_t}{I_o} \tag{2.1}$$

where t is the time delay after the temperature jump, I_t is the time dependent intensity and I_o is the initial intensity (before the temperature jump). The conversion of signal into absorbance was done automatically with the aid of a computer program. After every measurement had been converted into absorbance, they were averaged to give a single averaged curve for each wavelength investigated. The averaged curves were then logarithmically averaged using a logarithmic averaging program. This was done by averaging all values measured at times within 1% of each other after 30 ns or after 50 ns.

Before fitting the logarithmically averaged curve, an additional correction was applied. In D_2O, a decrease of the absorbance at all wavelengths is observed after a temperature jump, which arises from a shift of the D_2O association band with temperature. This absorbance change appears instantaneously within the nanosecond time resolution of our setup as the sample is heated. The absorbance change then decays mostly on the timescale of 100 μs to 10 ms as the sample cools due to heat diffusion. However, the onset of cooling is apparent on the hundred of nanosecond to microsecond timescale. This onset of cooling distorts the fit results and needed to be corrected for before fitting[89, 92] (see chapter 2.4.1).

The curve was fitted using a non-linear least squares (Levenberg-Marquardt) fitting routine in Microcal Origin. For all temperature jump results shown here (Chapters 3, 4 and 5), the curve was well-described by either a mono-exponential or multi-exponential decay from which the averaged relaxation time constant was obtained. This is because the protein and peptide investigated exhibited a heterogeneous decay that requires the sum of two or more exponentials for an adequate description of the average relaxation time constant. Also, a stretched exponential function was used for fitting, which is shown in equation 2.2 below:

$$y = y_o + A * \exp(-kt)^{\beta} \tag{2.2}$$

where y_o is the offset, A is the amplitude, k is the rate constant, t is time and β is a measure of the net deviation from mono-exponentiality, which varies between 0 and 1. By knowing the values of k and β, the averaged relaxation time constant (τ) can be obtained from equation 2.3:

$$\tau = \frac{\Gamma\left(\frac{1}{\beta}\right)}{k\beta} \tag{2.3}$$

where Γ is the gamma function.

Finally, a method was used to estimate the error in the average time constant. For all measurements taken with 64 single scans or 512 single scans, measurements were grouped into groups of five (5 x 512 single scans) or ten (10 x 64 single scans) and were then analyzed by the methods discussed above. The standard deviation of the individual time constants obtained in this way was calculated and used as an error estimate for the averaged time constant[89].

2.3 Temperature Jump Calibration

Temperature variation is an important factor when studying the folding dynamics of peptides and proteins[24, 32, 33, 60, 63, 85, 86, 90, 93]. Due to its importance, a consistent method is needed to correctly characterize the size of the temperature jump. As shown in Figure 2.5, the IR absorbance of D_2O varies with temperature. This can be used for determining the size of the temperature jump by measuring the absorbance change at a wavelength where the protein/peptide itself has no absorbance. To quantitatively calibrate the absorbance changes of D_2O, two methods were used: the cw-IR laser of the setup described above and a Perkin Elmer FT-IR spectrometer.

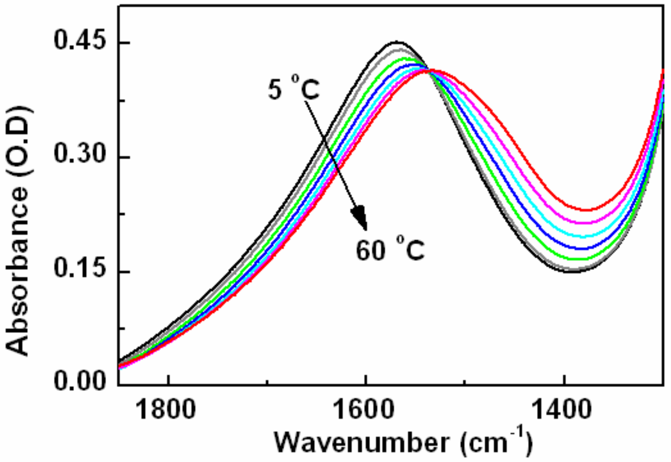

Figure 2. 5: Temperature dependent FT-IR spectra of D_2O from 5 °C to 60 °C (50 µm path length).

Firstly, a Perkin Elmer FT-IR spectrometer was used to determine the D_2O absorbance change with temperature. The temperature controlled IR cell was filled with D_2O (50 µm path length) and placed in the spectrometer. FT-IR spectra were taken at 10 °C to 70 °C (in steps of 10 °C, data not shown), where the temperature was varied using a water bath. The absorbance at different wavelengths was recorded for each temperature and fitted to a second order polynomial with respect to temperature, as shown in Figure 2.6. For example, at 1584 cm^{-1}, the second order polynomial equation is given by:

$$A_{1584} = 6.1836\times10^{-6}\times T^2 - 0.00248\times T + 0.589 \tag{2.4}$$

where T is the temperature (°C). The absorbance change with respect to T can then be obtained from the equation 2.5 and 2.6 below for 1584 cm^{-1} and 1631 cm^{-1}, respectively:

$$\left(\frac{dA}{dT}\right)_{1584} = -0.00248 + 2\times6.1836\times10^{-6}\times T \tag{2.5}$$

$$\left(\frac{dA}{dT}\right)_{1631} = -0.00222 + 2\times4.5747\times10^{-6}\times T \tag{2.6}$$

where T is the temperature (°C).

Secondly, the cw-IR laser, tunable between 1570 cm^{-1} and 1640 cm^{-1} was used for calibration purposes. The cw-IR laser was tuned to a particular wavelength and the initial intensity was recorded. It was ensured that the maximum signal at the detector was ~300 mV to avoid saturation (see above). A D_2O sample was placed in a temperature controlled IR cell (50 µm path length) in the sample position, as shown in Figure 2.1. The mirror M2 and lens L3 were optimized for the maximum signal. Once this was achieved, the temperature was varied from 10 to 70 ^{o}C (in 10 ^{o}C steps). The signal was measured at each temperature and the absorbance was calculated. The absorbance with respect to temperature was fitted with a second order polynomial function as described above. The temperature dependent absorbance change per degree Celsius can be obtained from equations 2.7 and 2.8 below for 1584 cm^{-1} and 1631 cm^{-1}, respectively:

$$\left(\frac{dA}{dT}\right)_{1584} = -0.00267 + 2\times 6.1683\times 10^{-6}\times T \tag{2.7}$$

$$\left(\frac{dA}{dT}\right)_{1631} = -0.00227 + 2\times 4.1601\times 10^{-6}\times T \tag{2.8}$$

where T is the temperature (^{o}C).

There is a slight discrepancy between the FT-IR and CW-IR laser measurements, as shown in Figure 2.6 a. We attribute this discrepancy to background drifts over time. No cyclic measurements were taken; hence the experimental CW and FTIR data were averaged and then fitted to a second order polynomial, as shown in Figure 2.6 b. The temperature dependent absorbance change per degree Celsius can be obtained from the equation 2.9 and 2.10 for 1584 cm^{-1} and 1631 cm^{-1}, respectively:

$$\left(\frac{dA}{dT}\right)_{1584} = -0.00256 + 2\times 6.1582\times 10^{-6}\times T \tag{2.9}$$

$$\left(\frac{dA}{dT}\right)_{1631} = -0.00223 + 2\times 4.3293\times 10^{-6}\times T \tag{2.10}$$

where T is the temperature (^{o}C).

The absorbance changes with respect to temperature for the wavelengths 1584 cm^{-1} and 1631 cm^{-1} are shown in Figure 2.7. For example, the absorbance change at 20 ^{o}C is -0.0023 O.D./^{o}C at 1584 cm^{-1} and -0.0021 O.D./^{o}C at 1631 cm^{-1}.

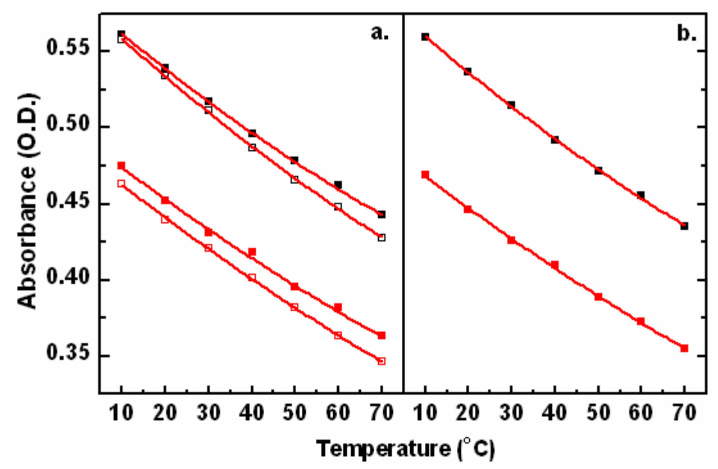

Figure 2. 6: The absorbance with respect to temperature at 1584 cm^{-1} (black) and 1631 cm^{-1} (red) of a D_2O sample (50 µm path length). (a.) Absorbance at 1584 cm^{-1} (black squares: solid, FT-IR; open, CW) and 1631 cm^{-1} (red squares: solid, FT-IR; open, CW). (b.) Average FT-IR and CW absorbance at the two wavelengths using FT-IR and CW. The polynomial fits are shown as red lines for the two wavelengths. The measurements were taken using the CW-IR tunable laser and FT-IR spectrometer as described in the text.

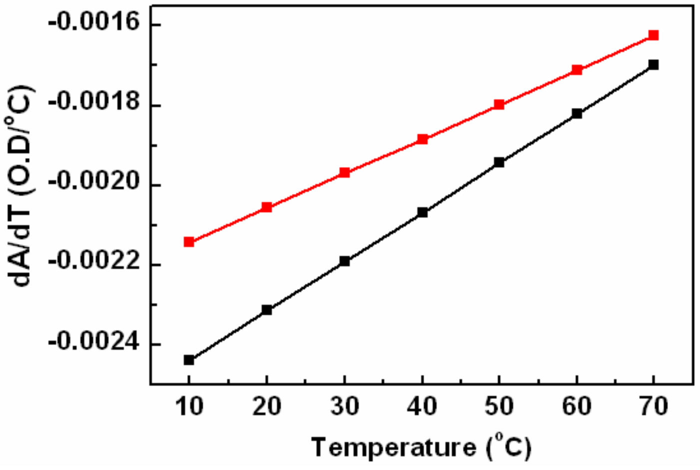

Figure 2. 7: Absorbance change with respect to temperature at 1584 cm^{-1} (black squares) and 1631 cm^{-1} (red squares) of a D_2O sample (50 µm path length).

Williams et al[64] were the first to report an absorbance change per degree Celsius of -4.0 x 10^{-5} O.D./^{o}C•µm at 28 ^{o}C[1] for 1630 cm^{-1}. This was tested a few years later in our research group by Pozo Ramajo[92], where she reported an absorbance change per degree Celsius of -0.0017 O.D./^{o}C at 20 ^{o}C for 1630 cm^{-1} and a path length of 50 µm. This value is considerably different to the most recent calibration done here (absorbance change of -0.0021 O.D./^{o}C). This is because the detector was partially saturated when Pozo Ramajo[92] performed the calibration. On the other hand, our new calibration results are in agreement with Williams et al[64]. Therefore, the calibration obtained here will be used to calibrate the size of the temperature jump throughout this project.

2.4 Measurement Artifacts and Limitations

While using the laser initiated temperature jump technique to follow the folding dynamics of peptides and proteins on the ns-timescale, several artifacts and limitations occur. These include an electronic overshoot (discussed in section 2.1.7), pressure relief, photoacoustic cavitation and cooling due to heat diffusion. It is important to minimize such problems so as to follow the dynamics of these proteins and peptides on the nanosecond time scale. Another artifact that often occurs is thermal lensing. However, this artifact was not an issue in our setup since the detection optics was designed to avoid thermal lensing artifacts.

2.4.1 Cooling

Cooling of the probed sample volume after a temperature jump is known to occur mainly on the millisecond timescale[92]. This effect was previously observed experimentally in our group and by other researchers[60, 64, 92, 93] and, although cooling occurs mostly on the millisecond timescale, the absorbance change of D_2O at 1583 cm^{-1} decreases by approximately 1% after 3 µs (50 µm path length), which was assigned to the onset of cooling[92].

In 2002, Wray et al[94] performed a series of finite element heat transfer calculations for D_2O-CaF_2 systems. Their calculation showed that the temperature of the

---

[1] The absorbance change of -4.0 x 10^{-5} O.D./^{o}C•µm corresponds to a change of -0.0020 OD/^{o}C at 1630 cm^{-1} for a 50 µm path length.

probed sample volume decreases by approximately 10% within 50 µs, for 50 µm sample thickness and 100 µm pump focus diameter or 300 µm pump focus diameter. However, their results are not correct, since a limited number of cells were used for their calculations (where cells refer to the cells of the calculations).

More reliable simulation calculations were performed in our research group to confirm the 1% absorbance recovery on the microsecond timescale to be due to cooling[2].

This onset of cooling in the first few microseconds also distorts the absorbance change at 1631 cm^{-1}, where protein relaxation is observed in this project, and needs to be corrected for before data analysis. The correction is particularly important if the amplitude of the absorbance change from the unfolding protein is small on the nanosecond timescale, in which case the distorting effect is much more prominent[89, 92].

To correct for the onset of cooling, Pozo Ramajo[89, 92] performed measurements on samples that do not contain peptide or protein. Measurements were taken at 1584 cm^{-1} and fitted either mono-exponentially or bi-exponentially with an offset. This was to ensure that the optimum correction was achieved. For measurements up to 2 µs, the correction function is best described by function 2.11[89, 92]:

$$(1-c)+c\times e^{\frac{-t}{\tau cool}} \tag{2.11}$$

where c = 0.05. This is the absorbance change decrease due to cooling with respect to the initial absorbance change and t is time (ns) and τ_{cool} = 10000, the time constant of the initial cooling phase.

In this work, a new function was determined for measurements up to 40 µs. The correction function is described by the function below:

$$(1-(a+b))+a\times e^{\frac{-t}{\tau cool1}}+b\times e^{\frac{-t}{\tau cool2}} \tag{2.12}$$

---

[2] M. Volk at the University of Liverpool, private communication.

where a is 0.011, the absorbance change decrease which is due to the fast cooling component, having a time constant (τ_{cool1}) of 4.5 μs, with respect to the initial absorbance change, b is 0.089, the absorbance decrease due to the slower component, having a time constant of 40 μs (τ_{cool2}), with respect to the initial absorbance change and *t* is the time delay (ns).

Finally, the absorbance changes at 1631 cm^{-1} were corrected for the onset of cooling by dividing by the optimum functions above. While other groups subtracted the absorbance changes observed in neat D_2O in a matched cell[60, 64, 93], our method has the advantage of correcting for the effects of cooling not only on the absorbance of D_2O, but also on the protein and peptide amide I band, which shifts with changing temperature due to the peptide carbonyls' interaction with the solvent[89].

2.4.2 Photoacoustic Cavitation

During temperature jump measurements, a negative artifact was observed in the probe intensity at the detector. This negative artifact is referred to as photoacoustic cavitation. The sudden increase in temperature during the temperature jump creates an increase in pressure which subsequently drops on a time scale determined by the speed of sound (see chapter 2.4.3). Consequently, the solvent molecules move outwards and, as a result of inertial motion, the pressure decreases to values below the surrounding pressure, making the solvent more susceptible to bubble formation which distorts the IR beam[89, 92]. The photoacoustic event is sporadic in nature, temperature dependent and the timescale on which this event occurs is on the order of a few microseconds.

As the temperature jump is increased above 5 to 10 ^{o}C, the probability of observing this event increases significantly. This event is even more pronounced at higher temperatures because the dissolved gases become less soluble in D_2O solution[94] and the thermal expansion coefficient increases with temperature.

Photoacoustic cavitation also occurs when visible laser pulses are used to induce temperature jumps in samples containing heat transducing dyes[19, 89]. This artifact is much more pronounced in this case because the dyes are very difficult to dissolve in aqueous solution and aggregates are often formed, which may act as nucleation sites for the formation of bubbles. Pozo Ramajo et al[89, 92] found that cavitation events can be fully avoided for temperature jumps of up to 10 ^{o}C from room temperature in aqueous solutions of heat transducing dye by stirring the dye solution for several days and stopping the sample flow during the measurement. As well as stirring the solution for days, we found that filtering of the solution with a 0.2 µm pore size filter can significantly reduce the occurrence of cavitation events.

According to Duxbury[95], triphenylmethane dyes are known to form aggregates in aqueous solution which results in a characteristic absorbance band blue-shifted from the monomeric dye absorbance. Therefore, it is suggested that in fresh crystal violet (CV) and basic fuchsin (BF) dye solutions, cavitation is enhanced by particles of aggregated dye molecules which may act as nucleation sites for cavitation, similar to the bubble formation by undissolved impurities after temperature jumps in D_2O[94]. Moreover, not flowing the sample ensures that no residual particles, which may be present in low concentrations even after extended stirring, are flowed through the laser focus. Consequently, the combination of extended stirring, filtering, and stopping sample flow allows for observing the dynamics of peptides and proteins. However, not flowing the sample leads to a rapid decrease in the size of the temperature jump due to photo-bleaching of the heat transducing dye (discussed in detail in chapter 3).

2.4.3 Pressure Relief

Water expansion occurs from the release of pressure induced by increasing the temperature. Upon absorption of laser light, heating occurs. This leads to an expansion in the liquid, but initially thermal pressure is generated which is not relieved during the time energy is deposited in the liquid[94]. The timescale on which this pressure relief occurs can be estimated from the radius of the pump focus diameter (~300 µm) divided by the speed of sound (1398 m/s) to be ~250 ns, which is much larger than the time in which the temperature jump is generated (~5-6 ns). On the time scale of the pressure relief, acoustic waves move away from the high pressured region at the heated spot, resulting in reduced pressure, potentially leading to photoacoustic cavitation[94, 96] (see chapter 2.4.2.).

From the thermal expansion coefficient (α) of D_2O at the final temperature, the change in volume of D_2O induced by a temperature change (ΔT) can be determined with the equation below:

$$\frac{\Delta V}{V} = \alpha \times \Delta T \tag{2.13}$$

For example, the volumetric thermal expansion coefficient of D_2O at 60 ^{o}C is ~0.0006/^{o}C[94]. For a temperature jump from 55 ^{o}C to 57 ^{o}C, the volume is expected to increase by 0.12%. Consequently, the density of D_2O should decrease by 0.12% after pressure relief, resulting in the same decrease of the absorbance. A D_2O sample has an absorbance of ~0.5 (70 µm path length) at 1584 cm^{-1} at 55 ^{o}C. Thus, in addition to the instantaneous absorbance decrease due to the temperature increase, a further absorbance decrease of 0.0006 is expected to occur on the time scale of the pressure relief after the temperature jump.

Figure 2.9 (black curve) shows the time dependent absorbance change at 1584 cm^{-1} in CT_8-NP/D_2O solution after a temperature jump from 55 ^{o}C to 57 ^{o}C. At this wavenumber, only D_2O has significant absorbance and the absorbance decreases as the temperature increases due to the shift of the D_2O absorbance band with temperature (Fig. 2.5). This absorbance change appears instantaneously within the time resolution of our temperature jump setup. In addition to the initial instantaneous absorbance decrease, we observed a further decrease on the hundred nanosecond time scale due to pressure relief (see Figure 2.9, black curve), followed by a slight absorbance recovery, corresponding to the recovery of the pressure after reaching values below the surrounding pressure (see chapter 2.4.1). The absorbance then remains constant up to the millisecond time scale, when the sample cools due to heat diffusion.

The observed absorbance decrease on the pressure relief time scale (0.00025) is of the expected order of magnitude, although somewhat smaller than the predicted value. A smaller value was also seen by Pozo Ramajo[92]. She suggested that this could be explained if the reduced density would lead to an increased extinction coefficient of the intermolecular vibrations of D_2O (responsible for the “association band” of D_2O around 1600 cm^{-1}) which are sensitive to intermolecular interactions, and thus the average distance between the solvent molecules.

The temperature dependence of this pressure relief effect was previously studied in detail by Pozo Ramajo[92]. She observed that the absorbance changes of the pressure relief artifact were virtually non-existent at a final temperature of 6 °C. This is because the final temperature is close to the temperature of the maximum density of D_2O, where the expansion coefficient is close to zero. However, she observed that the amplitude of this artifact increased with increasing temperature and needed to be corrected when the final temperature is higher than the temperature of the maximum density of D_2O, since the thermal expansion coefficient increases with temperature (see Figure 2.10). Consequently, the data shown in Figure 2.10 further confirm the presence of this pressure relief artifact, as the effect increased with increasing temperature.

An attempt was made here to suppress this pressure relief artifact. In an attempt to eliminate this pressure relief, the sample was restricted to a small sample volume of ~500 µm diameter created between two CaF_2 windows. This small size was to ensure that the sample was heated homogeneously without the possibility of pressure relaxation. The holes were created by punching small holes of ~500 µm diameter into a 70 µm Teflon sheet, as shown in Figure 2.8. The Teflon sheet was placed between the CaF_2 windows with 100 µl of neat nanoparticle solution (care was taken not to create bubbles in the sample once placed between the CaF_2 windows). Peptide-capped gold nanoparticles are used here as heat transducers. They are very stable in aqueous solution and cavitation events are significantly reduced in comparison to heat transducing dyes (BF or CV) (see Chapter 3 for further discussion).

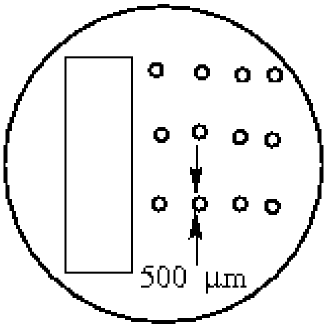

Figure 2. 8: Teflon sheet for pressure relief suppression with 500 µm diameter holes and a larger area. The larger area is to verify the presence of the pressure relief artifact under the experimental conditions employed.

With the cell in the sample position, as shown in Figure 2.1, measurements were first taken in a larger area (see Figure 2.8) to verify that the pressure relief is indeed observable under the conditions of the experiment before we attempted to do measurements in the small holes created in the Teflon sheet.

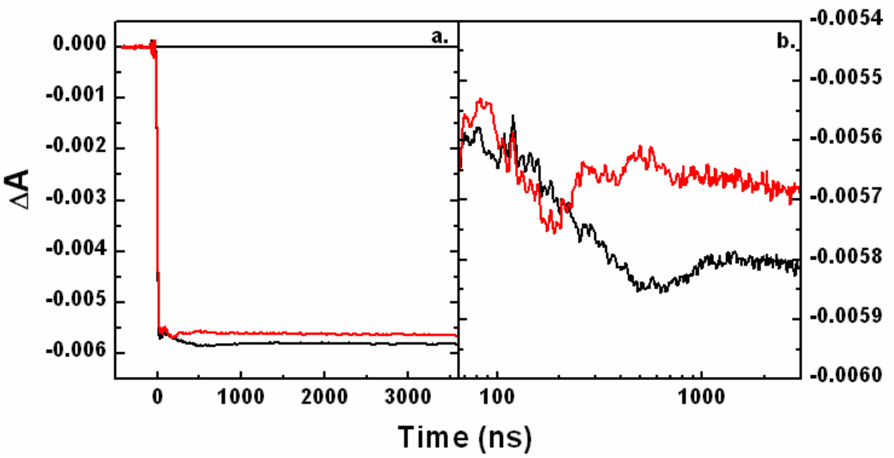

Figure 2. 9: Time dependent absorbance changes at 1584 cm^{-1} for D_2O in 4 x 10^{-6} M CT_8-NP/D_2O solution after a temperature jump of 2 ^{o}C from 55 ^{o}C (70 µm path length). (a.) The overall absorbance change in the large area shown in black and the absorbance change in a 500 µm diameter hole shown in red. (b.) Zoomed in on the few hundred ns timescale.

Having verified the pressure relief effect in the larger area, the sample cell was moved in the X and Y position until the continuous IR beam was transmitted through a small hole. After the optimization was completed, the temperature jump induced in the small area was similar to the temperature jump observed in the larger area, as shown in Figure 2.9. The final temperature jump induced in both the larger area and the 500 µm diameter hole was 2^{o}C.

In using this technique, we observed that the further absorbance decrease on the 100 ns time scale was indeed much smaller (red curve in comparison to black curve), as expected if pressure relief is suppressed. However, additional artifacts occurred, as shown in the red curve of Figure 2.9 b. We attribute such artifacts to the heating of the Teflon sheet and to residual pressure relief acoustic waves and their reflection on the wall of the holes. Most importantly, unlike the pressure relief artifact in larger areas, these new artifacts are not well reproducible and thus cannot be easily corrected for.

Since it does not seem possible to suppress the pressure relief artifact without introducing other artifacts, we developed a method to subtract the pressure relief artifact. Firstly, time dependent absorbance changes of D_2O at 1584 cm^{-1} were measured at 30 to 60 ^oC (in 10 ^oC steps) in the presence of heat transducer (CT_8-NP), as shown in Figure 2.10. Each curve was logarithmically averaged and corrected for cooling. It is important to note that the absorbance change should be constant after cooling correction since the sample is neat D_2O and heat transducing gold nanoparticles, which show no absorbance change at this probe wavelength, see chapter 3). As expected (and described in detail above) and shown in Figure 2.10, the pressure relief artifact on the few hundred ns-time scale increased with increasing temperature.

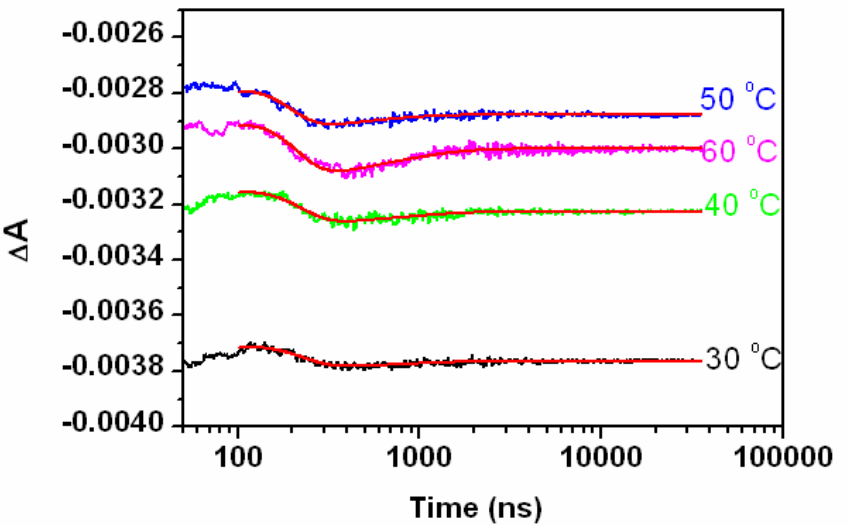

Figure 2. 10: Time dependent absorbance changes of a neat nanoparticle solution in D_2O (50 µm path length) at 1584 cm^{-1}. The temperature varies from 30 ^oC to 60 ^oC in 10 ^oC steps. The temperature jump varies from ~1.5 ^oC to ~2.0 ^oC. The red lines are the fits at each temperature. All data shown here were logarithmically averaged and corrected for cooling.

The curves were fitted in the time range of 100 ns to 35 µs with a phenomenological Gaussian/exponential function plus an offset, as shown in equation 2.14 below:

$$y(t) = y_o + A \times e^{\frac{-(t-t_c)^2}{2w^2}} + A1 \times e^{\frac{-t}{\tau}} \quad (2.14)$$

where y_o is the offset, A and $A1$ are the amplitudes, t is the time delay, t_c is the center time of the Gaussian (ns), τ is the time constant, and w is the width of the Gaussian. As shown in red, the fits obtained were very good.

The parameter t_c was fixed to 100 ns, since we observed a significant amount of variation when t_c was allowed to be varied. The amplitudes obtained from the fits were normalized with respect to the exact temperature (ΔT) of each measurement and the absorbance of D_2O at 1584 cm^{-1} at each temperature. Finally, the normalized amplitudes, widths, and times were fitted linearly with respect to temperature, as shown in Figure 2.11 a-c to give the equations (2.15 to 2.18) below:

$$w = 122.22402 + (-0.6235 \times T) \tag{2.15}$$

$$\tau = 916.23865 + (-6.48776 \times T) \tag{2.16}$$

$$A = -9.69676x10^{-6} + (6.39504x10^{-6} \times T) \tag{2.17}$$

$$A1 = 1.25386x10^{-4} + (-5.31211x10^{-6} \times T) \tag{2.18}$$

where T is the temperature (^{o}C). From the linear equations, we were able to obtain the temperature dependent parameters for equation 2.14 at all temperatures.

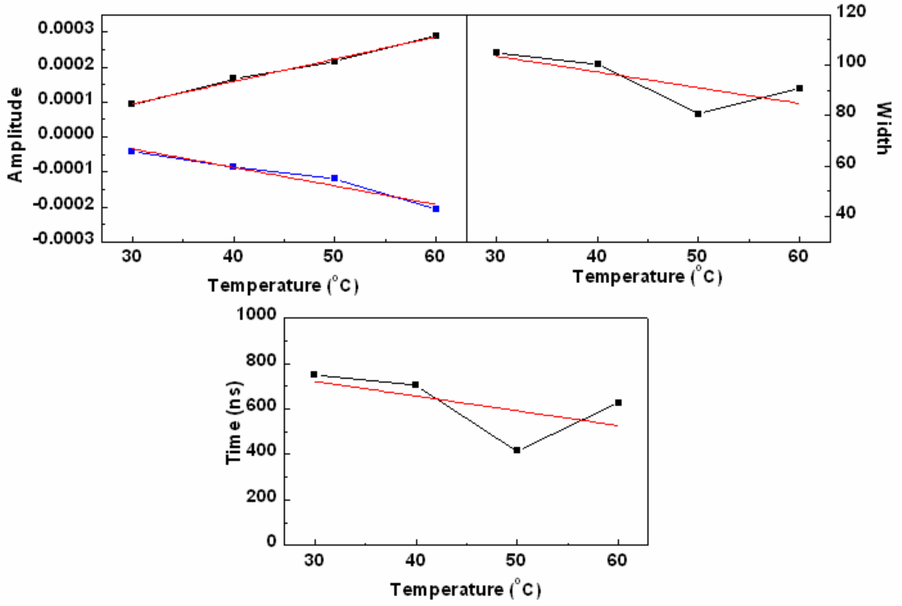

Figure 2. 11: The linear fits of the pressure relief parameters with respect to temperature. (a.) The linear fit of the normalized amplitudes (A; black and A1; blue). (b.) Linear fit of the widths. (c.) Linear fit of times. The red lines are the best linear fits.

Finally, we corrected for the pressure relief in our peptide/protein measurements by subtracting the optimum correction function determined above from the neat nanoparticle time dependent traces at 1584 cm^{-1}. The correction function, Equation 2.14, without the offset, was multiplied by the total absorbance of the sample at the wavelength at which the measurement was taken and the size of the temperature jump to obtain the optimum correction function. As a note, this correction is valid for all measurements taken at elevated temperatures (see Chapter 4) and the correction of the pressure relief was only applied to data after 100 ns.

An example of where the pressure relief correction has been applied is shown in Figure 2.12. Figure 2.12 shows the time dependent absorbance changes of a ~10 mg/ml poly(n-isopropylacrylamide) (pNIPAM) sample after a temperature jump of 4 ^{o}C in CALNN-NP/D_2O solution, where the black curve and the red curve are the uncorrected and corrected data, respectively.

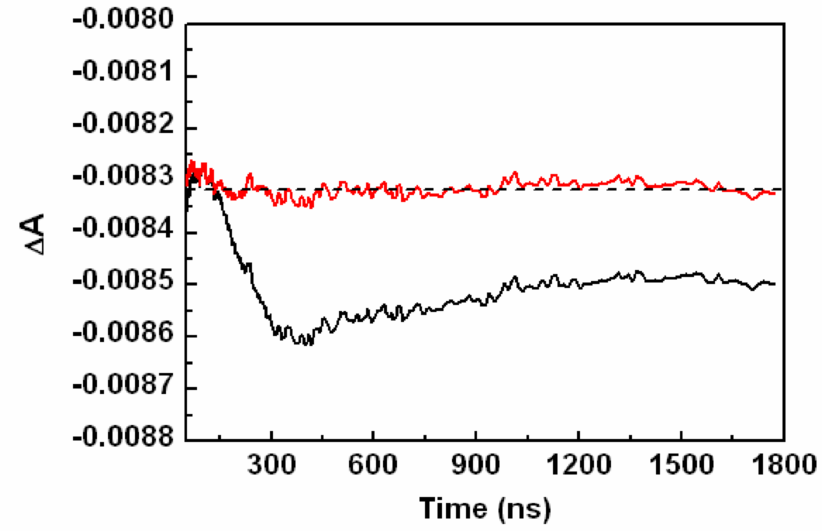

Figure 2. 12: Pressure relief correction for the time-dependent absorbance change at 1584 cm^{-1} after a temperature jump of 4 ^{o}C from 34 ^{o}C in ~10 mg/ml pNIPAM (50 µm path length, ~4 x 10^{-6} M CALNN-NP/D_2O). The red curve is the corrected data and the black curve is the uncorrected data. The data were logarithmically averaged and corrected for cooling[3]. The dotted line is to guide the eye.

---

[3] Measurements were taken by Christopher Bentley, a PhD student in our research group.

The major absorbance decrease is due to the absorbance of D_2O which decreases with increasing temperature. In addition to this instantaneous absorbance decrease, a further decrease was observed during the first few hundred nanoseconds due to pressure relief followed by a slight recovery due to pressure recovery (black curve, see discussion above). The absorbance then remains constant up to the milliseconds time scale as the sample cools due to heat diffusion. As a note, pNIPAM has no absorbance at this wavenumber. Therefore, after the instantaneous absorbance change, no additional absorbance change is expected to occur on nanosecond time scale. As can be seen, the pressure relief correction, based on Eq. (2.14), is very good and yields exactly the expected result (red curve).

2.5 Principles of FT-IR Spectroscopy and Measurements

Today, most modern infrared spectrometers are Fourier transform infrared spectrometers (FT-IR). An FT-IR spectrometer consists of a source, interferometer, and a detector, but the heart of the spectrometer is an interferometer, as shown in figure 2.13. The Michelson interferometer is a device that splits a beam of radiation into two beams of nearly equal power and then recombines them in such a way that the intensity variation of the combined beams can be measured as a function of the path length difference of the two beams.

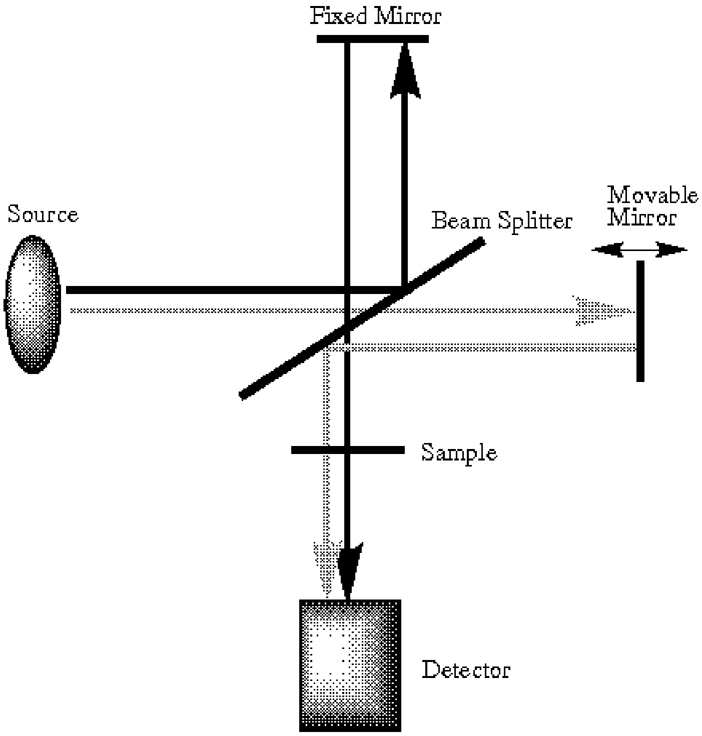

Figure 2. 13: Schematic of an FT-IR Spectrometer

As shown in Figure 2.13, a beam of radiation from the light source is split by a beam splitter where 50 % of the light is reflected and 50 % of the light is transmitted. The resulting beams are reflected by a movable mirror and a fixed mirror, respectively. The two beams then meet again at the beam splitter, with half of each beam directed toward the sample and into the detector and the other half going back toward the source.

Horizontal motion of the movable mirror causes the power of the radiation that reaches the detector to fluctuate in a predictable manner. When the two mirrors are equidistant from the beam splitter, the two parts of the recombined beam are precisely in phase and constructive interference occurs. On other hand, when the movable mirror moves in either direction by a distance equal to exactly one fourth wavelength, the path length of the corresponding reflected beam changes and destructive interference occurs for this particular wavelength. The light intensity with respect to the position of the movable mirror is called an interferogram. The interferogram is Fourier transformed to give a plot of intensity versus wavelength.

The advantage of this method is that it provides rapid measurement, high throughput, and much greater signal to noise ratio than a conventional spectrometer.

Here we used FT-IR spectroscopy to study the structural changes of proteins and peptides. The spectrometer used throughout the course of my studies is a Bio-RAD FTS-40 FT-IR spectrometer linked to a computer for spectral output. Win-IR software was used for collecting the IR spectra. The detector was cooled with liquid nitrogen before starting measurements. The spectrometer was flushed with dry air at all times so as to minimize water vapor accumulation and kept cooled with running water. The spectra were taken with 1 cm^{-1} resolution and averaged over 500 single scans. Even though the instrument was flushed with dry air constantly before taking a spectrum, we observed that residual water vapor lines occurred in the sample spectrum. To correct for this, a percentage of the water vapor spectrum was subtracted from each spectrum until this artifact was minimized in the final absorbance spectrum. Since the solvent D_2O absorbs in the amide 1 region of our peptide and protein samples, a scaled D_2O spectrum at the appropriate temperature was also subtracted from each spectrum before data analysis.

2.6 Sample Cells

During the course of my experimental investigation, the samples were placed between two calcium fluoride (CaF_2) windows separated by a 50 µm, 56 µm or 70 µm Teflon spacer, and mounted in home built temperature controlled cells (copper or stainless steel) or a Harrick cell (Part No. DLC-M25) without temperature control mechanism. When the sample is placed in a temperature controlled cell, water was circulated through a water jacket surrounding the cell, the temperature of which was changed using a water bath (Grant, Low temperature bath/circulator R series). Depending on the sample of interest, the sample was flowed continuously using a peristaltic pump or remained static throughout the course of the measurement.

As mentioned before, the amide I band is very sensitive to temperature. Therefore, it is essential to define the accurate temperature when using the temperature controller for taking FT-IR or temperature jump measurements.

A Pt100 resistor was mounted in a disc (Perspex window) and was calibrated between 1 ^{o}C and 90 ^{o}C by immersion of the disc in water. Temperature ($T/^{o}C$) and resistance (R/Ω) were found to follow a linear relationship described by equation 2.19:

$$R = 0.367 \times T + 100.01 \tag{2.19}$$

To calibrate the copper and stainless steel cells, the Perspex window was used in place of one of the CaF_2 windows in the temperature controlled IR cell. Using the water bath to heat and cool the cell, a multi-meter was used to measure the resistance of the Pt100 resistor for different temperatures of the water bath. From the resistance, the actual temperature in the sample can be calculated, thus allowing calibration of the sample temperature against the water bath temperature.

CHAPTER 3: TEMPERATURE JUMP METHODS

3.1 Background

Understanding of protein folding and unfolding has increased tremendously over the years because of the vast amount of experimental and theoretical methods that make it possible to go beyond the millisecond time resolution of standard stopped-flow or rapid mixing techniques. Central to experimental investigations of the fastest steps of protein folding is the development of fast triggering methods; in particular, the most widely used method of laser-induced temperature jumps.

There are three methods that have been used to induce fast temperature jumps in aqueous solution: indirect laser heating, which requires the use of a heat-transducing dye to allow the induction of temperature jumps by UV/Vis laser pulses, direct laser heating, which requires the use of an IR laser, necessitating more complex laser systems[89, 92, 97] and the Eigen temperature jump method of resistive heating with an electrical discharge[83, 98, 99]. The resistive heating technique is not ideal since it requires high ionic strength solutions and it only enables microsecond time resolution. Direct heating of water by IR laser pulses is the ideal method to induce temperature jumps because it greatly improves quality, reliability, and speed of measurements[89, 92]. However, this method was not available here and hence the indirect laser heating method was used for investigations throughout this research.

Here, we describe the use of triphenylmethane dyes and peptide- and poly-ethylene glycol-capped gold nanoparticles as heat transducers. Gold nanoparticles were tested for the first time as heat transducers in this thesis. We also report results of TR-IR spectroscopic measurements on a small alanine based peptide and conclude that the helix-coil dynamics of the alanine based peptide are not affected by the presence of gold nanoparticles.

3.2 Experimental

3.2.1 Preparation of Dye Solution

The basic Fuchsin dye was purchased from Sigma Aldrich and used as supplied. A stock dye solution was prepared by dissolving ~8 mg of dye in 5 mL D_2O to obtain ~5 mM solution. The dye solution was stirred on a hot plate for several days until dye particles were dissolved. After extended stirring, some of the solution was removed and diluted in D_2O for a dye concentration of ~0.5 mM. The solution was filtered with a 0.2 µm pore filter to remove undissolved particles. The concentration of the dye was verified using UV-Vis spectroscopy.

3.2.2 Preparation of Gold Nanoparticle Solution

The peptide-capped gold nanoparticles (CALNN-NP and CT_8-NP) were prepared by Christopher Shaw[4]. They were prepared by mixing 5 nm citrate-capped gold nanoparticles and peptide stock solution. The samples were freeze dried and stored in an eppendorf tube. The polyethylene glycol-capped gold nanoparticles (PEG-NP) were prepared by Laurence Duchesne[5] and tested by Christopher Shaw. The nanoparticles were characterized by TEM and UV-Vis spectroscopy and used as received. The gold nanoparticles were suspended in D_2O and the concentration was verified using UV-Vis spectroscopy.

3.2.3 Preparation of Peptide Sample

The peptide studied here is Ac-AAAAA-$(AAARA)_4$-NH_2, abbreviated as AR_4, where A is alanine and R is arginine. The peptide was purchased from Pepsyn Ltd and used as received. A fresh sample of AR_4 (~10 mg/ml) was prepared by dissolving in D_2O containing ~4 µM PEG-NP. The pD values were measured with a Whatman PHA230 pH meter equipped with a Hanna Instruments microelectrode (HI 1083) to give pH*, where

---

[4] Collaborator at the University of Liverpool, School of Biosciences

[5] Dave Fernig's group at the University of Liverpool, private communication

pH* is the value measured by the pH meter. To obtain the correct pD value, the equation below was used[100]:

$$pD = pH^* + 0.4 \tag{3.1}$$

The concentration of the sample was verified by FT-IR spectroscopy.

3.2.4 Temperature Jump Measurements

For the neat nanoparticle solutions and AR_4 samples, ~100 µl of the sample was transferred to a temperature controlled home built IR cell with 50 µm path length. For the dye solution, a home-built reservoir was used to flow the dye solution, see below. The total volume needed for this system was ~1 ml. Temperature jumps of up to 5 ^{o}C were induced in the sample using a nanosecond Nd:YAG laser (532 nm, 1 mJ, 5 ns), see chapter 2.1. The absorbance changes were monitored at 1584 cm^{-1} and 1631 cm^{-1}.

The peptide absorbance changes after cooling correction were fitted mono-exponentially between 40 ns and 1500 ns to determine the relaxation time constant. A detailed description of the correction for cooling is given in section 2.4.1. A description of the temperature jump analysis is given in section 2.3.

3.3 Triphenylmethane Dyes as Heat Transducers

When using visible laser pulses for inducing temperature jumps, heat transducers are needed to absorb the laser pulse energy[101]. Typically, triphenylmethane dyes, such as basic fuchsin (BF) and crystal violet (CV) are used for such purposes because they are known to undergo rapid internal conversion on the sub-ps timescale[95, 97, 102, 103]. Both dyes have a high extinction coefficient at 532 nm and have been used in our research group to obtain successful temperature jumps.

The molecular structure of CV is shown in Figure 3.1. It is the first dye to be tested as heat transducer and was successfully used to achieve temperature jumps in protein and peptide samples[19, 101, 104]. However, this dye is not the best heat transducer since it bleaches rapidly upon exposure to laser light, thus preventing the accumulation of several single scans without moving or flowing the sample. To circumvent this problem, the sample was flowed using a peristaltic pump to continuously exchange the dye molecules so as to minimize the bleaching effect. However, flowing the sample is disadvantageous since it requires a large amount of protein/peptide sample, which is not always available, and most importantly, flowing the sample leads to a massive increase in cavitation events. This is because flowing the sample increases the probability of finding dye aggregates in the heated volume which act as nucleation sites for these cavitation events (see chapter 2.4.2).

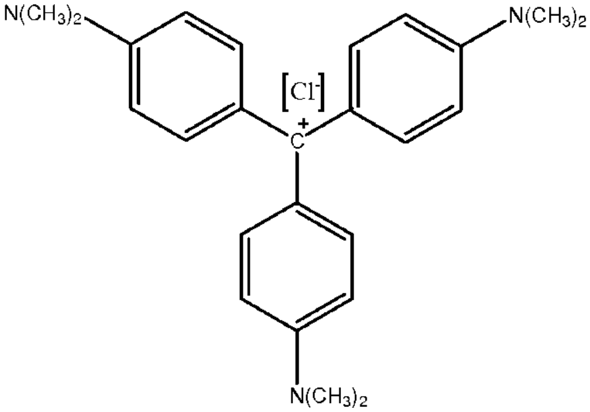

Figure 3. 1: Molecular structure of crystal violet

Other dyes were later tested[92] and BF was found to be a suitable dye for temperature jump measurements. As shown in Figure 3.2 below, the chemical structure of BF is very similar to the chemical structure of CV with the exception of the groups attached to the phenyl rings. The internal conversion is even faster than that of CV because of the smaller attached groups[102].

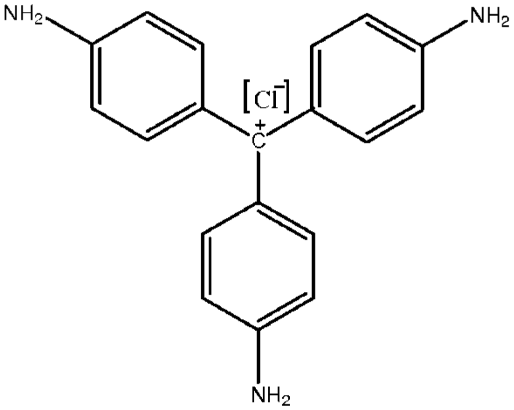

Figure 3. 2: Molecular structure of basic Fuchsin

Pozo Ramajo[92] found that the BF dye bleaches considerably slower than CV and that it seemed possible to accumulate 512 single measurements when the sample was not being flowed. However, when looking more carefully, we found that it was not possible to accumulate 512 single measurements since the dye begins to bleach after 15 seconds of irradiation (~150 single measurements). Furthermore, even when flowing the sample every 15 seconds, the temperature jump decreased by 5% over 5 minutes, accompanied by accelerated dye bleaching and increased cavitation. Thus, our aim here was to develop a technique to minimize these artifacts.

The need to flow the sample regularly requires the use of a small reservoir. Initially, the dye solution was stored in a plastic syringe and the absorbance was monitored over a twenty-four hour period (data not shown). We found that the dye solution degrades rapidly within three hours after preparation. This is because the dye adsorbs to the plastic materials, thus decreasing the concentration of the solution. We then investigated several materials and found that a glass reservoir connected to the cell through Teflon tubing and a metal connector (see Figure 3.3) is ideal for minimizing dye adsorption. Care was taken not to allow the sample to remain in the syringe at any time to avoid dye adsorption on the plastic material.

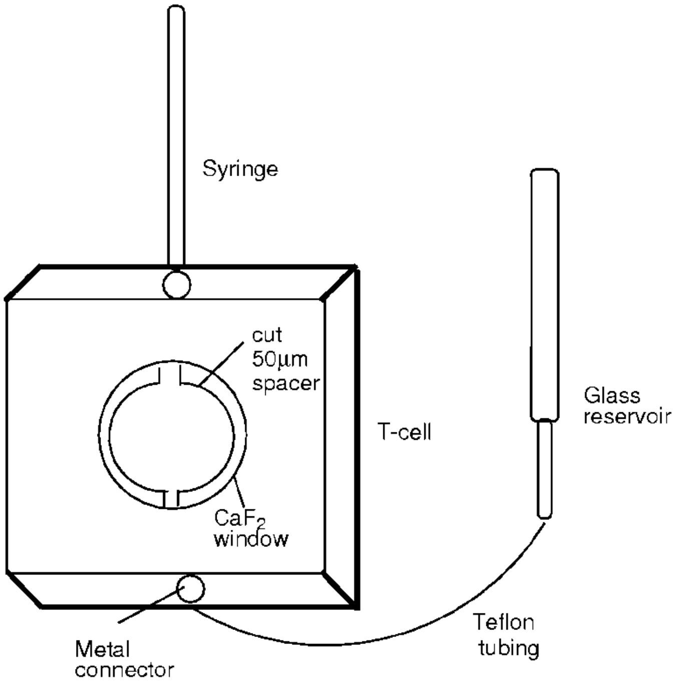

Figure 3. 3: Schematic of the temperature controlled cell with CaF_2 windows (50 µm spacing) equipped with glass reservoir, syringe and Teflon tubing.

The temperature-controlled cell was fitted with two CaF_2 windows and a cut 50 µm spacer. The syringe was filled with ~0.8 mL BF dye solution and attached to the temperature controlled IR cell. The sample was then pumped through the cell with the syringe ensuring that no bubble formation occurs. Since the dye adsorbed to the plastic syringe, it was ensured that the solution did not remain in the syringe for any length of time by pumping the solution into the glass reservoir (see schematic above). Finally, the sample cell was placed on a mount that was fitted with micrometer screws (used for moving the cell) and placed at the sample position (see Figure 2.1).

For temperature jump measurements, the sample was exchanged every 12-15 seconds using the syringe as a pump and the cell was moved after 150 seconds to use a fresh sample spot. This was to ensure that dye aggregates would not amass on the cell window which leads to an increase in cavitation events. This was proven to be an effective method and was useful for taking decent temperature jump measurements, as it allowed us to maintain a constant temperature jump over the full acquisition process. Therefore, this newly hand-operated design allowed us to reduce the sample volume, to reduce dye photo-bleaching and dye adsorption, and to maintain a constant temperature jump.

We also found that while trying to obtain the highest temperature jump possible, the dye degrades rapidly when the energy of the laser is above 2 mJ. To maintain a constant temperature jump throughout, the laser energy was kept as low as possible (~1 mJ), yielding a temperature jump of 3 ^oC.

For the protein investigated in chapter 4 (WT-BBL), a high salt concentration (200 mM NaCl) is needed as this has been proven to stabilize the native state of the protein. It is essential that temperature jump measurements are taken in conditions suitable for the protein's stability and comparable to previous studies of this protein.

Since heat transducing dye is needed for the induction of temperature jumps in a protein/peptide sample, it is necessary to know how the dye is influenced by the addition of NaCl. Here we tested whether BF dye was stable in the presence of high salt concentration.

Figure 3.4 shows the absorption spectra of BF/D_2O solution at various salt concentrations. As shown in the Figure 3.4, the spectral absorption curves of BF are similar in shape in the presence and absence of NaCl. It is important to mention that the dye solution was prepared at a higher concentration (~5 x 10^{-3} M), greater than the concentration typically used for measurements (~5 x 10^{-4} M). However, the dye precipitated upon increasing NaCl concentration. For example, the saturation dye concentration at 50 mM NaCl is ~6 x 10^{-4} M and the saturation dye concentration at 200 mM NaCl is ~2 x 10^{-4} M, as determined from the spectra in Fig. 3.4.

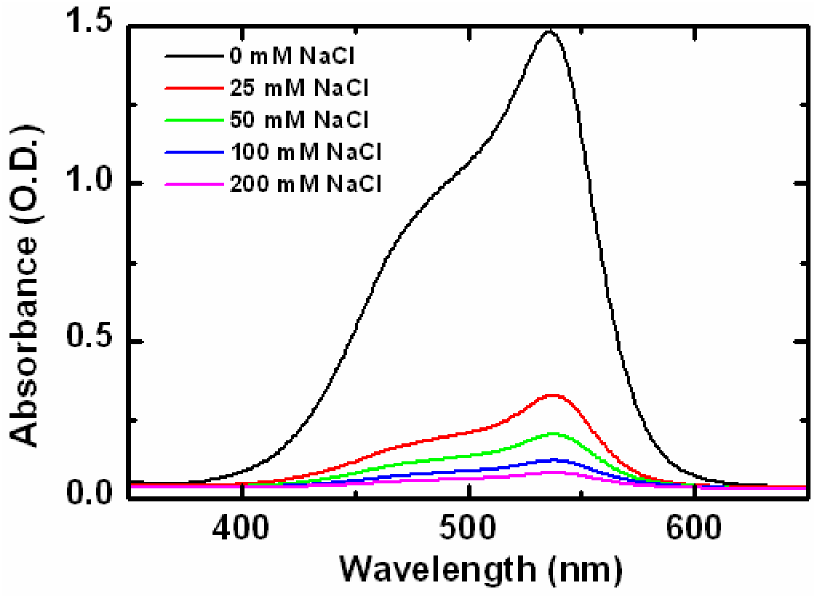

Figure 3. 4: Absorbance spectra of a solution of Basic Fuchsin in D_2O (~5 mM) with various concentrations of NaCl, ranging from 0 to 200 mM, 50 µm spacing.

For the solution containing 50 mM NaCl, we were able to induce temperature jumps of ~4 °C. This temperature jump was possible since the dye solution gave an absorbance of ~0.2 O.D. (typical absorbance for inducing temperature jumps). However, above 50 mM NaCl concentration, the saturation concentration of the dye is too small to get sufficient temperature jumps.

Even though we were able to perform decent temperature jumps in a 50 mM NaCl concentration solution, this is not ideal for the protein investigated (see chapter 4), because changing the ionic strength would require changing the protein's preparation protocol and it would not allow for comparability to previous results. For this reason, BF dye cannot be used for inducing temperature jump in the protein BBL samples.

Therefore, other heat transducers are needed for the investigation of the protein WT-BBL.

3.4 Gold Nanoparticles as Heat Transducers

Triphenylmethane dyes are useful when conducting indirect heating measurements because of the rapid internal conversions on the sub-ps timescale[19, 89, 92, 101]. However, several complications arose with these dyes, which are unavoidable (see section 3.3). Therefore, we tested peptide- and poly-ethylene glycol-capped gold nanoparticles as heat transducers.

Gold nanoparticles are of interest because of their intense color. After absorption of light, the free electrons of the gold nanoparticles undergo a collective coherent oscillation known as surface plasmon resonance[105-109]. The plasmon resonance band for gold nanoparticles is at ~520 nm for a 5 nm diameter gold nanoparticle, as shown in Figure 3.5 below.

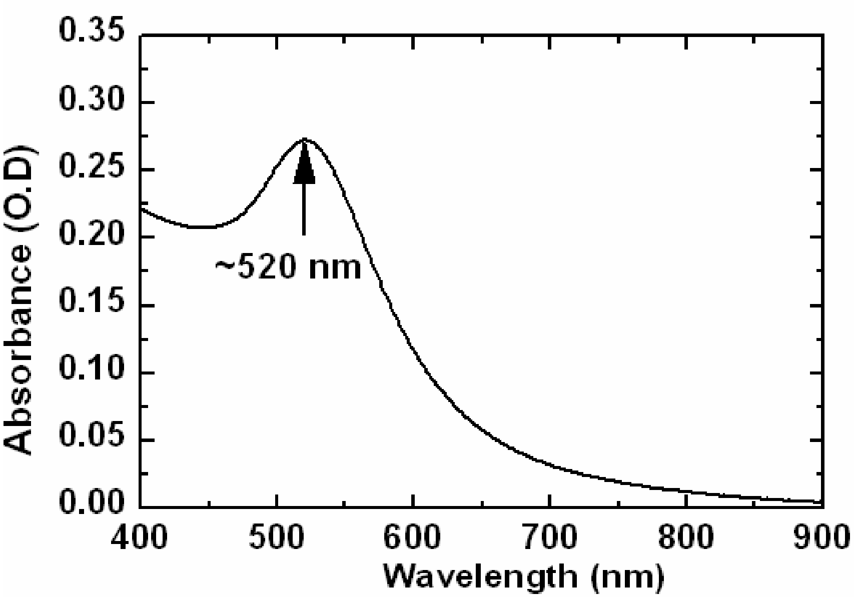

Figure 3. 5: UV/vis absorption spectrum of 5 nm CALNN-NP in D_2O (50 µm spacing, ~6 x 10^{-6} M). The maximum of the plasmon band is at 520 nm.

Upon irradiation of the gold nanoparticles with intense laser light at 532 nm, light energy gets absorbed by the electrons and then transferred to the surrounding solvent (sub-ns). Because of the rapid transfer of the energy to the surrounding solvent, any light energy absorbed is resulting in solvent heating faster than our instrumental resolution[106].

It can be shown that the size and the concentration of the gold nanoparticles can be chosen so that:

1. The absorbance in the plasmon band is correct (0.2 O.D.) for 50 µm path length for inducing temperature jumps in protein and peptide samples.
2. The distance between the nanoparticles is small enough to ensure equilibration of the heat to occur in less than 10 ns. The average distance between randomly dispersed particles (r) at number density, n, can be determined by the equation below[101]:

$$r = 0.554 / n^{1/3} \tag{3.2}$$

Heat diffuses over a distance similar to the distance amongst neighboring nanoparticles within a diffusion time (τ) of 7.4 ns as calculated for our system with a nanoparticle concentration of ~4 x 10^{-6} M (typical concentration used for measurements), from the equation below[101]:

$$\tau = \frac{r^2}{2\chi} \tag{3.3}$$

where χ is the thermal diffusion coefficient of water (1.11 x 10^{-3} $\mathrm{cm^2 sec^{-1}}$).

Gold nanoparticles are known to be very stable in aqueous solution. The new generation of nanoparticles which have covalently linked peptides as capping groups further increases the stability of gold nanoparticles in aqueous solution. According to Levy et al.[110, 111], the basic design principle was to create a ligand that would attach to the surface of the gold particle and form a well-packed passivating layer with a hydrophilic terminus. In such cases, the stability and solubility in water is enhanced. These nanoparticles can be freeze dried and stored as powder for further usage.

In recent years, gold nanoparticles have been used extensively in the area of structural, electronic, imaging, optical, biomedical, and chemical applications[112-117]. Also, gold nanoparticles have been used for heating such as: integrating cancer imaging and therapy applications, reversible photo-thermal melting of DNA, and photo-thermal therapy of epithelial carcinoma[105, 107, 118-123]. However, gold nanoparticles have never been used for rapid large-scale heating on the ns-timescale. Our aim was to test whether gold nanoparticles work as good heat transducers on this time scale, to determine the limitations of the method, and to compare different capping groups. For this reason, we investigated two different peptide-capped gold nanoparticles and poly-ethylene glycol-capped gold nanoparticles.

3.4.1 CALNN Capping Ligand

The first peptide capping ligand tested was CALNN. It is a pentapeptide that was designed to have strong affinity for gold, the ability to self-assemble into a dense layer that excludes water, and a hydrophilic terminus which would ensure solubility and stability[110]. The pentapeptide structure is shown in Scheme 3.1, consisting of five amino acids: Cysteine (C), Alanine (A), Leucine (L), and Asparagine (N). The most important part of the structure is the side chain Cysteine (at the N-terminus), since it can be covalently bonded to the gold surface. Furthermore, amino groups are known to interact strongly with gold surfaces. This peptide-capped nanoparticle is negatively charged.

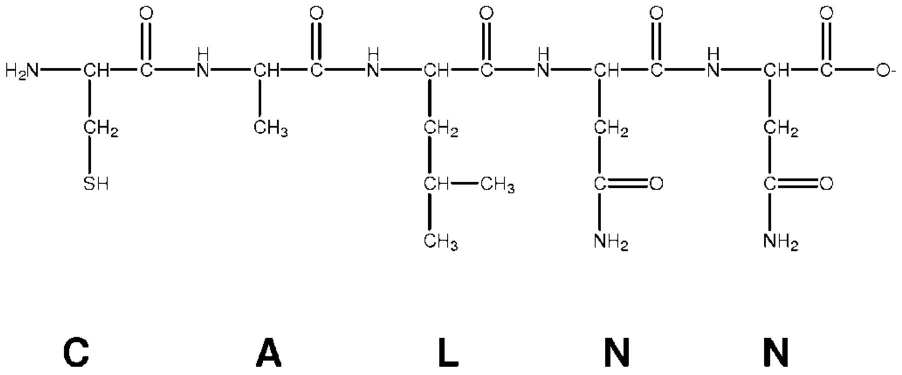

Scheme 3. 1: Schematic representation of CALNN structure where C is Cysteine, A is alanine, L is Leucine, and N is asparagine.

3.4.2 CT_8 Capping Ligand

Another peptide-capping ligand investigated was CT_8 where C is Cysteine and T is Threonine as shown in Scheme 3.2. This peptide-capped gold nanoparticle is negatively charged and has a longer peptide that enhances its stability.

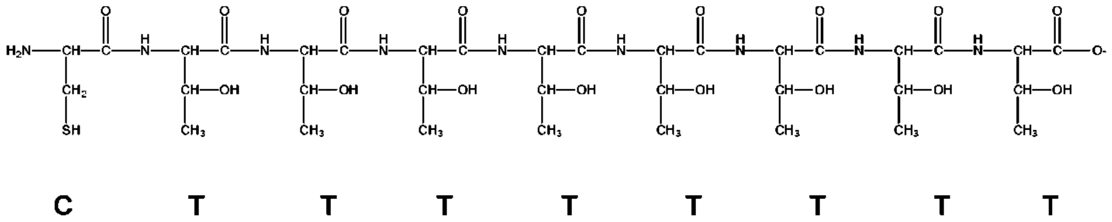

Scheme 3. 2: Schematic of CT_8 structure where C is Cysteine and T is Threonine.

3.4.3 Poly-ethylene Glycol-Capped Gold Nanoparticles

More recently, polyethylene glycol (PEG)-capped gold nanoparticles were developed by Laurence Duchesne[6]. The chemical structure of this capping group is shown in Scheme 3.2.

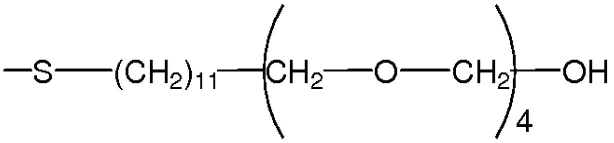

$-S-(CH_2)_{11}-(CH_2-O-CH_2)_4-OH$

Scheme 3. 3: Schematic of PEG-ol structure

This nanoparticle has excellent properties in terms of preventing non-specific binding to proteins and it has very good colloidal stability.

Gold nanoparticle solutions were studied by FT-IR spectroscopy. The IR spectra were taken in D_2O using the FT-IR spectrometer described in chapter 2.5. A relatively broad amide I band was observable in the IR spectra of peptide-capped nanoparticles at ~1650 cm^{-1}, with an absorbance of 5 x 10^{-3} O.D (4 x 10^{-6} M CALNN-NP, 50 µm pathlength), which is much smaller than the typical amide I absorbance of protein/peptide samples used here (~0.2 OD, see e.g. Figure. 3.8). The temperature jump results showed that the time traces of the IR changes of NP solutions in D_2O are identical to those observed when using our standard dye. Therefore, there is no additional signal from the peptide-capped gold nanoparticles.

---

[6] Dave Fernig's group at the University of Liverpool, private communication

3.5 Testing of Gold Nanoparticles for Inducing Temperature Jumps

As discussed in chapter 3.3, we have shown that triphenylmethane dyes can be used successfully as heat transducers. However, several artifacts arose with these dyes which cannot be ignored. Therefore, gold nanoparticles were tested here for the first time as heat transducers.

Unlike triphenylmethane dyes, nanoparticles do not photo-bleach, thus there is no need to flow the sample. Also, cavitation events are significantly reduced, which is always a major problem in the presence of dye at room temperature. As with the dye (although more slowly), we observed buildup of deposits on the cell windows, thus, the sample position was moved after 5000 single scans. A typical example of the time dependent absorbance changes induced in a CALNN-NP solution is shown in Figure 3.6. An example of time dependent absorbance changes in a BR solution is also shown in Figure 3.6 for comparison.

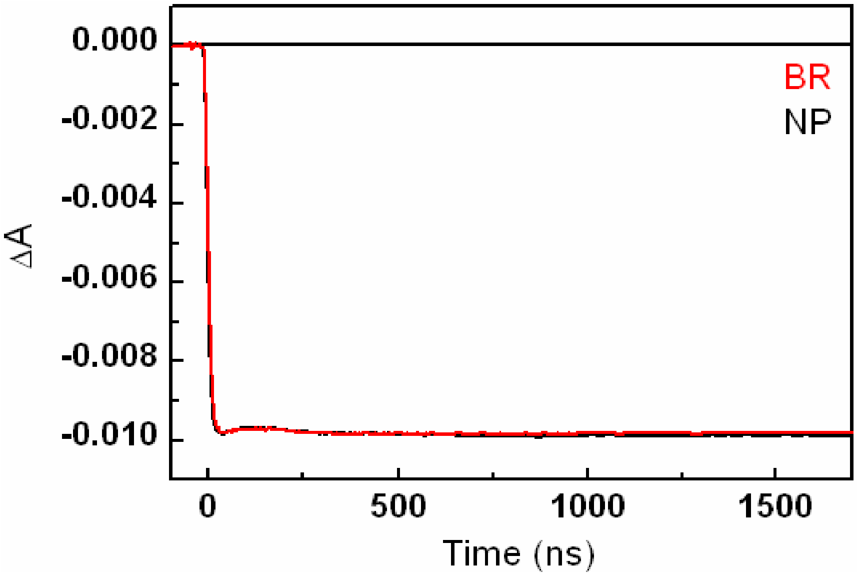

Figure 3. 6: Time dependent absorbance changes observed at 1584 cm^{-1} after a temperature jump of ~4 ^{o}C, induced by 5 ns laser pulses at 532 nm in ~4 x 10^{-6} M CALNN-NP (black) and ~5 x 10^{-4} M BR (red) in D_2O (50 µm path length) at room temperature. The NP curve was scaled to the BR curve for comparison.

As shown in the Figure 3.6, the two curves are virtually identical. The absorbance decrease is due to the shift of the D_2O absorption band with temperature. The absorbance change appears instantaneously within the response time of our temperature jump setup and then remains essentially constant up to the millisecond time scale, when the sample cools due to heat diffusion[89]. As a note, we observed a drop of the temperature jump signal within the first 20 x 128 single scan measurements when using CALNN-NP. This drop in signal was bypassed by discarding the first 20 x 128 measurements before analysis.

We also tested other nanoparticles, namely CT_8-NP and PEG-NP. The CT_8-NPs are more stable than CALNN since they have longer peptide ligands to enhance stability and the PEG-NPs are ideal for peptide studies since they have no peptide as capping ligands. Unlike with CALNN-NPs, we did not observe a drop in the temperature jump signal after 20 x 128 single measurements when using CT_8-NPs and PEG-NPs.

Although ideal for measurements, we found that once the nanoparticles were in solution, they have to be kept at room temperature before measurements. When the samples were stored below room temperature, we encountered an artifact during temperature jump measurements which is shown in Figure 3.7. A similar artifact was also observed when the sample was exposed to laser light in the same sample position for an extended amount of time (≥ 5000 single scans). This artifact is presumed to be due to aggregation of gold nanoparticles, most likely due to dissociation of the peptide ligands from the nanoparticles by pulsed irradiation (Levy and Volk, unpublished results).

In doing temperature jump measurements, we were able to induce temperature jumps of up to 5 ^{o}C in the presence of CALNN-NP and CT_8-NP and 3 ^{o}C in the presence of PEG-NP. We also found that while trying to obtain the highest temperature jump possible, the nanoparticles aggregate rapidly at pump pulse energies above 2 mJ.

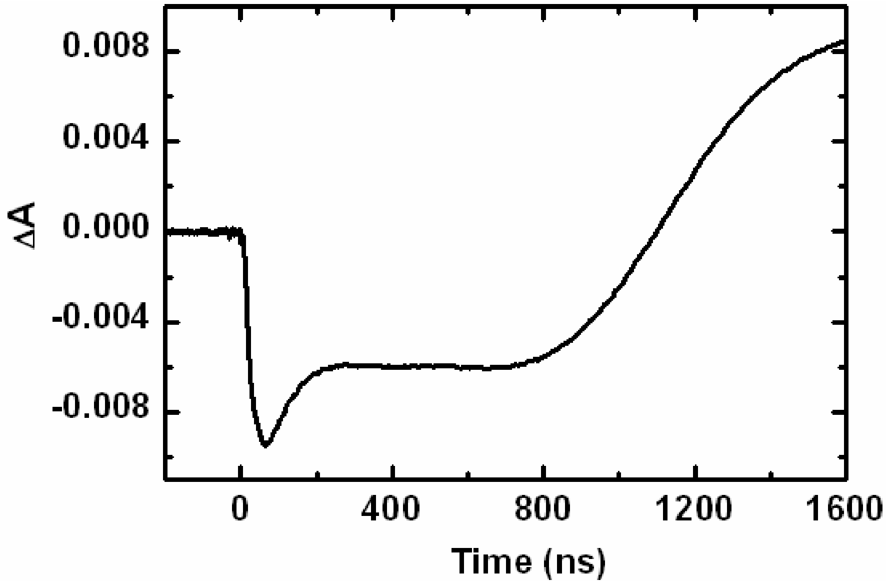

Figure 3. 7: An artifact observed at 1631 cm^{-1}, induced by 5 ns laser pulses at 532 nm (~4 x 10^{-6} M CALNN-NP in D_2O at room temperature, 50 µm path length) after sample had been stored in fridge for 2 days.

The nanoparticles were also tested in the presence of various NaCl concentrations (50 mM - 200 mM). We were able to induce reliable temperature jumps in CT_8-NP and PEG-NP solution containing 200 mM NaCl. The maximum temperature jumps that could be induced without encountering artifacts were ~5 ^oC and 3 ^oC for CT_8-NP and PEG-NP, respectively. On the other hand, CALNN-NP showed the same aggregating behavior as described above (Fig. 3.7) in the presence of 200 mM NaCl even for small temperature jumps. Thus, they cannot be used for inducing temperature jumps in the BBL protein sample investigated in chapter 4, which require the presence of 200 mM NaCl.

3.6 Helix-Coil Relaxation in the Presence of PEG-Nanoparticles

Having found that the peptide- and poly-ethylene glycol- capped gold nanoparticles seem to be a promising idea for inducing temperature jumps in peptide/protein samples, we chose to take temperature jump measurements on a peptide which was investigated previously using the direct heating method in the presence and absence of heat transducing dye. Here we used PEG-NP, as the peptide under investigation is positively charged. We investigated the folding dynamics of an alanine-based α-helical peptide, AR_4, in the presence of PEG-NP.

3.6.1 FT-IR Spectrum of AR_4

The peptide AR_4 investigated is a typical alanine based peptide. The FT-IR spectrum of AR_4 in D_2O at pD 1.5 containing PEG-NP is shown in Figure 3.8. The low pD 1.5 measured in the sample is due to the presence of the highly acidic trifluoroacetic acid (TFA). This is not an unusual occurrence, since TFA is used during the preparation process of the peptide. The band at 1675 cm^{-1} shown in Figure 3.8 is associated with the presence of TFA.

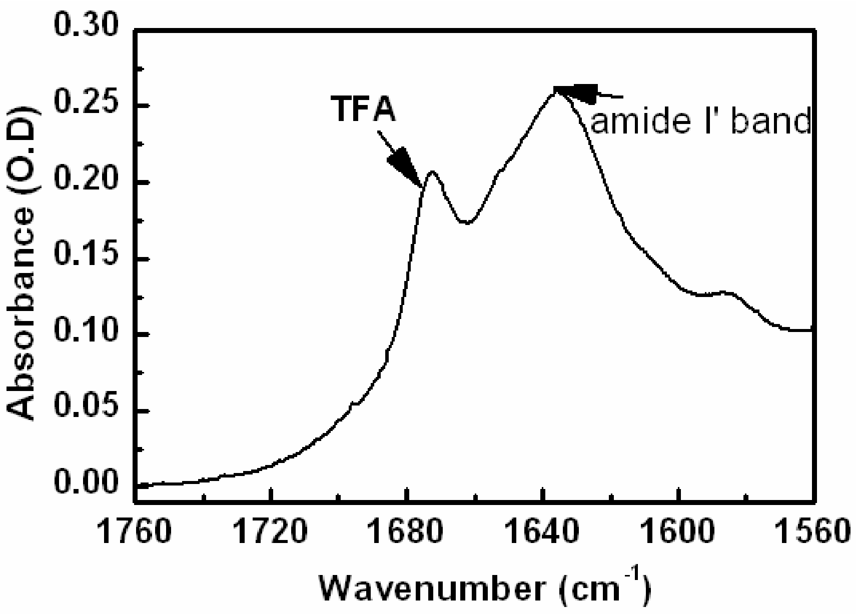

Figure 3. 8: FTIR spectrum of AR_4 (10 mg/ml) in PEG-NP(4 x 10^{-6})/D_2O solution (pD 1.5, 50 μm path length) at room temperature. The peak at ≈1675 cm^{-1} is due to TFA counterion.

It was shown by Pozo Ramajo and coworkers[89] that as temperature is increased, the amide I' band near 1635 cm^{-1} broadens and shifts to higher frequencies. Their results showed that AR_4 undergoes a well-characterized temperature induced transition from α-helical to disordered conformation.

3.6.2 Relaxation Dynamics of the Helix – Coil Transition of AR_4

It has been shown previously that the indirect heating of water by visible laser pulses in the presence of a triphenylmethane dye is a good method for investigating the folding dynamics of peptides and proteins[101, 104]. It was later proven by Pozo Ramajo that the indirect heating of D_2O by visible laser pulses is as valid for inducing temperature jumps as using direct heating of D_2O[89, 92], since the heat transducing dye was found to have no effect on the helix-coil transition dynamics of the alanine-based peptide AR_4. Here, we performed experiments on the peptide AR_4 in the presence of PEG-NPs.

Figure 3.9 shows an example of a temperature jump measurement taken on peptide AR_4, using temperature jumps of 2 °C in the presence of PEG-NPs.

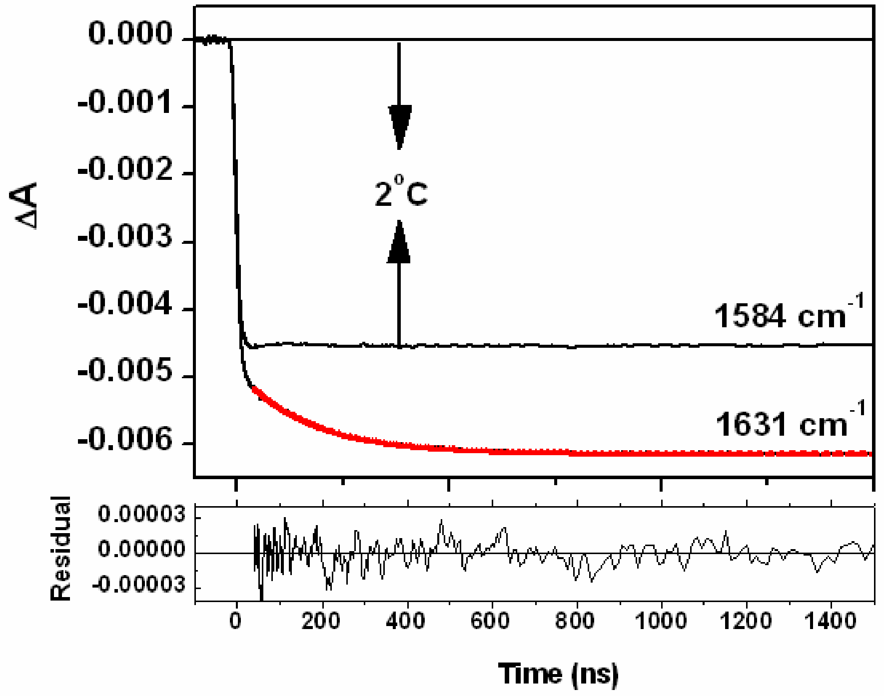

Figure 3. 9: Time dependent absorbance changes for peptide AR_4 (~10 mg/ml) in PEG-NP (4×10^{-6} M)/D_2O (pD 1.5, 50 µm path length) after a temperature jump from 22 °C to 24 °C induced by 5 ns laser pulses at 532 nm. Shown are the absorbance changes at 1584 cm^{-1} and 1631 cm^{-1}. The red line on top of the 1631 cm^{-1} measurement is the mono-exponential fit in the time window of 40 – 1500 ns, giving a time constant of (168 ± 13) ns. The residuals of the fit are also shown. The data shown are corrected for cooling, as described in chapter 2.4.1.

The instantaneous absorbance change at 1584 cm^{-1} is due to the shift of the D_2O absorption band with temperature. This absorbance change remains essentially constant up to the millisecond time scale (data not shown), when the sample cools due to heat diffusion[94]. The 1584 cm^{-1} measurement is used for calibration of the size of the temperature jump, since only D_2O has significant absorbance at this wavenumber, with strong temperature dependence. The size of the temperature jump was calibrated using the temperature dependent D_2O FTIR spectra as discussed in section 2.3, giving a temperature increase of 2 ^{o}C in this measurement.

In the presence of peptide AR_4, the absorbance changes at 1631 cm^{-1} are more complex than the absorbance change at 1584 cm^{-1}. In addition to the absorbance change observed at 1584 cm^{-1}, two additional features were observed from the amide I' absorbance of peptide AR_4. The first is an additional instantaneous absorbance decrease within the time resolution of our setup. This instantaneous change is due to the temperature induced shift of the amide I' frequency of the peptide backbone[60, 64, 90, 93] due to the breaking of hydrogen bonds between the peptide carbonyls and water molecules at higher temperatures[19]. The second absorbance decrease on the 100 ns timescale arises from the melting of the helical structures following an increase of temperature.

It was observed that although cooling occurs mostly on the microsecond to millisecond timescale, a decrease of the D_2O absorbance change at 1584 cm^{-1} was noticeable on the timescale relevant for helix-coil dynamics[89, 92]. This was assigned to the onset of cooling. The onset of cooling also distorts the 1631 cm^{-1} measurement and needed to be corrected for before fitting could take place. This correction was done by dividing the 1631 cm^{-1} by a correction function obtained from the D_2O absorbance change at 1584 cm^{-1} (further discussion in section 2.4.1), as opposed to subtraction of the absorbance changes observed in D_2O in a matched cell[60, 64, 93]. The red curve is the mono-exponential fit that describes the relaxation process of the peptide AR_4. The helix-coil relaxation in peptide AR_4 at 24 ^{o}C was found to have a time constant of (168 ± 13) ns.

For a temperature jump from 20 ^{o}C to 22 ^{o}C, we observed an increase in the helix-coil relaxation time constant from (168±13) to (179±6) ns. This observation is correct since the helix-coil relaxation is an activated process. Recently in our group, Sapna Sharma[20] investigated the dependence of the helix-coil dynamics on temperature for the peptide AR_4. She showed that the temperature induced relaxation of the peptide AR_4 is well characterized by an Arrhenius temperature dependence with an apparent activation energy of ~8 kcal/mol, predicting an increase of the relaxation time by 10% when lowering the temperature by 2 ^{o}C.

The helix-coil dynamics of peptide AR$_4$ in the presence of PEG-NP (indirect heating method) and in the presence and absence of BF dye (direct heating method)[89, 92] were compared. Figure 3.10 shows the time-dependent absorbance changes in the region of interest for the peptide AR$_4$ sample. The absorbance changes of the peptide samples containing BF dye or PEG-NP were scaled to the curve containing no heat transducer (black curve).

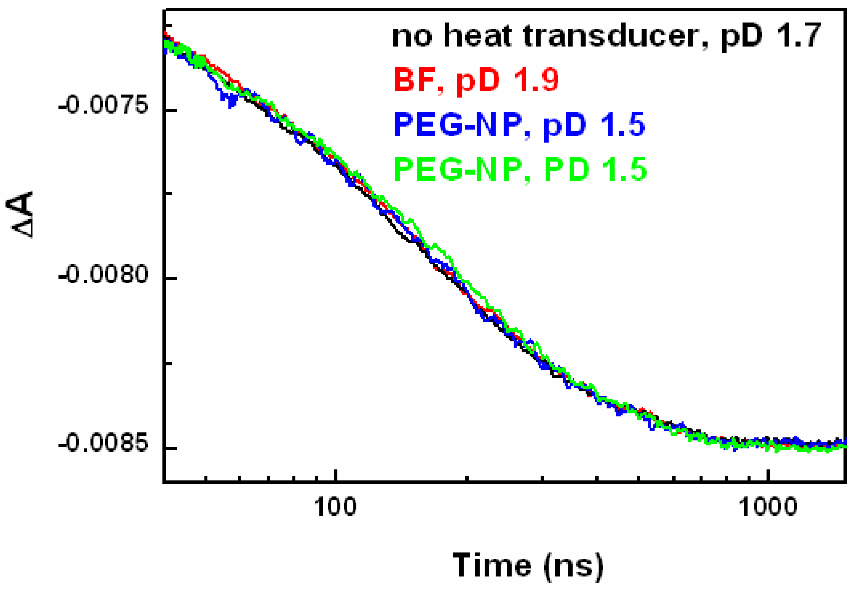

Figure 3. 10: Time dependent absorbance changes at 1631 cm^{-1} for peptide AR$_4$ in D$_2$O containing no heat transducer, ~4 x 10^{-6} M PEG-NP, or ~5 x 10^{-4} M BF. The black and red curves are representative of temperature jump measurements in the absence and presence of BF dye from 20 ^{o}C to ~22.5 ^{o}C, induced by 7 ns laser pulses at 1970 nm[89, 92]. The blue and green curves are temperature jump measurements in the presence of PEG-NP from 22 ^{o}C to 24 ^{o}C and 20 ^{o}C to 22 ^{o}C, respectively, induced by 5 ns laser pulses at 532 nm. The curves BF and PEG-NP were scaled to the curve obtained in the absence of heat transducers for comparability.

Although these results were obtained at slightly different pD values, Pozo Ramajo[89] showed that the helix-coil relaxation time constant of AR$_4$ varies only very slightly with pD, (by ~2 ns between pD 1.5 and pD 1.9), which can be neglected here. As shown in Figure 3.10, the four curves are very similar. The relaxation dynamics of the peptide AR$_4$ are identical within the noise (see Fig. 3.10 and Table 3.1), which confirms that the presence of a heat transducer does not affect the helix-coil dynamics of the peptide. Table 3.1 summarizes the temperature jump, the solvent conditions, and the helix-coil relaxation time constants for all samples.

Table 3. 1: Summary of the temperature jump experiments carried out on peptide AR_4 in the absence of heat transducers and in the presence of PEG-NP or BF dye[89, 92]. Given are the temperature jumps, heat transducer concentrations, pD values and time constants.

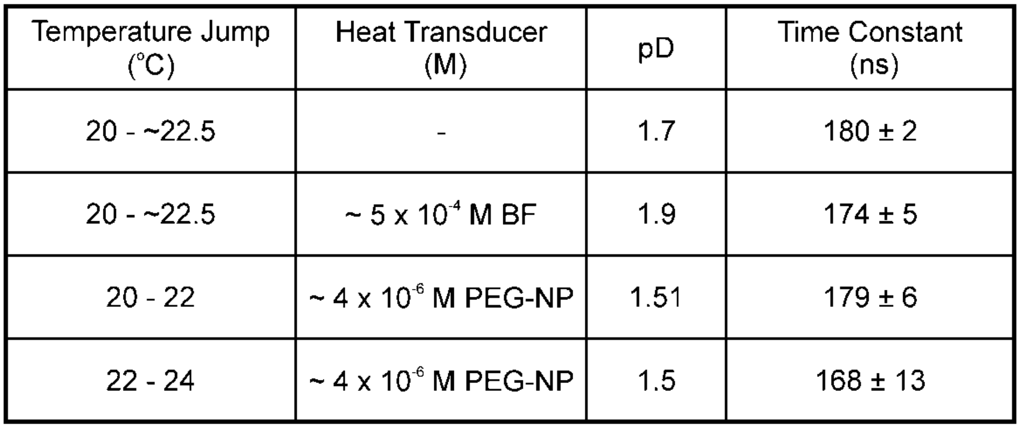

Temperature Jump (°C)	Heat Transducer (M)	pD	Time Constant (ns)
20 - ~22.5	-	1.7	180 ± 2
20 - ~22.5	~ 5 x 10^{-4} M BF	1.9	174 ± 5
20 - 22	~ 4 x 10^{-6} M PEG-NP	1.51	179 ± 6
22 - 24	~ 4 x 10^{-6} M PEG-NP	1.5	168 ± 13

From the results shown here, we conclude that the helix-coil dynamics of the peptide AR_4 are not affected by the presence of PEG-NPs and the results are identical to previous results.

3.7 Conclusions

We have investigated a triphenylmethane dye, peptide-capped gold nanoparticles and poly-ethylene glycol-capped gold nanoparticles as heat transducers for inducing temperature jumps in protein/peptide samples. Triphenylmethane dyes have been proven to be successful for inducing temperature jumps in peptide and protein solutions. However, several artifacts arose, such as cavitation and photo-bleaching, which cannot be ignored. On the other hand, capped gold nanoparticles were tested here for the first time and they were more successful than the triphenylmethane dye, even though artifacts still arose under certain conditions.

We also showed that high ionic strength affects the solubility of the basic fuchsin dye and causes the peptide-capped gold nanoparticle CALNN-NP to aggregate when irradiated. On the other hand, CT_8-NP and PEG-NPs were both stable at high ionic strength.

We also confirmed that the helix-coil dynamics of the peptide AR_4 was not affected by the presence of PEG-NPs or the use of the indirect heating method. The helix – coil relaxation was found to be (179±6) and (168±13) ns for a temperature jump of 2 ^{o}C from 20 ^{o}C and 22 ^{o}C, respectively and the results are identical to the helix-coil relaxation found in literature[89, 92].

CHAPTER 4: DYNAMICS OF PROTEIN BBL

4.1 Introduction

The protein BBL is the peripheral subunit binding domain (PSBD) of 2-oxo-acid dehydrogenase from Escherichia coli[124-126]. It is composed of two parallel α-helices (helix I and helix II) and a 3_{10}-helix (see Figure 4.1 below).

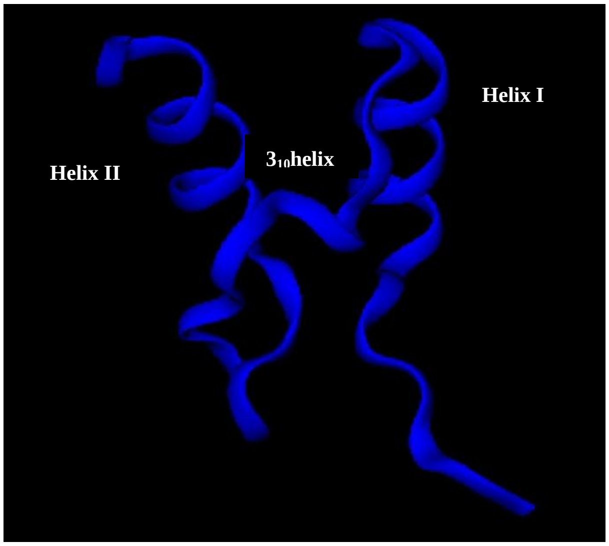

Figure 4. 1: Three dimensional structure of BBL (PDB ID: 1W4H).

The protein BBL was proposed by Muñoz and coworkers[126-130] to undergo a one-state downhill folding process; however, experimental results found by other groups argued against this principle[128, 131, 132]. The main results and their different interpretations are discussed below.

Muñoz and coworkers[126] studied the thermal unfolding of BBL, which led them to believe that BBL is a one-state downhill folder; downhill folders are proteins with an ensemble of conformations that lose structure gradually as the protein stability changes[126]. The evidence for one-state downhill folding was determined by measuring the thermal denaturation midpoints (T_m) of BBL, using far-ultra-violet circular dichroism (UV CD) spectroscopy, fluorescence resonance energy transfer (FRET), differential scanning calorimetry (DSC) and fluorescence quantum yield experiments. The protein construct investigated had 40 residues and experiments were carried out at pH 7 and without salt. It is important to note that an extrinsic fluorophore Naphthyl-alanine was introduced at the N-terminus (Naf-BBL) and for some experiments an additional dansyl at the C-terminus (Naf-BBL-Dan) since the original BBL construct lacks natural fluorophores.

The DSC experiments resulted in a broad unfolding temperature range (280 – 345 K) with the transition midpoint at ~322 K. The far-UV-CD spectra of BBL were investigated as a function of temperature in the range 273 – 363 K. At low temperatures the far UV-CD spectrum was found to be consistent with that of an α-helical structure with some random coil. At high temperatures the far UV-CD spectrum was found to be characteristic of a denatured protein. For the different temperatures studied, they observed a gradual, continuous shift from α-helix state to a denatured state, consistent with downhill folding behavior. Also, the transition midpoint was found to be ~8 K higher than the midpoint from their DSC results.

The FRET experiments revealed a transition midpoint at ~315 K. On the other hand, the fluorescence quantum yield data revealed no unfolding below 305 K. Above this temperature, the quantum yield decreased monotonically with increasing temperature, but did not reach a plateau even at the highest temperature (~363 K). Therefore, the authors observed different unfolding behavior with the different experimental methods used. Because of the differences, they concluded the protein is not a two-state folder, but exhibits a one-state downhill folding signature. Muñoz and coworkers also attempted to fit the data to a three-state model but also that did not work.

On the other hand, Fersht and coworkers[131] investigated a construct of BBL without labels and they showed that the protein folds cooperatively. The protein investigated was studied at pH 7 and 200 mM ionic strength; it had the following sequence:

WT-BBL: QNNDALSPAIRRLLAEHNLDASAIKGTGVGGRLTREDVEKHLAK

Unlike the BBL construct investigated by Muñoz and coworkers, four additional residues were included at the N-terminus (QNND). In investigating the non-labeled protein, they arrived at conclusions different from those of Muñoz and coworkers[126]. Fersht and coworkers investigated the thermal denaturation of BBL using several techniques, far-UV CD, H-NMR, ^{13}C-NMR, and DSC. They reported that the heat capacity changes occurred over a narrow temperature range and the transition melting point was located at 328 K, higher than the 322 K measured by Muñoz and coworkers[126]. Furthermore, thermal denaturation curves of BBL were shown to be cooperative when monitored by UV-CD at different wavelengths, ^{1}H-NMR and ^{13}C-NMR, and there was no evidence for the large spread of transition midpoints previously reported by Muñoz and coworkers[126]. Fersht and coworkers also showed that the extrinsic fluorophores used by Muñoz et al. perturbed the unfolding energetics of labeled BBL, altered the relative population of the conformational ensemble in the energy landscape and caused aggregation when studied at high temperatures and high protein concentration. Therefore, the experimental results suggest that the protein follows a two-state folding transition and not a one-state downhill folding transition as claimed by Muñoz and coworkers.

Naganathan et al[128] studied four modifications of the protein BBL using DSC and far-UV CD. The proteins Naf-BBL, Naf-BBL-Dan and WT-BBL were previously investigated, see above. The additional sequence investigated was Ac-Naf-BBL-NH_2 in which both ends are chemically protected. The DSC experimental results showed that the equilibrium thermal unfolding of Naf-BBL and NaF-BBL-Dan is completely reversible and has the same thermodynamic properties when studied under the correct experimental conditions (pH 7 and low ionic strength), in disagreement with Fersht's report that claimed that the labeling of BBL induced aggregation[131].

Naganathan et al[128] also analyzed the experimental results of Fersht and coworkers on the protein WT-BBL. They found that WT-BBL is not a two state folder even though this variant was found to be more stable.

The new variant of BBL in which both ends were chemically protected (Ac-Naf-BBL-NH_2) was also investigated. This new variant was introduced to determine whether the lower stability of Naf-BBL and Naf-BBL-Dan than WT-BBL arises from repulsive interactions between the charges at the peptide terminals or whether the lack of QNND at the N-terminal removed important native interactions. They found that Ac-Naf-BBL-NH_2 has the same thermodynamic stability as WT-BBL and exhibited the equilibrium signatures of downhill folding. Therefore, they concluded that extrinsic labels do not perturb the thermodynamic properties of BBL. Furthermore, regardless of the protein's stability and specific protein tail, they claimed that the protein was consistently found to fold downhill.

Neuweiler et al[133] used temperature jump fluorescence spectroscopy in combination with chemical denaturation experiments for following microsecond and nanosecond folding kinetics of three single point tryptophan mutants of WT-BBL (A130W, L131W, and H142W). The mutations A130W and L131W were found to affect the protein stability. However, the H142W single point mutation did not induce any measurable perturbation[132]. Their experimental results showed that the thermal and chemical denaturation curves of WT-BBL and WT-BBL-H142W are identical and that they fold cooperatively.

Neuweiler et al observed that the fluorescence transients of the three mutants exhibited a single-exponential decay with relaxation times in the range of 5 – 14 μs when the folding kinetics was monitored using resistive-heating temperature jumps. To observe whether an additional fast phase coexists for the three mutants, Neuweiler et al used a laser temperature jump technique with nanosecond time resolution. Using the nanosecond temperature technique, they found no evidence for an additional fast phase. For all three mutants, they observed that the denaturant-dependent microsecond transients followed chevron plots which could be fitted to a two-state transition. Therefore, they concluded that WT-BBL folds via a two state transition.

Arbely et al[124] investigated the energetic and structural perturbation effects upon protonation of histidine (His166) as a function of pH using heteronuclear NMR spectroscopy and far UV-CD spectroscopy. Their results showed that the thermal melting point of BBL was reduced by 10 K between pH 7 and pH 5.3 with an apparent decrease of ~0.9 kcal/mol in free energy of denaturation ($\Delta G_{D\text{-}N}$) at room temperature. Furthermore, the difference in stability measured by guanidine hydrochloride (GDmCl) denaturation showed that the protein BBL loses helicity between pH 7 and pH 5.3 with an apparent decrease of $\Delta G_{D\text{-}N}$ by ~1.1 kcal/mol. Another important result is that at pH 5.3, i.e. close to the pKa of His166, the protein exists in a mixture of two different native states.

More recently, Li et al[129] investigated the protein conformational dynamics of BBL. They performed nanosecond temperature jump experiments probing the end-to-end distance using FRET and the backbone structure using IR absorption. Their FRET experiment revealed two components. The first component was found on the ~100 ns time scale. They pointed out that the fast nanosecond component is similar to the hydrophobic collapse relaxation of acid denatured BBL[134]. The second component was observed on the tens of microsecond time scale and they assigned this to the global unfolding of BBL. Unlike the FRET results, where two components were observed, they claimed that only a single microsecond component was found in their IR results. Li et al assigned the microsecond component to overall unfolding of BBL. However, their claim of only a single microsecond component in the IR results is incorrect, as discussed in chapter 4.3.2.2.

Thus, studies on the protein BBL have shown to be very controversial between the two groups, where Muñoz and coworkers[126, 128-130] claimed that BBL is a downhill folder and Fersht and coworkers[131, 135, 136] claimed that BBL folds cooperatively in a (quasi-) two state process. In spite of the many studies on the protein BBL, very little has been done on investigating fast kinetics of this protein. Thus, the aim of this project is to use temperature jump coupled with TR-IR spectroscopy to determine whether a fast component exists in the folding of the protein BBL.

4.2 Materials and Methods

4.2.1 Protein Synthesis

The protein WT-BBL

(GSQNNDALSPAIRRLLAEHNLDA-SAIKGTGVGGRLTREDVEKHLAKA) was overexpressed in E. coli BL21 cells and purified by Eyal Arbely[7] using standard protocols by Maniatis et al[137]. The BBL samples were lyophilized in eppendorfs and used in our lab as received.

---

[7] Collaborator at Cambridge University

4.2.2 Buffer Preparation

The buffer solutions in D_2O (50 mM phosphate buffer at pD 7 and pD 5.2, respectively) were also prepared by Dr. Eyal Arbely. The ionic strength of the buffer solutions was adjusted to 200 mM by addition of potassium chloride (KCl).

4.2.3 Sample Preparation

Protein samples were prepared at a concentration of ~10 mg/ml in solutions of ~4 x 10^{-6} M CT_8-NP in phosphate buffer solution at pD 7 and pD 5.2. Immediately after preparation, the samples were transferred to a home-built IR cell with 50 µm path length; FT-IR spectra before and after dynamic measurements were recorded.

Temperature dependent FT-IR spectra of BBL in CT_8-NP/Phosphate buffer at pD 7 were recorded by Dr. Eyal Arbely[1]. His results showed that the presence of the nanoparticles does not affect the protein unfolding transition

4.2.4 Temperature Jump Measurements

Immediately after preparation, ~100 µl of protein solution was placed in a home built temperature controlled IR cell with 50 µm path length. Temperature jumps of up to 2 ^oC were induced in the sample using a nanosecond Nd:YAG laser (532 nm, 2 mJ, 5 ns). Temperature jump experiments were carried out at 30 to 65 ^oC (in 5 ^oC steps) at pH 7 and at 25, 45 and 50 ^oC at pH 5.2. Absorbance changes following the temperature jumps were monitored at 1584 cm^{-1} and 1631 cm^{-1}. After cooling correction and pressure relief correction, the absorbance changes were fitted tri-exponentially (see Chapter 2.2). Detailed descriptions of the correction for cooling and pressure relief are given in section 2.5.1 and 2.5.3, respectively. An example of the pressure relief correction is shown in Figure 4.2. Figure 4.2 shows the time dependent absorbance changes of a ~10 mg/ml BBL sample after a temperature jump of ~1.5 ^oC in CT_8-NP/D_2O solution at 1584 cm^{-1} where the blue and magenta curves are the uncorrected data and the corrected data, respectively, and at 1631 cm^{-1}, where the black and the red curves are the corrected and uncorrected data, respectively.

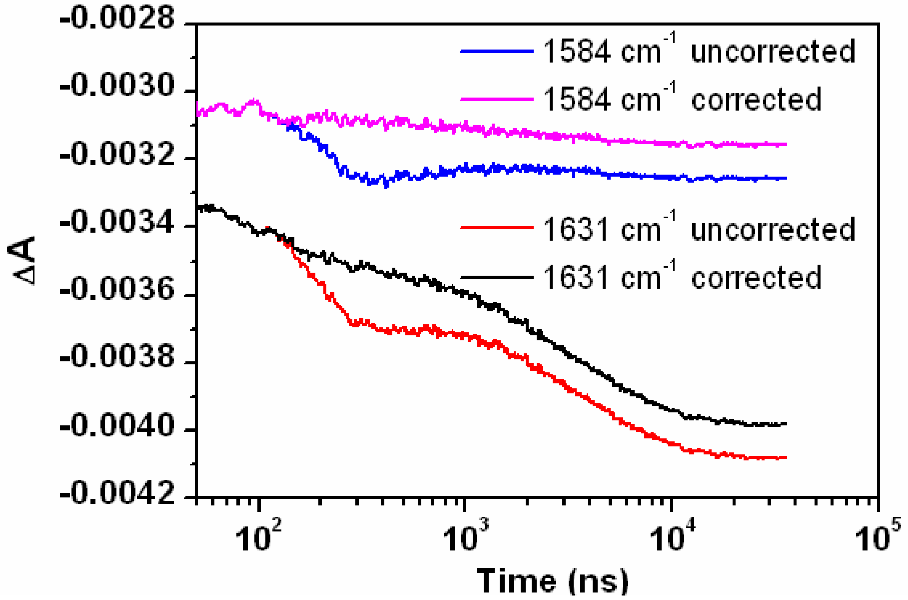

Figure 4. 2: Pressure relief correction for the time-dependent absorbance changes at 1584 and 1631 cm^{-1} after a temperature jump of ~1.5 °C from 55 °C in ~10 mg/ml BBL (50 µm path length, ~4 x 10^{-6} M CT$_8$-NP/D$_2$O). The magenta and black curves are the corrected data and the blue and red curves are the uncorrected data. The data were logarithmically averaged and corrected for cooling.

At 1584 cm^{-1}, the major absorbance decrease is due to the absorbance of D$_2$O which decreases with increasing temperature. In addition to this instantaneous absorbance decrease, a further decrease was observed during the first few hundred nanoseconds due to pressure relief followed by a slight recovery, due to pressure recovery (Figure 4.2, blue curve, see also Chapter 2.4.3). The D$_2$O absorbance then remains constant until it recovers on the millisecond time scale as the sample cools due to heat diffusion (data not shown). As a note, BBL has a small absorbance at this wavenumber. Therefore, after the instantaneous absorbance change, additional absorbance change could be expected to occur on the nano- and microsecond time scale, in parallel to those observed at 1631 cm^{-1}, which indeed is seen in the Figure 4.2 (magenta curve).

At 1631 cm^{-1} (red curve), the measured absorbance decrease is larger than the absorbance decrease at 1584 cm^{-1} (blue curve), signifying that a nanosecond phase is hidden beneath the pressure relief. Applying the pressure relief correction should reveal this hidden phase. As shown in the black curve, after pressure relief correction, the remaining absorbance changes on the nanosecond time scale can be clearly identified, which are due to an absorbance decrease of the protein.

The pressure relief correction does limit the accuracy of our numerical results to some extent. Nevertheless, the main features on the 100 nanosecond time scale which are observed can be relied on, see the quality of the pressure relief correction in the absence of protein, shown in Chapter 2.4.3.

4.3 Results and Discussions

4.3.1 FT-IR Spectra

The protein studied here is WT-BBL. The FTIR spectra before measurements (black) and after measurements (red) are shown in Figure 4.3. FTIR spectra of the protein sample were taken immediately after preparation and after completion of temperature jump measurements. The FTIR spectrum taken after the temperature jump measurements was found to be almost identical to the FTIR spectrum taken before temperature jump measurements.

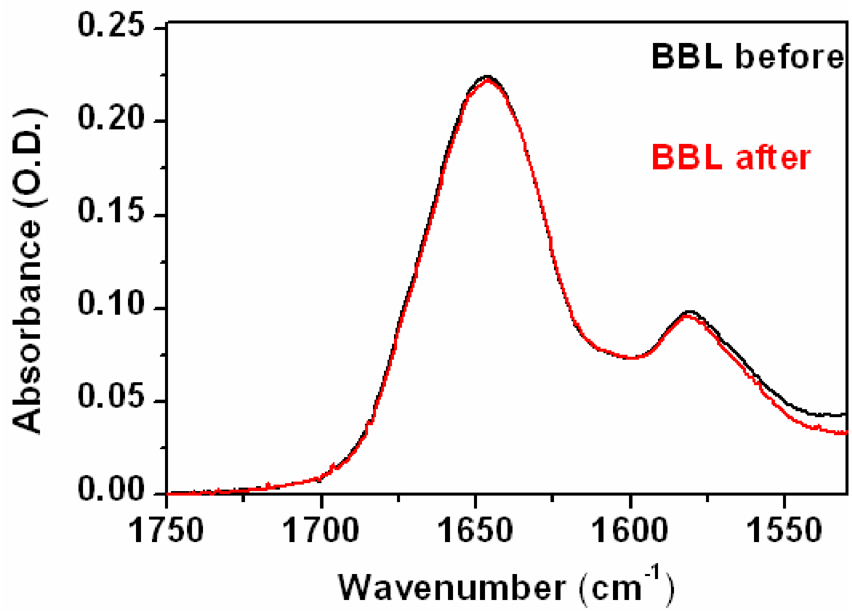

Figure 4. 3: FT-IR spectra in the amide I′ band of protein WT-BBL in D_2O/CT_8-NP (~10 mg/ml, pD 7, 50 µm path length, 200 mM ionic strength) recorded before (black) and after (red) the temperature jump measurements.

Figure 4.4 shows the temperature dependent FTIR-spectra of BBL in the amide I′ spectral region between 15 and 90 ^{o}C[8]. As shown, the amide I′ band gradually broadens and shifts to higher frequencies upon increasing temperature (Figure 4.4 a). Due to the fact that the absorbance changes are so small, it is very difficult to identify the changes of the various structural components. Therefore, in order to indentify the amide I′ components, difference spectra were generated by subtracting the spectrum at 15 ^{o}C from the spectra at the subsequent temperatures (Figure 4.4b). The band centered at ~1630 cm^{-1} corresponds to the α-helical structure of the protein backbone. The band disappears due to melting of the α-helical structures with increasing temperature. The band at 1675 cm^{-1} corresponds to the disordered structure of the protein in accordance with literature assignments. The band appears due to an increase in the disordered structure with increasing temperature.

---

[8] Measurements taken by Eyal Arbely at Cambridge University

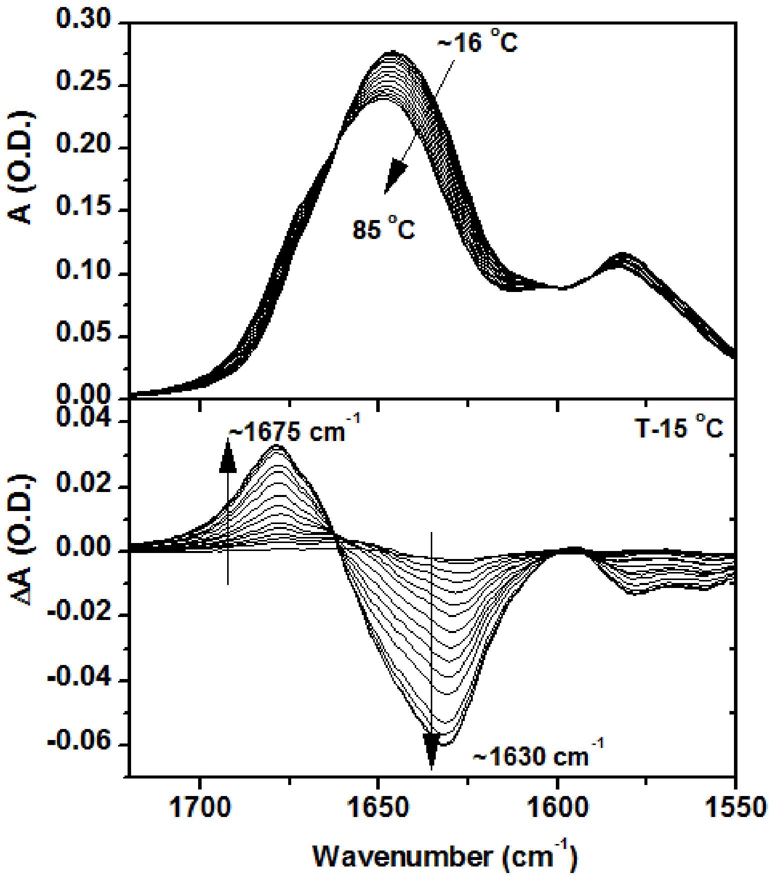

Figure 4. 4: Temperature dependent FT-IR spectra in the Amide I region of WT-BBL in D_2O/CT_8-NP (2 mM WT-BBL, ~4 x 10^{-6} M CT_8-NP, 0.05 M phosphate buffer, pD 7, 50 µm path length, 200 mM ionic strength)[9].

The thermal denaturation of BBL in the presence of CT_8-NPs was monitored by FTIR spectroscopy. The melting temperature for the protein BBL was determined by fitting the data in Figure 4.5 to a two-state equation. The melting temperature of protein BBL is exactly as expected (328 K). This means that during thermal denaturation, there is no interaction between the protein and the nanoparticle.

---

[9] Measurements taken by Dr. Eyal Arbely, Cambridge University.

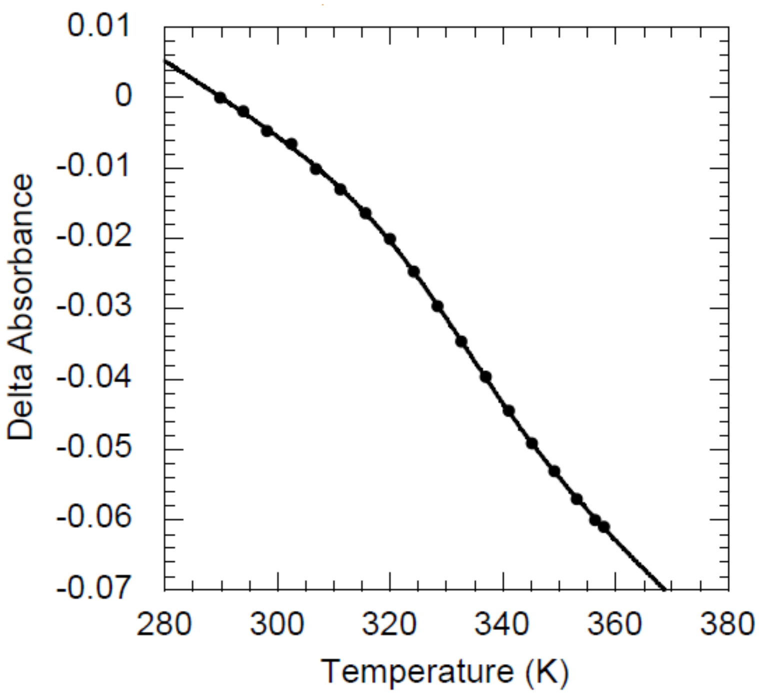

Figure 4. 5: Thermal denaturation of BBL monitored at 1630 cm^{-1} (2 mM BBL, ~4 x 10^{-6} M CT$_8$-NP, 0.05 M phosphate buffer, pD 7, 200 mM ionic strength , 50 µm path length) with a transition midpoint at 328 K. Delta Absorbance is the absorbance at temperature T – absorbance at 15 ^{o}C.

4.3.2 Temperature Dependent Relaxation Dynamics

4.3.2.1 Results

Temperature jump measurements were carried out on protein BBL in the presence of heat transducer, CT$_8$-NP, at 1584 and 1631 cm^{-1} at pD 7 and 5.2. Dynamic studies were carried at these two pD values so as to search for possible causes of irregularities in BBL's denaturation and dynamic behavior. The protein BBL is very stable at pD 7 and high ionic strength (200 mM). On the other hand, the protein loses stability at pD 5.2. Furthermore, experimental results have shown that the folded protein is found in a near-equal mixture of two different states at pD 5.2[124].

The measurement at 1584 cm^{-1} (see Figure 4.2), where D$_2$O has a significant absorbance and the protein contribution is very small (see Figure 4.4), exhibits an instantaneous absorbance decrease with an increase in temperature. This absorbance decrease is due to the shift of the D$_2$O absorbance band with temperature. This absorbance change appears instantaneously within the time resolution of our setup and then remains constant up to the millisecond timescale when the sample cools due to heat diffusion (data not shown). The change of the absorbance band at 1584 cm^{-1} was used to measure the size of the temperature jump (see discussion in Chapter 2.3) to be ~1 ^{o}C for measurements at pD 5.2 and ~1.5-2 ^{o}C for measurements at pD 7.

At 1631 cm^{-1}, the major absorbance decrease arises from the absorbance of D_2O, which decreases with the increasing temperature due to the shift of the D_2O absorbance band with temperature. In addition to the instantaneous absorbance decrease of D_2O, four additional dynamic components were found in the time resolved IR absorbance changes at 1631 cm^{-1} after a temperature jump (see Figures 4.6 and 4.7): (i) an additional instantaneous absorbance decrease (not shown in Figure 4.6 and 4.7), (ii) an absorbance decrease on the ~100 ns time scale, (iii) an absorbance increase on the ~500 ns timescale, and (iv) an absorbance decrease on the microsecond time scale.

Figures 4.6 and 4.7 show the time dependent absorbance changes in the region of interest, the tri-exponential fit results in the time range of 100 ns to 36 μs and the corresponding residuals obtained for the BBL samples on which temperature jump experiments were carried out, namely for pD 7 and pD 5.2. As shown, the tri-exponential fits describe the relaxation process very well and the residuals of the tri-exponential fits to the relaxation at the different temperatures confirm that the fit is good (see Figure 4.6 and 4.7).

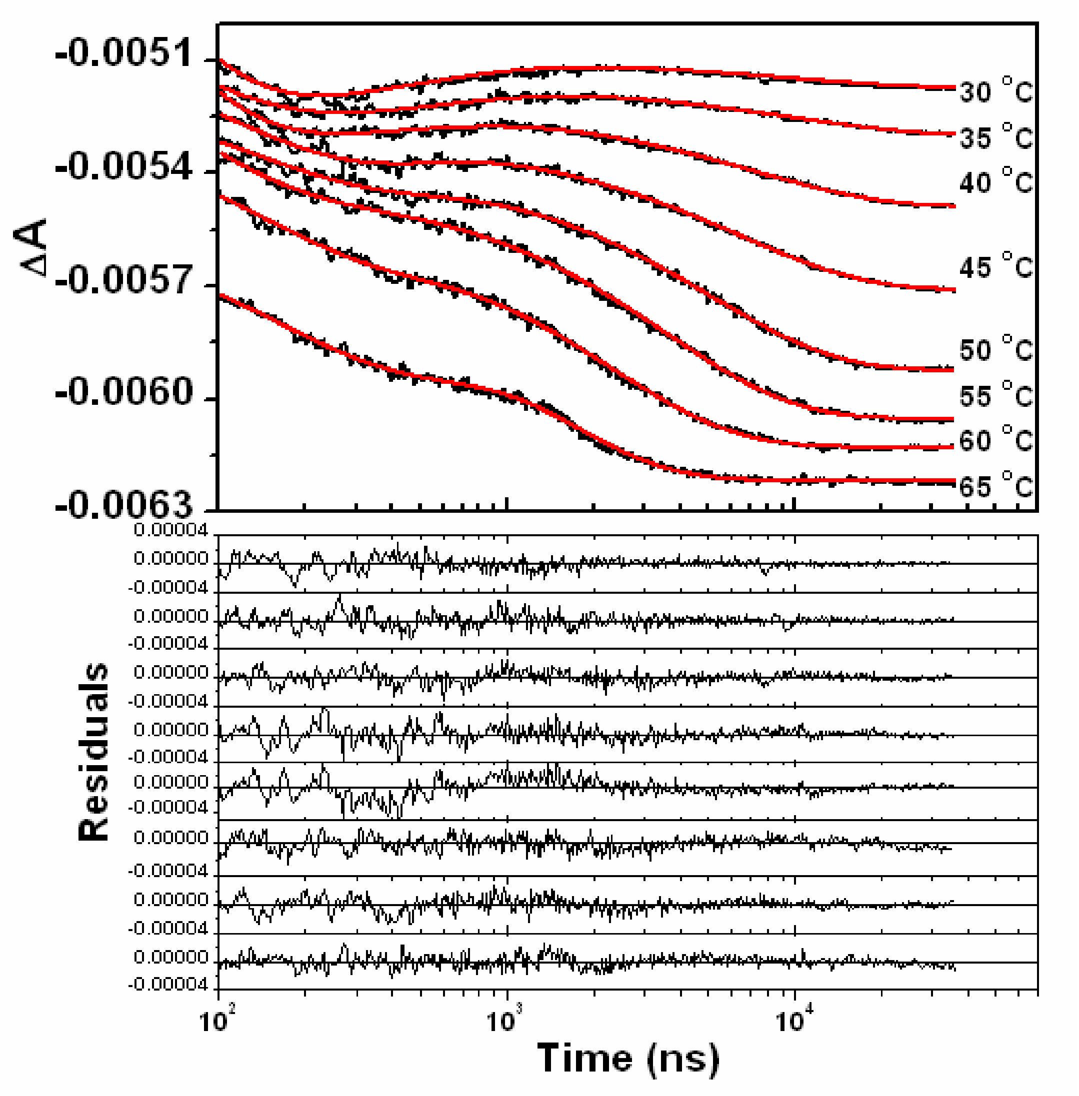

Figure 4. 6: Time-dependent absorbance changes at 1631 cm^{-1} after a temperature jump of 2 °C from 30 – 65 °C in ~10 mg/ml WT-BBL (50 µm path length, ~4 x 10^{-6} M CT_8-NP/D_2O, pD 7), induced by ~5 ns laser pulses at 532 nm. The experimental results were logarithmically averaged, cooling corrected and pressure relief corrected. They were then scaled so that the absorbance changes correspond to a temperature jump of 2 °C from all temperatures. The curves were also shifted slightly so that the curves do not overlap. The tri-exponential fit results are shown in red. The residuals are shown in the order of increasing temperature from 30-65 °C from top to bottom.

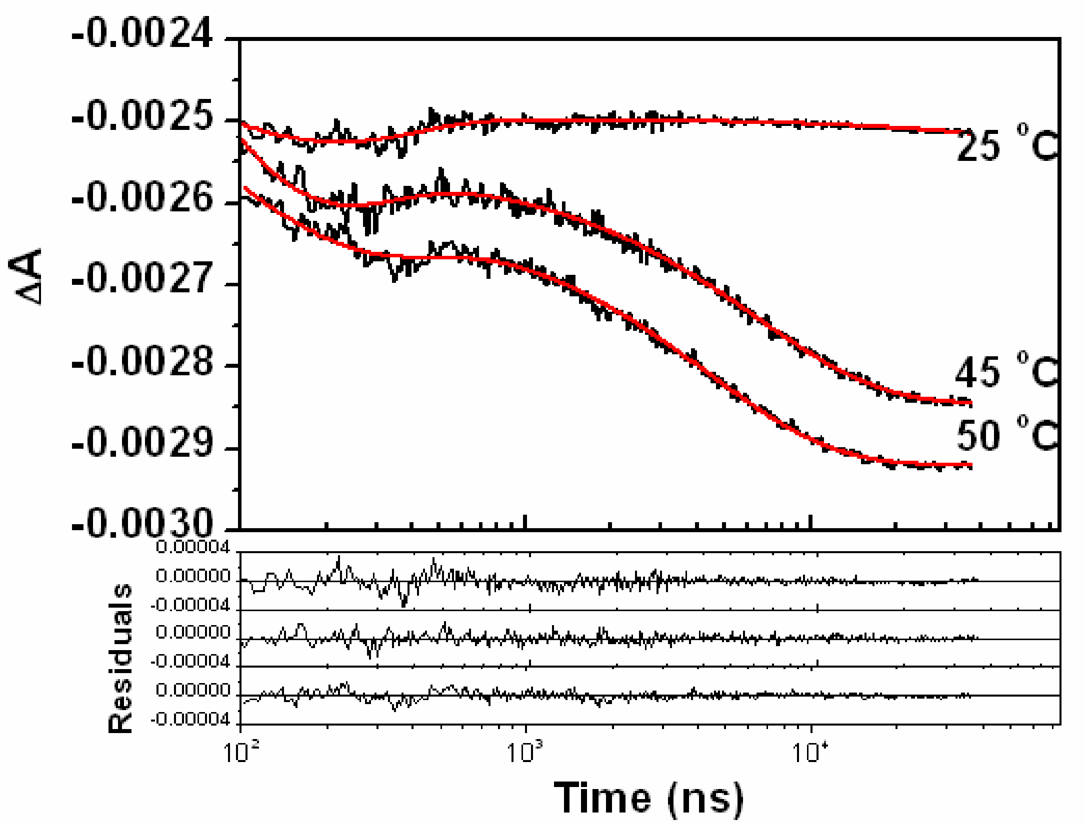

Figure 4. 7: Time-dependent absorbance changes at 1631 cm^{-1} after a temperature jump of 1 °C from 25, 45 and 50 °C in ~10 mg/ml WT-BBL (50 µm path length, ~4 x 10^{-6} M CT$_8$-NP/D$_2$O, pD 5.2), induced by ~5 ns laser pulses at 532 nm. The experimental results were logarithmically averaged, cooling corrected and pressure relief corrected. They were then scaled so that the absorbance changes correspond to a temperature jump of 1 °C from all temperatures. The curves were also shifted slightly so that the curves do not overlap. The tri-exponential fit results are shown in red. The residuals are shown in the order of increasing temperature 25 – 50 °C from top to bottom.

The first component is an absorbance decrease which is instantaneous within our time resolution of tens of nanoseconds after an increase in temperature. This absorbance decrease is too rapid to be ascribed to the helix-coil relaxation. We suggest that the additional instantaneous absorbance bleach originates from the protein due to a shift of the amide I′ frequency with temperature which has been observed previously[19, 20, 59, 64, 92, 93].

The absorbance of BBL at 1631 cm^{-1} decreases further on the nano- to microsecond time scale with three kinetic phases. The relaxation time constants obtained from the tri-exponential fits are shown in Table 4.1 and 4.2 for pD 7 and pD 5.2, respectively. The amplitudes, normalized against the size of the temperature jumps, are shown in Figure 4.8.

Table 4. 1: Relaxation time constants and the errors obtained from tri-exponential fits of the temperature jump measurements on BBL at pD 7.

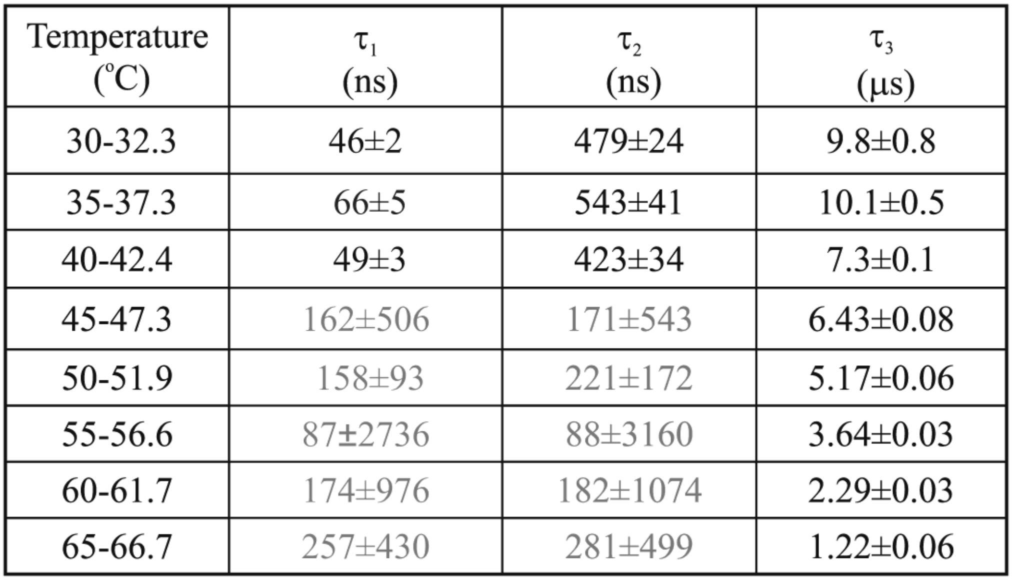

Temperature (°C)	τ_1 (ns)	τ_2 (ns)	τ_3 (μs)
30-32.3	46±2	479±24	9.8±0.8
35-37.3	66±5	543±41	10.1±0.5
40-42.4	49±3	423±34	7.3±0.1
45-47.3	162±506	171±543	6.43±0.08
50-51.9	158±93	221±172	5.17±0.06
55-56.6	87±2736	88±3160	3.64±0.03
60-61.7	174±976	182±1074	2.29±0.03
65-66.7	257±430	281±499	1.22±0.06

Table 4. 2: Relaxation time constants and errors obtained from tri-exponential fits of the temperature jump measurements on BBL at pD 5.2.

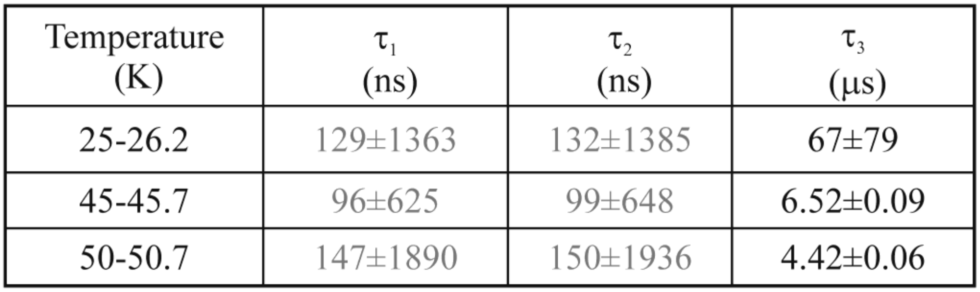

Temperature (K)	τ_1 (ns)	τ_2 (ns)	τ_3 (μs)
25-26.2	129±1363	132±1385	67±79
45-45.7	96±625	99±648	6.52±0.09
50-50.7	147±1890	150±1936	4.42±0.06

The first phase of absorbance decrease occurs on the hundred nanosecond time scale (Table 4.1 and 4.2, τ_1 = ~100 ns). This absorbance decrease is assigned to the structural relaxation of the protein backbone at higher temperature, which results in the unfolding of solvated helical stretches in agreement with relaxation times observed on helical proteins[138-141] and helical peptides[24, 32, 34, 60, 63, 64, 85, 88-90, 142].

The second phase is an absorbance increase and it also occurs on the nanosecond time scale. This absorbance increase is only clearly observed at temperatures 30 – 40 ^{o}C (τ_2 = ~500 ns) and it could possibly be ascribed to an increase in partially solvated helix structure, i.e. buried helices (amide I′ ~1645 cm^{-1}) get somewhat exposed to the solvent and thus their amide I′ band shifts to lower frequency (~1630 cm^{-1}). This would indicate loosening of the protein structure so that the protein backbone becomes more solvent accessible in agreement with the transition state structure determined by Φ-value analysis[132]. The Φ-values of BBL were found to be similar along the entire sequence with loosely formed native-like interactions and high helical content in the transition state. On the other hand, the nanosecond components at 45 – 65 ^{o}C, pD 7 and all temperatures at pD 5.2 cannot be well resolved. This is because very similar time constants (Table 4.1 and 4.2, τ_1 andτ_2) with very large errors and very large amplitudes with opposite signs were found (data not shown).

Since the fit yields similar time constants and amplitudes of opposite signs for the pD 7 data at high temperatures and at pD 5.2, a bi-exponential fitting function was used to fit each dynamic traces, but these fits were not satisfactory. This indicates that there is indeed another dynamic process which cannot be separated by the tri-exponential fits. It is possible that the two time constants are getting closer to each other or the 500 ns component's amplitude gets smaller as the temperature is increased. Unfortunately, there is no reliable way of quantifying the contribution of each of these processes from the fits, making the interpretation of the results impossible. Given that it is not possible to clearly identify the two nanosecond components, especially at higher temperatures, the amplitude of the fast component in Fig. 4.8 was obtained directly from the difference in the signals at 100 ns and 1 μs. As shown in Figure 4.8a, the amplitude of this component increases with increasing temperature with no evidence of a plateau.

Finally, the third phase is an absorbance decrease on the microsecond time scale (Table 4.1 and 4.2, τ_3). This phase can be assigned to the global unfolding event of the protein BBL in agreement with previous results for BBL[129, 132, 133] and other helical proteins[58, 138, 141]. The amplitudes of the microsecond component were found to increase with increasing temperature with a maximum near the transition midpoint (Figure 4.7b), in agreement with the thermal melt results within the experimental uncertainty of our measurements.

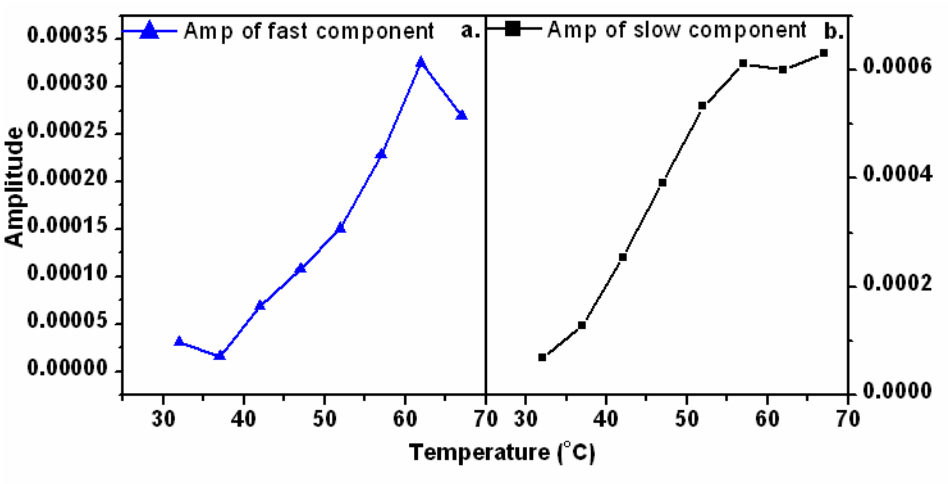

Figure 4. 8: The amplitude contributions of the fast and slow phase at various temperatures and pD 7. The amplitude of the fast component was obtained from the difference of the signals at 100 ns and 1μs. The amplitude of the slow component was obtained from the tri-exponential fit. The amplitudes were normalized against the size of the temperature jump, to correspond to a temperature jump of 2 °C at all temperatures.

Previous kinetic studies have considered the global unfolding of helical proteins to be a two-state process with 1/τ as the apparent rate constant[138]. Thus, if τ is measured at different temperatures, the apparent activation energy (E_a) can be determined from the Arrhenius equation as shown in equation 4.1:

$$k(T) = A * e^{-E_a / RT} \tag{4.1}$$

where $k(T)$ is the rate constant as a function of temperature, A is a pre-exponential factor, E_a is the activation energy, R is the ideal gas constant and T is the temperature in Kelvin.

The plot of the logarithm of the rate constant (inverse of the relaxation time in seconds) against the inverse of the temperature in Kelvin (Figure 4.9) shows an Arrhenius dependence of the temperature jump induced relaxation kinetics of BBL, with the activation energy of 11±0.1 kcal/mol. However, there seems to be a slight deviation from Arrhenius behavior, probably indicating that the unfolding transition of BBL is more complex.

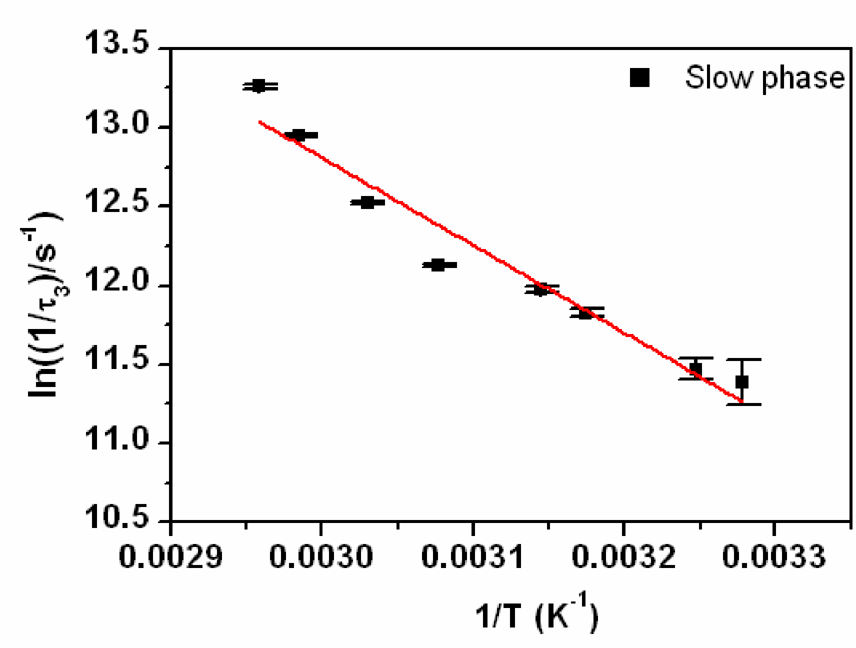

Figure 4. 9: Plot of $\ln(1/\tau_3)$ of the slow phase versus 1/T. The red line shows the best linear fit to the data.

4.3.2.2 Discussion

The time dependent IR kinetic results clearly showed that three distinct phases are observable for the unfolding transition of BBL at both pD 7 and pD 5.2. In a simple multi-state scheme, the three distinct phases require at least four states to describe the folding and unfolding of BBL. This can be described by the following model:

$$\mathbf{U} \xrightleftharpoons{\tau_1 = \text{~}100\text{ ns}} \mathbf{I_1} \xrightleftharpoons{\tau_2 = \text{~}500\text{ ns}} \mathbf{I_2} \xrightleftharpoons{\tau_3 = \text{~}1\text{-}10\ \mu\text{s}} \mathbf{F}$$

where U is the unfolded state, I_1 and I_2 are the intermediate states and F is the folded state. The relaxation time constants are the measured time constants at various temperatures. It is worth mentioning that the relaxation time τ_2 is only evident at 30 – 40 ^{o}C. The relaxation time, τ_3, decreases with increasing temperature. As shown in the model above, the relaxation process between U and I_1 occurs very rapidly on the ~100 ns time scale. This phase corresponds to the unfolding of solvated helix segments, and the time is in agreement with that found helical peptides and proteins. On the other hand, the relaxation process between I_1 and I_2 is ~5 times slower than the first phase. This relaxation process is observed here for the first time and we suggest that it reflects buried helix segments getting exposed to the solvent. Finally, the relaxation process between I_2 and F is characteristic of the global unfolding of BBL. As shown in Figure 4.10, the global unfolding rate is very sensitive to temperature, over the range of 30 – 65 ^{o}C and the relaxation time exhibited an approximate Arrhenius temperature dependence.

Our fast nanosecond results can be compared to recent results on a variant of BBL. In 2009, Muñoz and coworkers studied the dynamics of dansylated and non-dansylated BBL using FRET and IR absorption temperature jump experiments. A fast nanosecond component was observed for the dansylated BBL (Naf-BBL-Dan) using a FRET probe[129]. In that study, Muñoz and coworkers assigned the ~100 ns component to the hydrophobic collapse of the protein denatured state. Furthermore, the amplitude of the fast component was shown to increase linearly with temperature[129, 134]. The ~100 ns relaxation time constant observed in our study for the protein WT-BBL is similar to the nanosecond lifetime observed for the dansylated BBL[129]. Also, the amplitude of our nanosecond component showed a similar trend to the one observed in that study (see Figure 4.8a). Even though the relaxation time and the amplitudes are similar to the results observed by Muñoz and coworkers, it is reasonable to suggest that the nanosecond component is due to helix unfolding and not hydrophobic collapse and that Muñoz' interpretation is wrong. This is because hydrophobic collapse should not occur when a protein is denatured by increasing the temperature, which reduces hydrophobic interactions (except in the region of cold denaturation, which is at much lower temperatures).

Unlike the FRET data where results were reported on the nanosecond time scale, IR data of the non-dansylated BBL (Naf-BBL) were not reported on the fast time scale in the paper by Muñoz and coworkers[129]. IR data were only reported on the microsecond time scale and Muñoz and coworkers claimed to have observed a single microsecond exponential decay (see Figure 4.10) with no faster component. This eliminates the possibility of comparing their IR results to ours on the nanosecond time scale; however, their claim of a single exponential is in contradiction to our results. For this reason, we determined whether their IR data were indeed well fitted by a single exponential decay as they claimed explicitly or whether they chose not to include data on the fast time scale due to some artifact.

We tested the validity of their claim of a single exponential decay by overlaying their experimental data with time dependent changes calculated using a single exponential function, Fig. 4.10. Figure 4.10 shows the transient measurements on a non-dansylated BBL measured by Muñoz and coworkers (Figure 2C of reference 129). As shown, the calculated time dependent changes (blue dotted curves) are in stark contrast with Muñoz and coworker's claim of a single-exponential decay – note the deviation from a single exponential at short delay times (highlighted in Fig. 4.10) for the measurements at the higher temperatures. We believe that some relevant information is hidden about a fast helix-coil relaxation of the protein and an artifact occurring on the nanosecond time scale (see Chapter 2.4.3). With this in mind, their wrong claim of an absence of a fast nanosecond IR component invalidates their analysis and claim that the protein is characteristic of one-state folding.

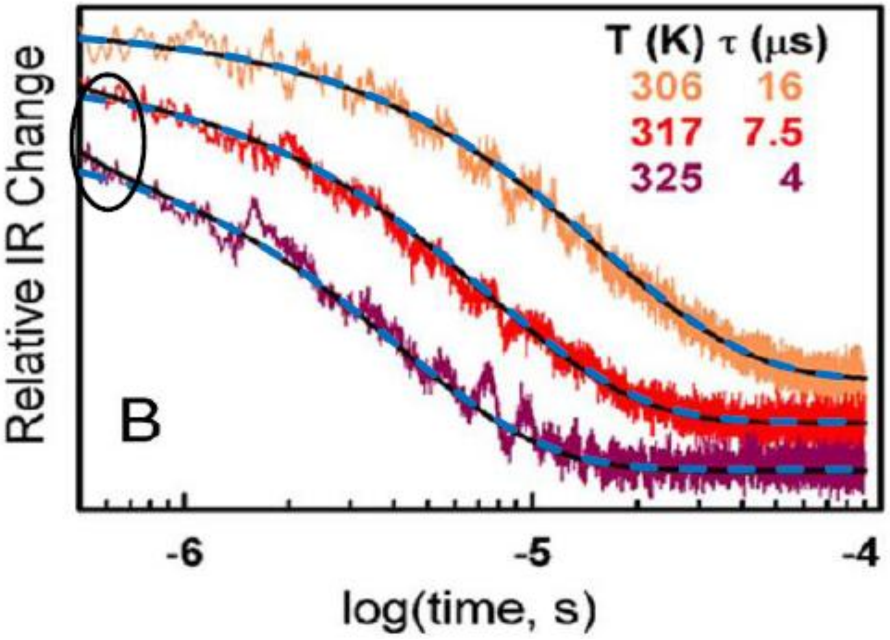

Figure 4. 10: Temperature dependent IR absorbance changes for Naf-BBL (60 μM, pH 7) measured by Muñoz and coworkers (Figure 2C of reference 129). The supposedly single exponential fits are shown as black solid curves[129]. The blue dotted curves are calculated single exponentials. The circle on the nanosecond time scale is to guide the eye to the deviation from a single exponential.

Despite the failure to not report IR data on the nanosecond time scale, it is still possible to compare results on the microsecond time scale. The microsecond relaxation time observed for our WT-BBL is similar to the lifetime reported for the global unfolding of Naf-BBL[129]. Nevertheless, our time constants are slightly different (e.g. 5.2 µs vs. 4 µs at 325 K) – note that their experimental conditions are different to ours and the proteins investigated are slightly different[129]. Furthermore, the results also showed a similar trend where the relaxation time constant decreases with increasing temperature (see Figure 4.10).

Neuweiler et al[133] also published data on the kinetics of BBL; they undertook resistive-heating and laser temperature jump fluorescence measurements of folding as a function of denaturant concentration with microsecond and nanosecond time resolution, respectively, on a mutant, WT-BBL-H142W. In their work, the authors did not observe a fast nanosecond component at 298 K, indicating that the core of the protein does not unfold. This is in agreement with our interpretation of the fastest component being due to structural relaxation of the protein backbone which results from the unfolding of solvated helices. The second nanosecond component is also in agreement, being due to separation of helices, which would occur at the other end of the protein, away from the His142 (helix II). In any case, Neuweiler and coworkers[133] did not see the nanosecond components due to the fact that they are limited by their spectroscopic probe. Though a nanosecond component was not observed, a microsecond component was observed by Neuweiler et al[133], in close agreement with our observation.

Relaxation dynamics were investigated here at different pD values: pD 7 and pD 5.2. According to Eyal Arbely and coworkers[124], the protein BBL is less stable at pD 5.2 and it is comprised of a mixture of two native states. The authors showed that the mixture of two states occurs due to partial protonation of His166. However, our results showed that the dynamic features at pD 7 and pD 5.2 are almost identical within our experimental uncertainty. This is very different to the expectation of a faster kinetic phase at low pD[10]. Even if there is a difference in the stability, it does not seem to affect the kinetic behavior after a temperature jump.

---

[10] Eyal Arbely, Private communication

4.4 Conclusions

Here, the folding dynamics of the small protein BBL was investigated at various temperatures and pD 7 and pD 5.2 using TRIR spectroscopy. Our results showed three distinct phases: two nanosecond phases and one microsecond phase. The nanosecond phases are well separated at low temperature. However, above 40 ^{o}C, the nanosecond components are not easily distinguishable due to similarities in the time constants or one of them being too small. Nevertheless, the microsecond component was evident and it displayed slight deviation from an Arrhenius behavior. Our results also showed that the relaxation times are independent of pH. These results provide significant insights into the unfolding processes of the protein BBL.

CHAPTER 5:DISSOCIATION OF BACKBONE CAGED PEPTIDE

5.1 Background

Insights into the first steps of protein folding have increased in recent years because of the many experimental and theoretical methods that made it possible to go beyond the millisecond time resolution of standard stopped-flow or rapid mixing techniques. Central to experimental investigations of the fastest steps of protein folding is the development of fast triggering methods. Although various approaches have been used, most of these suffer from significant drawbacks: in particular, the most widely used method of laser-induced temperature jumps generally triggers unfolding.

Alternative fast folding triggers make use of photochemical methods. One recently suggested method is based on a photocleavage reaction that generates the desired functional group from an inactive one upon photolysis[77, 78, 80]. One main advantage of this method is that photolysis of a non-native nitrobenzyl results in the full protein, thus avoiding any potential distortion of the folding reaction by the phototrigger group itself, which cannot be ruled out for most other photochemical folding triggers.

In recent years, photosensitive protection has become an important tool in organic synthesis in which the photosensitive precursors are termed “caged compounds”[77, 78, 80, 143-163]. The most widely used caged compounds are based on the 2-nitrobenzyl derivative. The currently available caged compounds have the general structure (**A**) and they typically follow the mechanistic pathway shown in Scheme 5.1[144, 145, 147, 148, 151, 155, 159, 162, 164-166]. Upon photolysis of compound **A**, the primary photoreaction is the intermediate (**I_1**) which is known as “aci-nitro”. The formation of this intermediate **I_1** has been shown by several researchers to occur very rapidly (ps) via intra-molecular hydrogen transfer[161, 162, 167]. Flash photolysis experiments show that the aci-nitro intermediate **I_1** undergoes deprontonation to form **I_1^-** in pure water and pH 7 on the time scale of ~50 ns[143, 159, 161]. The deprontonation is due to the relatively low pKa of the aci-nitro intermediate[77, 154]. The aci-nitro intermediate then decays by forming a cyclic intermediate (**D**) and a subsequent hemiacetal (**E**) followed by release of the caged compound and the final nitroso product (**C**).

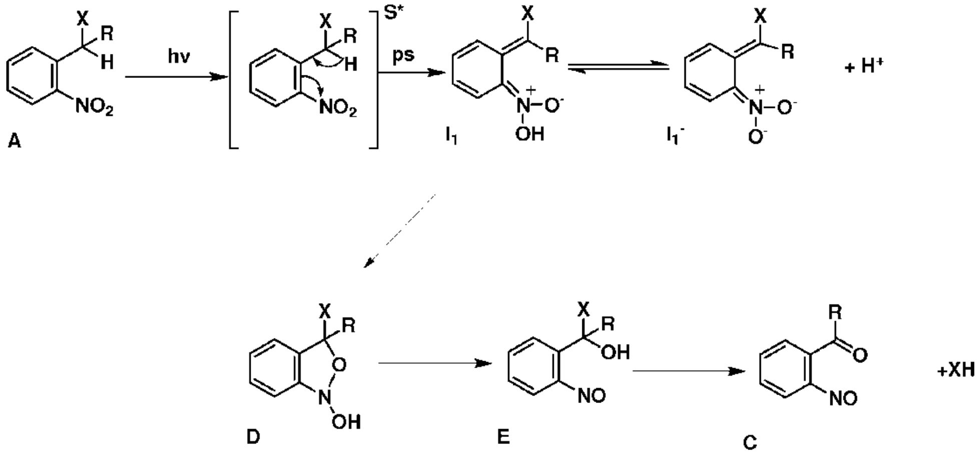

Scheme 5. 1: Schematic representation of the photoreaction of a nitrobenzyl caged compound; after Schwörer and Wirz[161], Pelliccioli and Wirz[159], and Gaplovsky et al[162].

One of the main reasons for developing caged compounds is the rapid release rate. However, the release rate is rarely known due to the fact that the photochemical reaction varies with substitution, solvent and pH. In one of the earliest study on a caged compound, Wootton and Trentham[168] found that ATP was released on the time scale of ~11 ms from nitrophenylethyl ATP at 20 °C and pH 7. With dimethoxy substituents on the benzene ring, the release time was even slower, ~50 ms at 20 °C and pH 7[168]. On the other hand, Trentham et al[169] investigated the photochemical reaction of yet another caged ATP. They found that ATP was released at a much faster rate, on the time scale of ~10 µs[169].

In an attempt to understand the mechanism of the photoreaction of 2-nitrobenzyl derivatives, several studies have been carried out in recent years on a series of model compounds using various techniques, which yielded the mechanism shown in Scheme 5.1 as the generally accepted mechanism. A summary of these studies is given below:

Using Laser flash photolysis (LFP) and time-resolved photoacoustic measurements, Abbruzzetti et al[143] investigated the deprotonation yields, decay rates, and pK_a of aci-nitro intermediates for *o*-nitrobenzaldehyde (NBA), 4-chloro-2-nitrobenzaldehyde (CNBA), 4,5-methoxy-2-nitrobenzaldehyde (DMNBA) and 4-formyl-6-methoxy-3-nitrophenoxyacetic acid (FMNA). Their LFP results indicate that the aci-nitro intermediates undergo deprontonation in water at pH 7 on the time scale of ~50 ns, depending on the exact compound under investigation. The deprontonation reaction is driven by the low pKa of the aci-nitro intermediate. For the compound NBA with pKa of 2.1, the aci-nitro intermediate was found to decay on the few nanosecond time scale after excitation. On the other hand, addition of electron donating methoxy substituents at the 4 and 5 position of the benzene ring resulted in lower deprotonation yields, slightly higher pKa, and slower decay rates of the aci-nitro intermediate on the 50 to 200 ns time scale. Conversely, addition of an electron withdrawing Cl atom at position 4 of the benzene ring was found to decrease the life time of the aci-nitro intermediate (**I_1**). Meanwhile, the deprontonation yield and the pKa were not affected by the presence of an electron withdrawing atom.

In 2002, Peng and Goeldner[170] synthesized and characterized three o-nitrobenzyl ethers of choline using UV/vis spectroscopy. The kinetics of the photolysis of the three compounds were analyzed by monitoring the formation and decay of the aci-nitro transient at 405 nm. The authors assumed that the decay of the aci-nitro intermediate to be a kinetic measure of the release of the choline based on previous studies[163]. The decay rates observed were different for the three and they were found to vary considerably with pH and the addition of substituents at the α-benzylic position. Peng and Goeldner observed a fast decay of the aci-nitro intermediate on the time scale of ~10 μs.

Il'ichev et al[155] investigated the mechanism of methanol photorelease from 2-nitrobenzyl methyl ether and 1-(2-nitrophenyl)ethyl methyl ether, and the release of ATP from adenosine-5'triphosphate-P^{β}-(1-(2-nitrophenyl)-ethyl) using laser flash photolysis (LFP), UV-vis and IR detection. The release of methanol was found, using fast scan IR spectroscopy and LFP, to proceed via three intermediates before forming the final compound (see Scheme 5.1): the primary aci-nitro intermediate (**I_1**), the 1,3-dihydrobenz(c)isoxazol-1-ol derivative (**D**) and 2-nitrobenzyl hemiacetal (**E**), followed by the release of methanol on the second timescale. Il'chev et al[155] reported an aci-nitro deprontonation time of ~370 ns for 2-nitrobenzyl methyl. The decay of the intermediate **E** limits the release of methanol up to pH 8 and 10 for 2-nitrobenzyl methyl ether and 1-(2-nitrophenyl)ethyl methyl ether, respectively. However, at pH values above 9, the release of methanol occurred parallel to the decay of the aci-nitro **I_1^-**. This means that the reaction steps D to C to E occurs faster and the release of the final product on the seconds time scale.

Gaplovsky et al[162] investigated the photochemical reaction mechanisms of 2-nitrobenzyl alcohol and 1-(2-nitrophenyl)ethanol in various solvents using TRIR spectroscopy. The photochemical reaction was shown to proceed via the primary aci-nitro intermediate, which decays by two competing paths. The first pathway followed the mechanism shown in Scheme 5.1, cyclization (**D**) followed by ring opening to the carbonyl hydrate (**E**). Dehydration of the carbonyl hydrate led to the formation of the final compound (**C**) on the seconds time scale. They showed that this reaction mechanism predominates in wet acetonitrile and near-neutral aqueous solutions. Furthermore, the authors showed that the aci-nitro intermediate ionizes very rapidly to form $\mathbf{I_1}^-$ within 50 ns when R = H. Conversely, when R = Me, aci-nitro decayed much more rapidly (on the sub-ns time scale).

On the other hand, the second pathway (not shown) is more specific to the compounds investigated (X = OH) and the pathway was found to be dependent on the reaction medium and pH. Gaplovsky et al[162] showed that the second pathway involved proton transfer from the enol to the aci-nitro function forming a nitroso hydrate. Dehydration of the nitroso hydrate was found to occur on the time scale of 1 ms. The researchers showed that the reaction via the second pathway predominates in hexane, dry acetonitrile and strongly acidic or basic solutions.

All evidence so far shows that the photocleavage reaction is relatively slow, on the time scale of milliseconds to seconds. However, all studies were done on compounds where the leaving group was linked to 2-nitrobenzyl derivative by C or O. When the leaving group is the amide group of a peptide (C—N), it is important to ensure that the release is sufficiently fast, especially when the principal interest is on triggering fast processes of folding. Wieboldt et al[171] investigated *o*-nitrobenzyl derivatives of urea using transient absorption spectroscopy to follow the rate of the photolysis reaction. The decay of the aci-nitro intermediate ($\mathbf{I_1}$) was assumed to be directly related to the rate of product release, based on previous results[163, 168]. They reported that urea was released on the time scale of 10 – 100 µs for the different derivatives. Wieboldt et al[171] also showed that the decay of the aci-nitro intermediate is pH dependent, similar to earlier studies[170]. On the other hand, Tatsu et al[79] investigated a caged sperm-activating peptide with a photocleavage protecting group on a backbone amide using LFP. A single exponential decay was observed in the absorption at 420 nm showing the decay of the aci-nitro intermediate. The half-life of the intermediate was found to be 26 µs. Again, Tatsu et al assumed that this half life of the intermediate is related to the photo-release of the leaving group[79, 150, 170].

So far, for all compounds where the leaving group is linked by a C—N bond, the authors have suggested that the reaction is faster (10 – 100 µs)[79, 171] than when the leaving group is linked by C or O[143, 155, 161, 162]. However, the authors only concluded this from the decay of the aci-nitro intermediate (**I_1**) using transient UV spectroscopy which gives no direct evidence for the formation of the final product. With the use of IR spectroscopy, it has been shown that the decay of **I_1** does not yield conclusive evidence for the release of the final product[155, 162].

For this reason, Rhee et al[80] investigated the photochemical reaction of a backbone caged peptide that is covalently bonded to a photolabile linker, 4,5-dimethoxy-2-nitrobenzyl (Scheme 5.2, compound **A)** using steady state FTIR absorption spectroscopy and time resolved FTIR in fast scan mode. Their FTIR data revealed two prominent amide I bands at 1622 cm^{-1} and 1639 cm^{-1}. Upon photolysis of compound **1**, the two bands merged into a singlet to form a new band at ~1635 cm^{-1}. This merge signifies the formation of the new peptide (**B**). On the other hand, their TRIR data revealed that cleavage of the backbone caged peptide occurs faster than their experimental time resolution (< 3 seconds). Also, their data showed that Scheme 5.1, does not apply to this reaction, since the cleaved peptide **B** appeared before the formation of the final product **C**.

Though Rhee et al[80] made an attempt to determine the release rate of the backbone caged peptide; they were limited by the time resolution of their set up. Here we investigated the rate at which the peptide is cleaved from the 4,5-dimethoxy-2-nitrobenzyl in the model peptide by Rhee et al[80] (see Scheme 5.2), using nanosecond time-resolved IR spectroscopy. Our experimental results show that the backbone caged peptide is cleaved within 50 ns, which indicates that nitrobenzyl photolysis is highly suitable for kinetic studies of even the fastest folding processes.

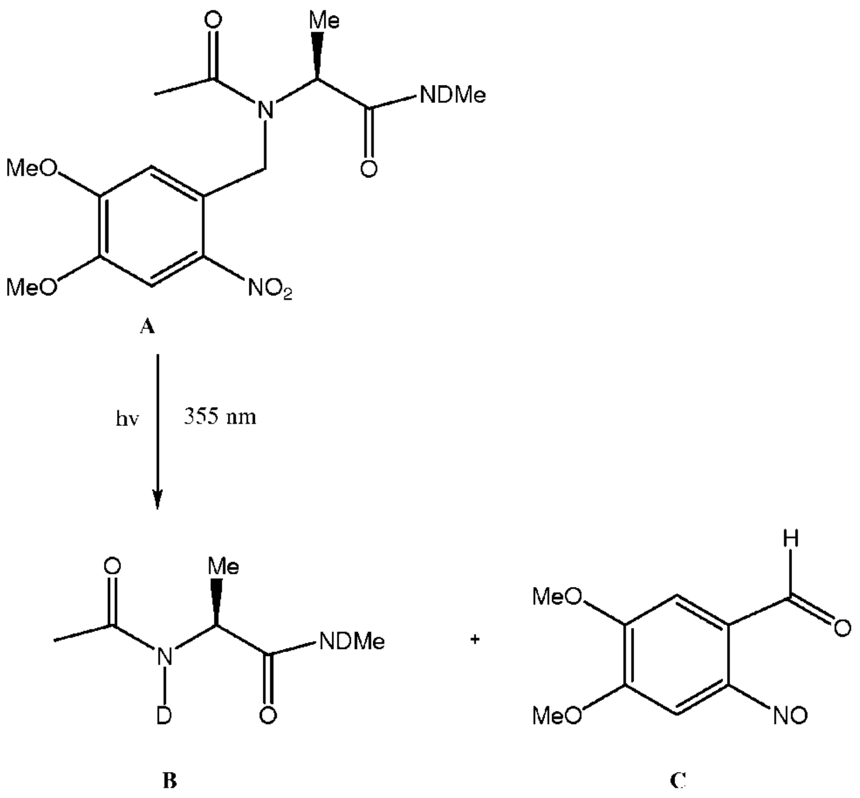

Scheme 5. 2: Schematic representation of the photocleavage reaction of compound A[80].

5.2 Materials and Method

5.2.1 Backbone Caged Peptide Synthesis

The backbone caged peptide was synthesized by Marina Gonzalez[11] following Rhee et al's[80] protocol and purified by Dr. James Gaynor[12] using thin layer chromatography (TLC). The synthesis of the backbone caged peptide was verified by UV-vis and FT-IR spectroscopy.

---

[11] Master student at the University of Liverpool, Chemistry department

[12] Post-doc at the University of Liverpool, Chemistry department

5.2.2 Backbone Caged Peptide Preparation

The backbone caged peptide solution was freshly prepared in the dark by dissolving ~10 mg of compound **A** in dimethyl sulfoxide (DMSO-d_6). The solution was stirred until compound **A** was fully dissolved. D_2O was then added to obtain a concentration of ~10 mg/ml peptide, 5% (w/w) DMSO-d6 and filtered with a 0.2 µm pore filter to remove any un-dissolved particles.

5.2.3 Monitoring the Photochemical Reaction of Backbone Caged Peptide

The solution of compound **A** (~50 µl) was placed in a small Harrick IR cell with CaF_2 windows (56 µm path length). The sample was exposed to ns-pulses from a Nd:YAG laser (355 nm, 20 mJ, 5 ns, 10 Hz repetition rate, beam diameter of 4 mm) for 5 minutes (in steps of 1 minute) at room temperature. During irradiation the sample cell was moved continuously so that the entire sample would be exposed to the laser light. After each irradiation step, the spectroscopic features of the photochemical reaction of compound **A** were monitored using FT-IR spectroscopy.

5.2.4 Time Resolved Infrared Measurements

Approximately 50 µl of compound **A** was placed in a small Harrick IR cell with a 56 µm path length. IR absorbance changes in compound A were measured after excitation by a nanosecond YAG laser (355 nm, 0.6 mJ, 5 ns). The absorbance changes following a laser pulse were monitored at eight different wavelengths between 1560 cm^{-1} and 1640 cm^{-1} in time windows of 0 ns – 1.7 µs, 10 ns – 89 µs and 10 µs – 89 ms. The sample was flowed continuously using a peristaltic pump to exchange the sample volume between each excitation pulse. If the sample is not flowed, only the simple temperature jump signal is observed, (see Chapter 3.6.2). A total of 5120 single scans were averaged to generate a curve for each wavelength and time window. No degradation occurred in the signal during the time in which single scans were obtained. The curves were logarithmically averaged to improve the signal-to-noise (see Chapter 3).

It is important to mention that the curves at the same wavelength on different time scales did not overlap and therefore need to be properly scaled. In order to do so, measurements in the longer time windows were scaled for overlap with scaling factor of

~1.01 to 1.07 for measurements taken on the same day. On the other hand, measurements taken on different days were scaled to each other with scaling factors in the range of ~0.9 to 1.4. After overlap, the curves were combined to obtain one single curve at each wavelength.

Finally, the combined curves at each wavelength were corrected for so that the spectrum of the absorbance changes on the long time scale corresponds to the D_2O difference spectrum between 23 and 21 ^oC. This is based on the assumption that the absorbance change is dominated by cooling on long time scale (see Chapter 2.4.1). The correction was obtained by subtracting the observed absorbance changes at 5 ms from the observed absorbance changes at 500 μs for each wavelength. The difference values were then plotted against wavelength and multiplied by individual scaling factors to obtain a spectrum that has the same shape as the D_2O difference spectrum between 23 and 21 ^oC. The scaling factors used were in the range of 0.8-1.35. As a note, the largest scaling occurred when there were notable breaks in data collection.

After all corrections were completed, the relaxation kinetics of compound A were fitted globally for all wavelengths by means of a non-linear least square (Levenberg-Marquardt) fitting routine in Microcal Origin. Sums of seven exponential functions with an offset were used to fit the relaxation kinetics of compound A in the time window of 30 ns to 4.2 ms (see Chapter 2.2). During global fitting, the time constants were shared between the wavelengths and they and the amplitudes were varied freely.

5.2.5 Photo-Acoustic Calorimetric Measurements

The dissociation of the backbone caged peptide was investigated by Jaroslava Mikšovská at Florida International University (FIU) using a photoacoustic calorimetric (PAC) technique[172]. The basic principle of PAC is that a photo-excited molecule dissipates excess energy via vibrational relaxation to the surrounding solution, which produces a transient heating of the reaction medium. A pressure wave is then transmitted through the cell due to the rapid increase in temperature which is then detected by a pressure sensitive detector[172]. The pressure wave is a result of the volume change (ΔV) which can be expressed by the equation:

$$\Delta V = \Delta V_{th} + \Delta V_{struct} \tag{5.1}$$

where ΔV_{th} is the thermal volume change, due to heat release to the solution. ΔV_{struct} is the volume change due to structural changes at the molecular level[173].

The thermal volume change of the solution (ΔV_{th}) can be described by the equation 5.2:

$$\Delta V_{th} = Q\frac{\beta}{Cp\rho} \tag{5.2}$$

where β is the thermal expansion coefficient of the solution, Q is the heat released to the solution, C_p is the heat capacity and ρ is the density. The amplitude of the sample acoustic wave (compound **A**) is described by the equation 5.3:

$$S = E_a K\left(Q\frac{\beta}{C_p\rho} + \Delta V_{struct}\right) \tag{5.3}$$

where E_a is the number of Einsteins absorbed by the sample, K is an instrumental response constant. A reference acoustic wave is also measured under the same condition as the sample acoustic wave to eliminate the instrumental response. As a note, the reference sample should undergo fast internal conversion, should be photochemically stable and capable of delivering the absorbed energy as heat[173]. With that, the amplitude of the reference acoustic wave is then given by equation 5.4:

$$R = E_a K E_{h\nu}\left(\frac{\beta}{C_p\rho}\right) \tag{5.4}$$

where $E_{h\nu}$ is the photon energy at 355 nm (80 kcal/mol). Therefore, the ratio of the amplitude of sample acoustic signal (compound **A**) to the reference amplitude is given by:

$$\frac{S}{R}E_{h\nu} = Q + \Delta V_{struct}\left(\frac{C_p\rho}{\beta}\right) \tag{5.5}$$

Finally, a plot of $S/RE_{h\nu}$ versus the ratio of $C_p\rho/\beta$ yields a linear relationship with a slope corresponding to ΔV_{struct} and an intercept corresponding to Q. $C_p\rho/\beta$ is highly temperature dependent in aqueous solution due to changes in the thermal expansion coefficient[173]. Therefore, measurements are taken at different temperatures between 16 and 35 ^{o}C. The reaction volume (ΔV) and enthalpy (ΔH) changes associated with the dissociation of the backbone caged peptide can be determined from the equations below

$$\Delta V = \frac{\Delta V_{struct}}{\Phi} \tag{5.6}$$

$$\Delta H = \frac{E_{h\nu} - Q}{\Phi} \tag{5.7}$$

where Φ is the quantum yield of the photoreaction.

5.3 Results and Discussion

5.3.1 UV-Vis and IR Band Assignment

Figure 5.1 shows the absorption spectra of compound **A** before and after the dynamic measurements. As shown in the Figure 5.1, the absorption at 355 nm decreases upon exposure to UV irradiation. As a note, our UV spectrum after irradiation is different to that observed by Rhee et al[80], in that there was no build-up of the product. This indicates that the ring product precipitates.

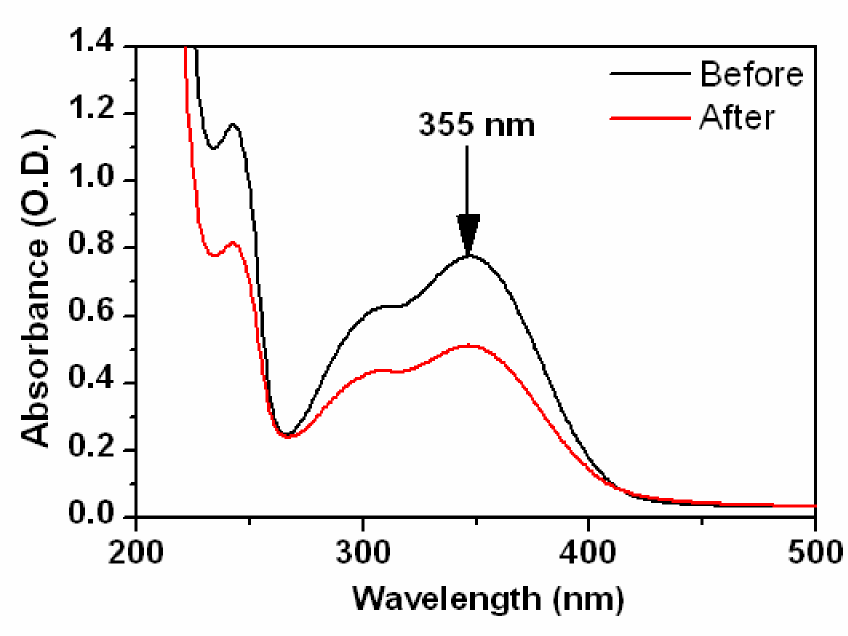

Figure 5. 1: UV-vis absorption spectra of compound A in D_2O, 5% DMSO-d_6 (~10 mg/ml, 56 µm path length). The black spectrum is before dynamic measurements and the red spectrum is after dynamic measurements.

Figure 5.2 shows the FT-IR spectrum of compound **A** and Table 5.1 shows the IR band frequencies and their assignments. There are two structurally sensitive bands associated with the backbone-caged peptide and six sensitive bands that are associated with the nitro moiety. Structural assignments are based on ab initio calculations of Cho and coworkers[80].

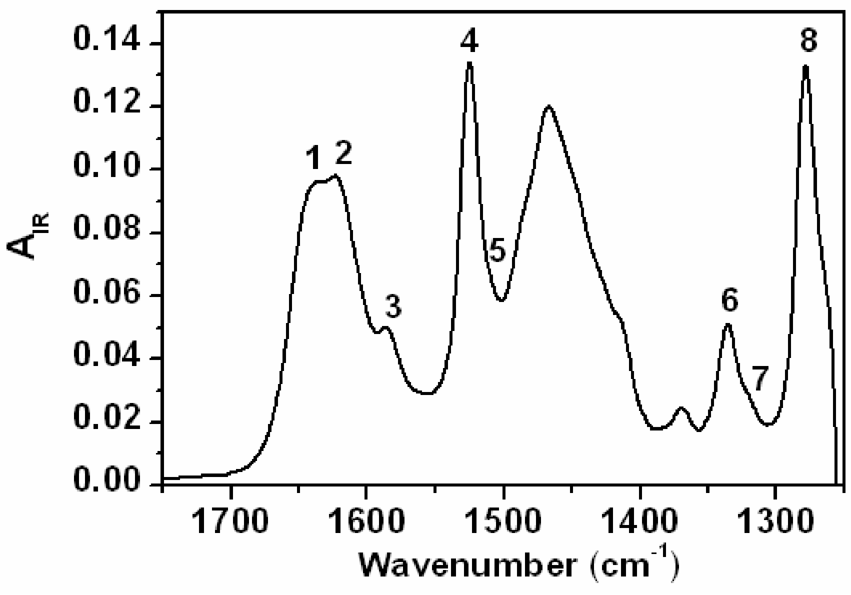

Figure 5. 2: FT-IR spectrum of compound A in D_2O/5% DMSO-d_6 (~10 mg/ml, 56 μm path length).

Table 5. 1: Measured IR frequencies of compound A.

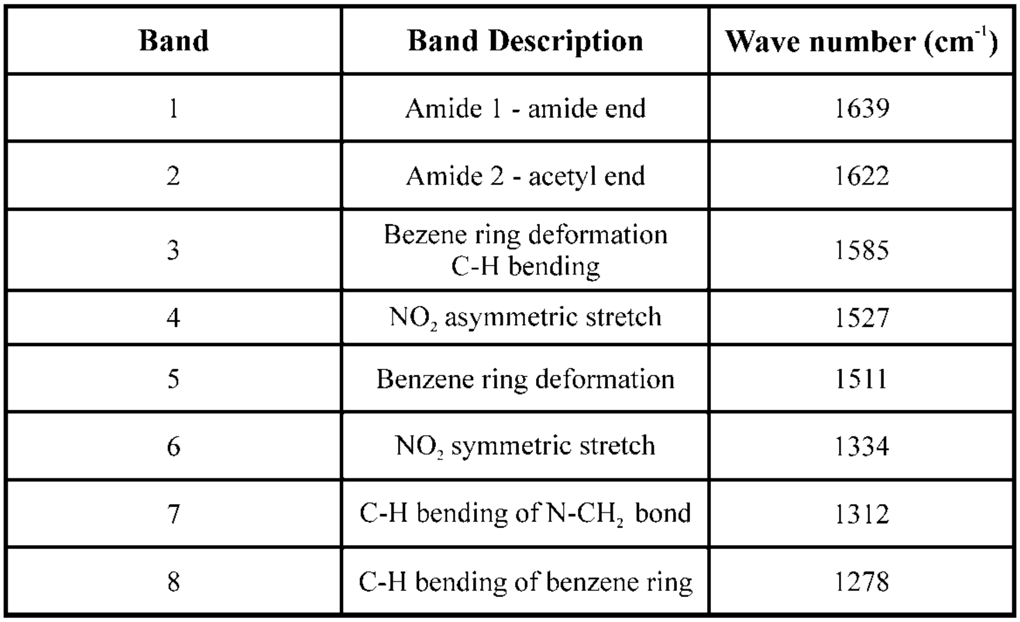

Band	Band Description	Wave number (cm^{-1})
1	Amide 1 - amide end	1639
2	Amide 2 - acetyl end	1622
3	Bezene ring deformation C-H bending	1585
4	NO_2 asymmetric stretch	1527
5	Benzene ring deformation	1511
6	NO_2 symmetric stretch	1334
7	C-H bending of N-CH_2 bond	1312
8	C-H bending of benzene ring	1278

The two amide bands are those of the amide groups at the amino end (1639 cm^{-1}) and the acetyl end (1622 cm^{-1}) of the peptide and they are denoted as band 1 and band 2, respectively. It should be noted that band 2 is not a normal amide band since the amide N-atom is covalently bonded to the nitrobenzyl group. Bands 4 and 6 arise from the asymmetric and symmetric NO_2 stretch, respectively. Band 7 is the C—H bending vibration in the N—CH_2—ϕ (ϕ: 2-nitrobenzyl moiety). Finally, bands 3, 5, and 8 are assigned to C—H bending vibrations of the benzene ring and benzene ring deformation.

5.3.2 Continuous Irradiation of Backbone-caged Peptide

Compound **A** was exposed to ns laser pulses (355 nm, 20 mJ, 5 ns) at 10 Hz repetition rate for 5 minutes (in steps of 1 minute) and the IR spectra were monitored using a FT-IR spectrometer (see Figure 5.3).

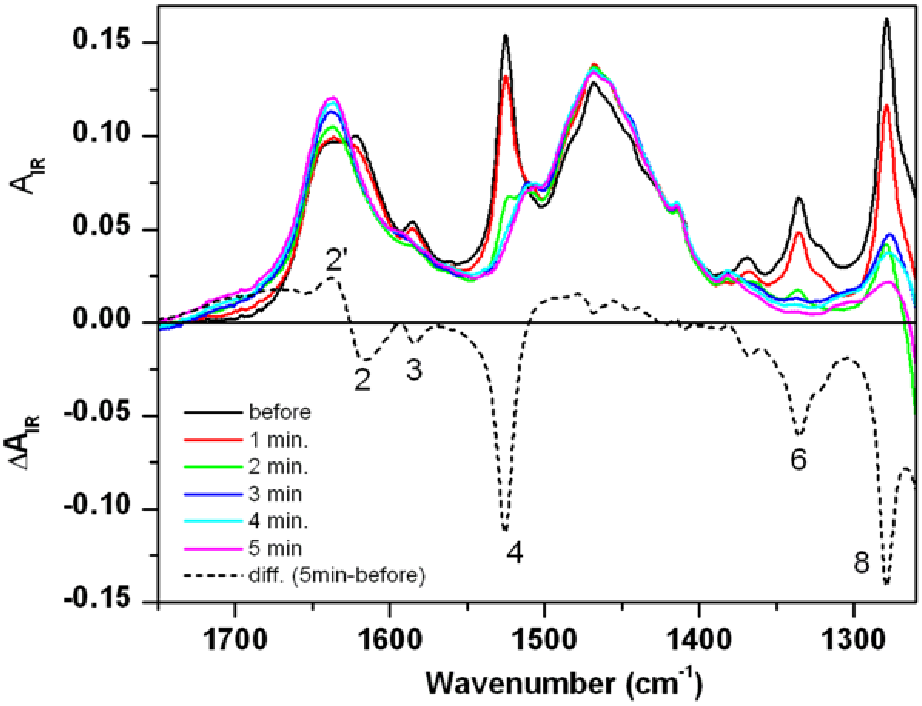

Figure 5. 3: FT-IR spectra of ~10 mg/ml compound A in D_2O/ 5% DMSO-d_6 (56 µm path length) before and during irradiation with Nd:YAG laser pulses (355 nm, 20 mJ, 5 ns, 10 Hz). The dotted curve is the difference IR spectrum obtained by subtracting the spectrum before exposure to UV light from that after 5 minutes of exposure to UV light. The labeled bands are the most sensitive features which change during the photochemical reaction.

The dotted spectrum is the difference between the initial spectrum (before irradiation) and the final spectrum (after 5 minutes of irradiation). The negative and the positive bands are indicative of the disappearance of photoactive species and appearance of newly produced compounds upon photolysis of compound **A**, respectively.

Upon photolysis of compound **A**, band 2 decreased in intensity within two minutes of irradiation. At the same time, band 1 at 1639 cm^{-1} and band 2 (1622 cm^{-1}) merge into a single band at ~1635 cm^{-1} (2′), as shown in Figure 5.3. According to Rhee et al[80], this newly formed band agrees well with the amide I band of the purely synthesized compound **B**. In parallel to this shift of the amide band, the asymmetric and symmetric NO_2 stretch bands (band 4 and 6, respectively) also disappear.

Rhee et al[80] reported that bands 3 and 5 remained nearly unchanged during photolysis of compound **A**. This is because the vibrational modes of the benzene ring are not directly related to the photochemical process. However, our experimental results show that band 3 disappears while band 5 is too weak to allow any definitive conclusion. Unlike Rhee's results where they saw a buildup of the final product, we did not see the formation of the final product in our measurements (Figure 5.1). This is because the ring product precipitates due to the considerable amount of time it takes to record spectra between irradiation.

We determined the quantum yield for the dissociation of the backbone caged peptide based on the probability of molecules excited. First, the absorption cross section (σ) can be expressed by the equation:

$$\sigma = \frac{2.303 * \varepsilon}{N_a} \tag{5.8}$$

where ε is the extinction coefficient which is determined from the absorbance of the sample (0.75) and N_a is Avogadro's number. The probability (P) for a molecule to be excited by one laser pulse can then be calculated from the equation below:

$$P = 1 - e^{(-\sigma N)} \tag{5.9}$$

where N is the number of photons per area. In using equation (5.9), we can estimate that ~99% of the molecules are excited for a laser pulse energy of 20 mJ. This indicates that the molecules in the laser beam are excited at least once by each laser pulse. Nevertheless, not all molecules are in the laser beam at any one time. This was accounted for by comparing the area of the laser spot to the area of the whole sample. We found that each molecule is excited ~22 times per one minute of irradiation at 10 Hz repetition rate.

As shown in the FTIR spectra (Figure 5.3), the photochemical reaction is not completed after one minute of irradiation and near completion after two minutes of irradiation. The reaction process is fully complete after three minutes of irradiation. The reaction outcome for the first irradiation and the second irradiation seem to be in disagreement with each other; this may be due to the fact that parts of the sample were not fully exposed to the laser light during the first irradiation step, even though the sample was moved continuously. Non-irradiated molecules have enough time to diffuse around the cell before the next irradiation step, and even before taking the FTIR spectrum. This is due to the considerable amount of time it takes to measure the FT-IR spectrum, hence the difference between the first and second IR spectra. Taking this into account, one can conclude that a significant fraction of all irradiated molecules have been photolysed after one minute, yielding an estimate for the quantum yield of on the order of a few percent (~ 5%) from the fact that each molecule is excited ~22 times per one minute.

5.3.3 Photolysis Reaction Monitored by TR-IR Spectroscopy

5.3.3.1 Dynamic Measurements and Quantum Yield

Dynamic studies were carried out on compound A at different IR wavelengths with a ns-pulsed Nd:YAG laser (355 nm, 0.6 mJ, 5 ns). The measurements taken on compound **A** in D_2O/DMSO-d_6 are shown in Figure 5.5. The sample was flowed continuously during measurements using a peristaltic pump, ensuring that a fresh sample volume was probed with each laser pulse. If the sample is not flowed, only the simple "temperature jump signal" is observed (see Chapter 3.6.2). The set-up used for nitrobenzyl photolysis is normally used for studying protein folding events after a fast temperature jump, where temperature increase and subsequent cooling of the sample can be monitored by following the corresponding absorbance changes of D_2O (see Chapter 2 and Figure 5.4).

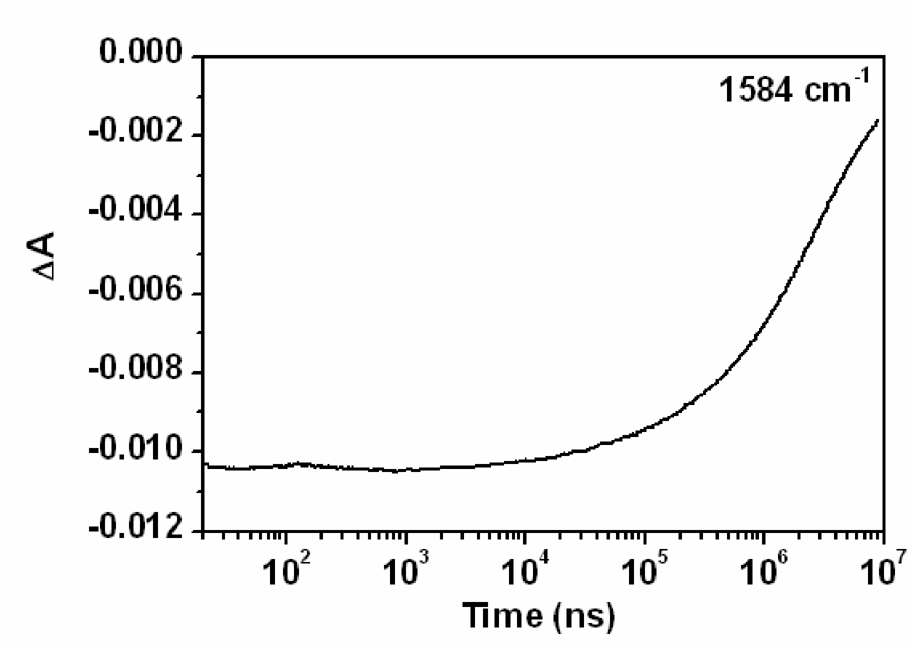

Figure 5. 4: Time dependent absorbance changes of CALNN-NP/D_2O at 1584 cm^{-1} after a temperature jump of ~4 °C from 20 °C (56 µm path length, 10 mg/ml, excitation with laser pulses at 532 nm, 5 ns, 10 Hz),

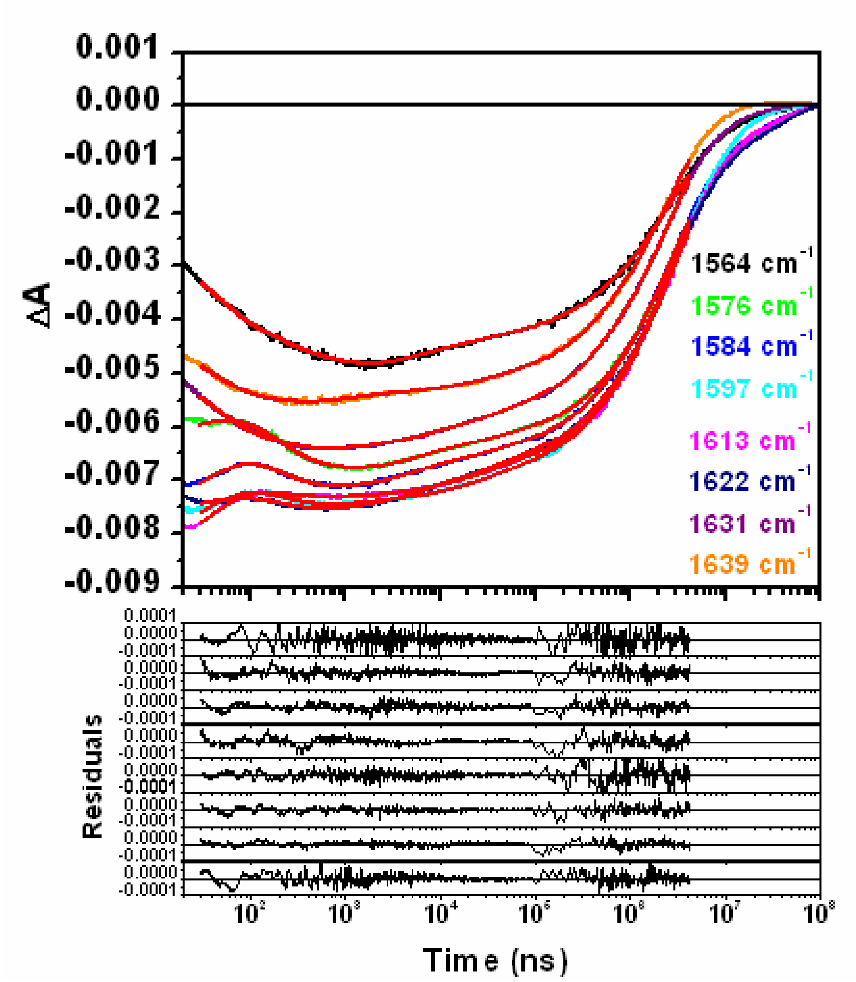

Figure 5. 5: Time dependent absorbance changes for backbone caged peptide A in D_2O, 5% DMSO-d_6 at 8 different wavelengths between 1560 cm^{-1} and 1640 cm^{-1} (56 µm path length, 10 mg/ml, excitation with laser pulses at 355 nm, 5 ns, 10 Hz), scaled as described in section 5.2.4. The smooth red curves on top of the data are the fits in the time range of 30 ns to 4.2 ms to a seven-exponential decay. The residuals of the fits are also shown in the order of increasing wavelengths (top to bottom).

For our dynamic studies on compound **A**, a decrease of the absorbance after excitation is observed at all wavelengths, which then recovers on the microsecond to millisecond time scale. In fact, most of the recovery has the time dependence of cooling as shown in Figure 5.4. Consequently, the absorbance recovery in our measurement (Figure 5.5) can be assigned to be due to the subsequent cooling after heating of our pumped sample volume; the signal corresponds to a temperature increase of ~2 ^{o}C.

The large instantaneous bleach at all wavelengths is indicative of the instantaneous release of heat to the sample within tens of nanoseconds after excitation, in agreement with photoacoustic results (see Chapter 5.3.4). If all the absorbed photon energy is converted to heat, the expected temperature increase can be determined from the equation 5.10:

$$\Delta T = \frac{E}{C_p V_o} \tag{5.10}$$

where E is the absorbed energy (estimated from the laser pulse energy and the absorbance of the sample), C_p is its heat capacity, and V_o is the volume. In using the equation 5.10, the expected temperature jump was calculated to be ~2 ^{o}C in agreement with the observed temperature jump determined from the signal (see discussion above).

A first approach in interpreting the data is to look at the transient spectra (see Figure 5.6). All transient spectra were corrected for underlying D_2O absorbance changes from sample heating by subtracting the absorbance changes at the different times (see Figure 5.6) from A7 (A7 is the amplitude spectrum corresponding to τ_7 which is obtained from the seven-exponential fit (see below) and the amount subtracted decreased with time, i.e. cooling of the sample). The spectra in Figure 5.6 show reasonably well the reaction process. As shown, large absorbance changes are observed within 30 ns.

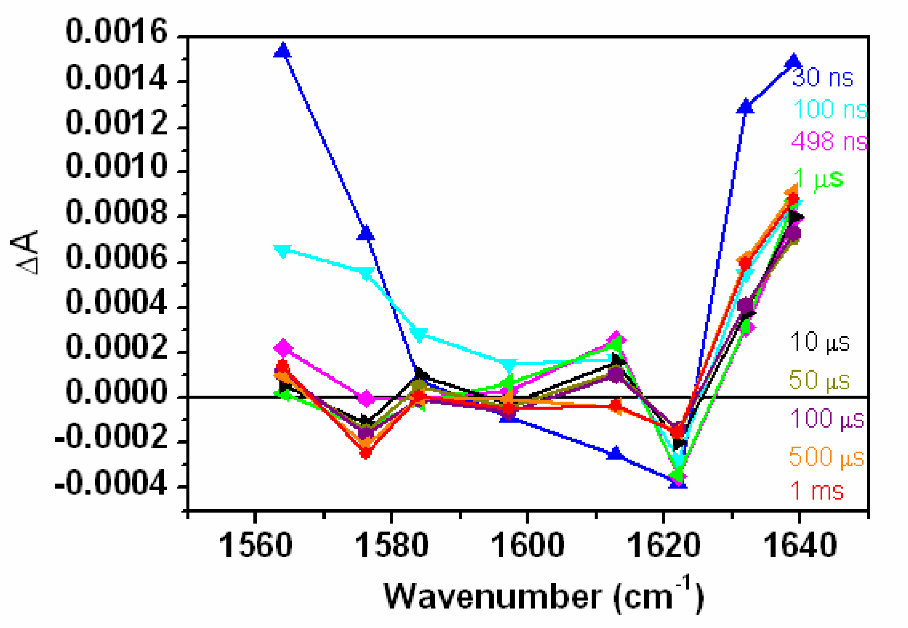

Figure 5. 6: transient difference spectra for selected delay times, corrected for the contribution from solvent heating.

However, the observed absorbance changes within 30 ns do not resemble the expected difference spectrum upon dissociation of the backbone caged peptide. After 100 ns, on the other hand, the amide I difference spectrum has reached more or less its final shape, close to the expected shift upon dissociation of the backbone caged-peptide followed by a slight signal loss after 10 µs. Furthermore, a considerable amount of signal is lost in the benzene ring region of the spectrum (~1580 cm^{-1}) within 1 microsecond, which then remains stable throughout the remaining photochemical process.

The quantum yield for the dissociation of the backbone caged peptide can be obtained by comparison of the size of the signals shown in Figure 5.6 to the size of the signals obtained after completion of the reaction by continuous irradiation (Figure 5.3). For example, a difference between 1617 cm^{-1} and 1639 cm^{-1} difference absorbance (Figure 5.3, dotted curve) indicates that ~30 mOD signal is observed after the reaction is complete. However, a difference of ~1.1 mOD was observed after 100 ns (see Figure 5.6). From equation 5.9, we found that ~99% of the molecules are excited under the conditions used here. Therefore, the quantum yield was estimated to be ~0.03. However, the loss of some signal after 10 µs indicates a slight reduction in the quantum yield.

5.3.3.2 Cooling Correction

Although the results discussed above are valid, interpretation of the fit results obtained from the dynamic traces is even more conclusive (see Figure 5.7). The dynamic traces in Figure 5.5 were fitted globally to a seven exponential function in the time window of 30 ns – 4.2 ms. The time dependent absorbance changes, the seven-exponential fit results and the corresponding residuals are shown in Figure 5.5. For all wavelengths, the seven-exponential fit describes the relaxation process very well. This is evident from the fit residuals. A summary of the time constants obtained from the global fits is shown in Table 5.2.

Table 5. 2 Time constants obtained from global fitting of eight wavelengths (~1560 – 1640 cm^{-1}) and corrections for amplitude spectra (A1-A6).

Amplitude Spectra	Time constants (τ)	Corrections
A1	36 ns	A1-0.1*A7
A2	174 ns	A2-(-0.07*A7)
A3	815 ns	A3-0.01*A7
A4	4 μs	no correction
A5	29 μs	A5-0.09*A7
A6	370 μs	A6-0.07*A7
A7	2.7 ms	-

As mentioned above and discussed in Chapter 2.4.1, complete cooling occurs on the millisecond time scale; however, cooling also affects measurements on the faster time scale and needed to be corrected for. Thus, in order to separate out the effect of cooling from our fit results shown in Figure 5.5, measurements were performed on a sample with nanoparticles in D_2O (CALNN-NP/D_2O) at 1584 cm^{-1} and 1631 cm^{-1} using 532 nm excitation light (Figure 5.4). The sample is typically used for our temperature jump measurements after excitation at 532 nm. The NP/D_2O sample traces were fitted to a seven-exponential function with an offset, using the 7 time constants obtained from the nitrobenzyl fits (Table 5.2), while the amplitudes were allowed to vary freely.

We assume that the slowest component (τ_7 = 2.7 ms) obtained from fitting data on compound **A** is solely due to cooling. This allowed us to determine the cooling contributions for the other amplitudes, since they should have the same ratio to A7 as those obtained in D_2O (see Table 5.2). Finally, these contributions were then subtracted from the amplitude spectra, taking into account the spectral dependence of A7.

5.3.3.3 Amplitude Spectral Analysis

As mentioned above, interpretation of the fit results obtained from the dynamic traces (Figure 5.7) is more conclusive than analysis of the transient spectra (Figure 5.6). Therefore, we analyzed the amplitude spectra obtained from the seven-exponential fits (shown in Figure 5.5) in order to determine how the photochemical reaction progresses.

The amplitude spectra correspond to the disappearance and appearance of old and new species, respectively, and are thus complicated; it is more instructive to look at the difference spectra after each dynamic step has finished and before the next step has started which were calculated from the instantaneous spectrum (see below) by progressively subtracting the corrected amplitude spectra (using the corrections as described in 5.3.3.2. and given in Table 5.2).

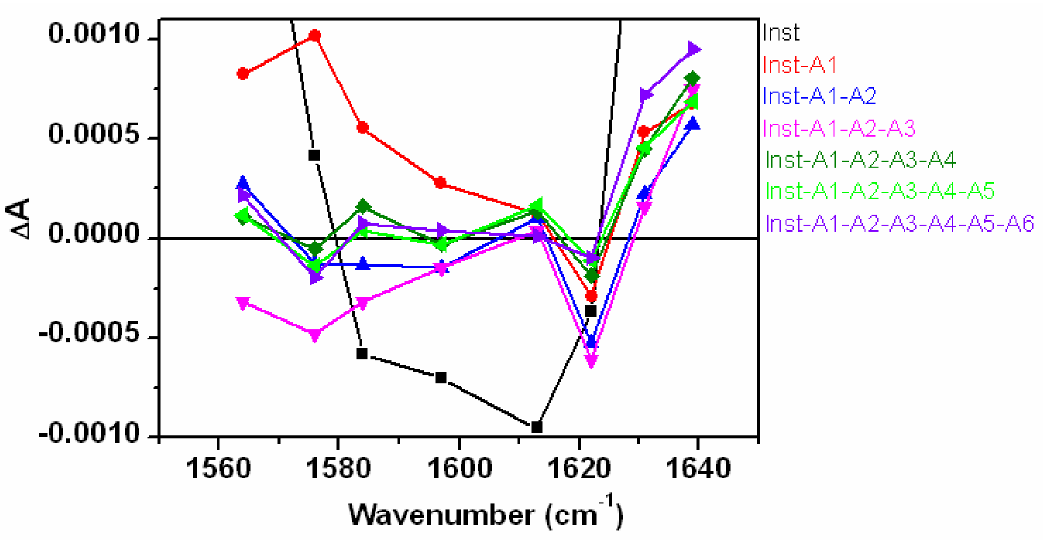

Figure 5. 7: Dynamic difference spectra with respect to wave numbers. The black curve is the instantaneous spectrum (Inst), see text. The colored curves are the results of progressive subtractions of A1-A6 from the Inst spectrum. The red curve is Inst-A1, blue curve is Inst-A1-A2, magenta is Inst-A1-A2-A3, olive green is Inst-A1-A2-A3-A4, lime green is Inst-A1-A2-A3-A4-A5, and purple is Inst-A1-A2-A3-A4-A5-A6.

The instantaneous absorbance change is the fit function extrapolated back to time zero, i.e. the sum of the amplitudes A1 to A7 and the offset. The cooling fits indicate that 1.5*A7 should be subtracted from the instantaneous spectrum in order to correct for the heating of the solvent. As shown in Figure 5.7, the shape is not the shape expected upon dissociation of the backbone caged peptide. It rather reflects the formation of a pre-dissociation intermediate that occurs within the time resolution of our set up which we ascribe to as the formation of the aci-nitro intermediate (**I_1**) (see Scheme 5.3). The formation of this intermediate **I_1** has been shown by several researchers to occur very rapidly (~ps) via intra-molecular hydrogen transfer[162, 167].

The first dynamic spectrum **Inst-A1** (Figure 5.7, red curve), i.e. the product of the first resolvable step, which occurs with a time constant of ~36 ns shows the expected shift of the amide I band upon dissociation accompanied by an absorbance increase in the ~1580 cm^{-1} region of the spectrum. This spectrum is indicative of the dissociation of the peptide and the formation of some intermediate around the benzene ring. As a note, the time constant, ~36 ns, is not expected to be reliable due to the fact that it is close to the time resolution of our setup and therefore, might not be a highly reliable time for the decay of the aci-nitro intermediate.

The second dynamic spectrum **Inst-A1-A2** (Figure 5.7, blue curve) shows a slight further decay of the band at 1622 cm^{-1} and a shift to a lower frequency of the benzene ring vibration. The decay at 1622 cm^{-1} shows the complete dissociation of the back bone caged peptide. As shown in the spectrum, a slight increase is observed in the bleach at 1622 cm^{-1}, indicating that the reaction is not exactly following the fit time constants. This is not surprising since a fit starting at 30 ns is not expected to be reliable since we are approaching the limit of our experimental time resolution, as already pointed out above. On the other hand, the slight increase in the signal could also be due to the noise of our data. All in all, we conclude that the peptide is released within 50 ns.

The next dynamic spectrum **Inst-A1-A2-A3** (Figure 5.7, magenta curve) showed no significant changes in the amide I region, the **Inst-A1-A2-A3-A4** (dark green) spectrum possibly showed slight recombination and the **Inst-A1-A2-A3-A4-A5** spectrum (lime green) showed no significant changes in the amide I region of the spectrum. However, the dynamic spectrum **Inst-A1-A2-A3** demonstrated an absorbance loss in the benzene ring region of the spectrum. The absorbance then recovered in the subsequent spectra and thereafter remained constant throughout the photochemical reaction, indicating that no more reactions are occurring around the benzene ring within our time window.

The next dynamic spectrum in the Figure 5.7, **Inst-A1-A2-A3-A4-A5-A6**, exhibits an increase in the total amide I absorbance on the time scale of ~400 µs and we ascribe this effect to H/D exchange. In their paper, Rhee and coworkers[80] observed that at high pD (pD 11), all IR bands exhibited an instantaneous absorbance change within their time resolution (<3s). At pD 7, the amide I bands showed an instantaneous absorbance change within their time resolution (<3s); however, the authors observed that the aldehyde C=O and N=O bands of the final compound rose slowly on the time scale of ~10 seconds. As the pD is decreased to pD 2, Rhee and coworkers observed that the aldehyde C=O and N=O bands are formed so slowly that they are not yet formed even after ~80 seconds. On the other hand, at pD 2 the authors observed an instantaneous change in the amide I band followed by fast dissociation of the backbone caged peptide, but the same spectra feature as our τ_6 component (see Figure 5.7, **Inst-A1-A2-A3-A4-A5-A6**) is observed, but on the time scale of ~10 seconds. This led us to believe that the increase in the signal on the time scale of ~400 µs is due to H/D exchange.

The rate of exchange for a particular amide proton depends on several factors, e.g. the degree of solvent exposure, temperature, pD and the concentration of the exchange catalyst (OD^- or D^+). For this reason, it is essential for us to consider the evidence for this component to be due to H/D exchange.

It has been observed that at neutral pD, H/D exchange is catalyzed by OD^-[174]. As the pD is decreased, the H/D exchange rate gets slower until ~pD 3 when the reaction mechanism changes and exchange becomes catalyzed by D^+. A further decreases in pD, then accelerates the exchange rate[175]. In the early 1990's, Baldwin et al[174], measured the proton exchange rate of a non-helical peptide. They found that at pD 2, H/D exchange occurred at a rate of 0.1 min^{-1}, i.e. with a half life of $\tau_{1/2}$ = 7 minutes, in agreement with Englander et al[176] where similar results were reported at pD 2. However, their experimental conditions were different to ours and Rhee et al's[80] in that their measurements were taken at 5 ^oC and not ~25 ^oC. The activation energy for the D^+ catalyzed H/D exchange was found to be 12-13 kcal/mol[175, 176], so that at 25 ^oC, the half-life is ~85 seconds, in very good agreement with the pD 2 results reported by Rhee et al[80]

On the other hand, extrapolation of Baldwin's data for neutral pH solution, predicts an exchange rate of 80 min^{-1}[174]. The activation energy for OD^- catalyzed H/D exchange is 16-18 kcal/mol[175, 176], giving a rate of 680 min^{-1} ($\tau_{1/2}$ = 65 ms). The half life predicted from Baldwin's data is two orders of magnitude slower than the time observed in our measurements; this may be due to uncertainties in our measurements: (i) the ~400 microsecond time constant observed in our measurement is somewhat slower. As mentioned above and discussed in Chapter 2.4.1, complete cooling occurs on the millisecond time scale. Thus, we assumed that the slowest component (ms) in our measurement is due to cooling. Our data were then scaled accordingly to correct for the cooling artifacts on the faster time scale. Therefore, any non-cooling dynamics on the millisecond time scale would be normalized away. Thus, the actual time is probably slower than the time observed in our measurement on the ~400 µs time scale, ii) the pD value was not measured for our sample and the solution was not buffered. Thus, it is easily possible that the pD of our solution was > pD 8. As mentioned above, H/D-exchange is OD^- catalyzed, so each unit increase of pD increases the rate of OD^- catalyzed H/D exchange by a factor of ten. In light of these uncertainties, the predicted rate and the observed rate are in reasonable agreement.

A more recent study was carried out by Bai et al[177]. The authors investigated the H/D exchange of several peptides, in particular, compound **C** (see Scheme 5.2) as studied by Rhee et al[80]. From their data, the predicted half life at pD 2 and 25 °C was found to be on the order of a few seconds. Also, the predicted half life at pD7.4 and 25 °C was found to be 170 ms. Again, these results are in very close agreement with the results reported by Rhee et al[80] and us for the rate at which H/D exchange occurred.

Secondly, the spectral change of the amide I band upon H/D exchange is another issue. We observed that the spectral changes of the backbone peptide investigated in our group and by Rhee et al exhibited a total increase in absorbance as well as a small shift in the frequency. When the peptide is in its protonated form (N—H), the amide I band is the result of the carbonyl stretch (C═O) coupled to a C—N stretch and an in-phase N—H bend. These account for 75%, 10%, and 15% of the vibrational energy, respectively. Since deuterium is heavier than hydrogen, the N-D bending vibration is slower and does not couple effectively to the carbonyl stretch vibrations, altering the nature of the amide I vibration. Thus, the amide I band is positioned at lower frequencies (see Chapter 1.2). Also, an increase in the total absorbance would be expected since a larger fraction of the vibration is in the carbonyl stretch since it has the largest dipole moment change.

Theoretical calculations were performed by Jan Kubelka[13] for N-methylacetamide (NMA) (Figure 5.8) and compound **C** using B3LYP/6-311++G**. His calculations confirmed that the deuterated amide I mode (N—D) was more intense than the protonated amide I mode (N—H). For example, Kubelka found that the amide I dipole strength for N—D (0.77 D^2) was greater than N—H (D = 0.72 D^2) for NMA. As clearly shown in the Figure 5.8, the amide 1 band shifts to lower frequency by ~ 10 less cm^{-1} and the total absorbance was increased upon deuteration.

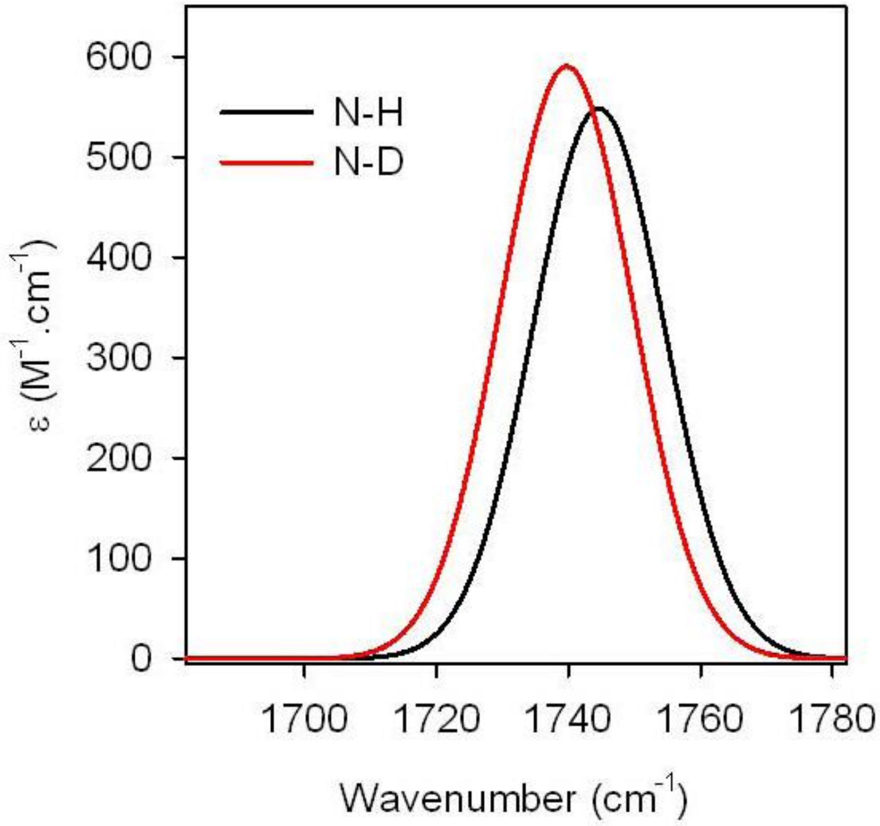

Figure 5. 8: Predicted spectral signature of the amide I band of NMA using B3LYP/6-311++G. The black and red curves are the non-deuterated and deuterated simulated spectra, respectively[14].**

---

[13] Jan Kubleka, Private communication, Department of Chemistry, University of Wyoming

[14] Calculations performed by Jan Kubelka, Department of Chemistry, University of Wyoming

These predicted changes seem in line with the spectral changes obtained on the 100 microsecond time scale at close to neutral pD (results obtained here) and on the 10 s time scale at pD 2[80]. To confirm that an increase in the total amide absorbance upon H/D exchange can yield the observed spectral changes, a simulation calculation was performed in our group (see Figure 5.9), based on the assumption that an increase in the amide I absorbance occurs upon deuteration of the amide; it can be seen from the simulated spectra that H/D exchange is indeed expected to yield spectral changes similar to those observed.

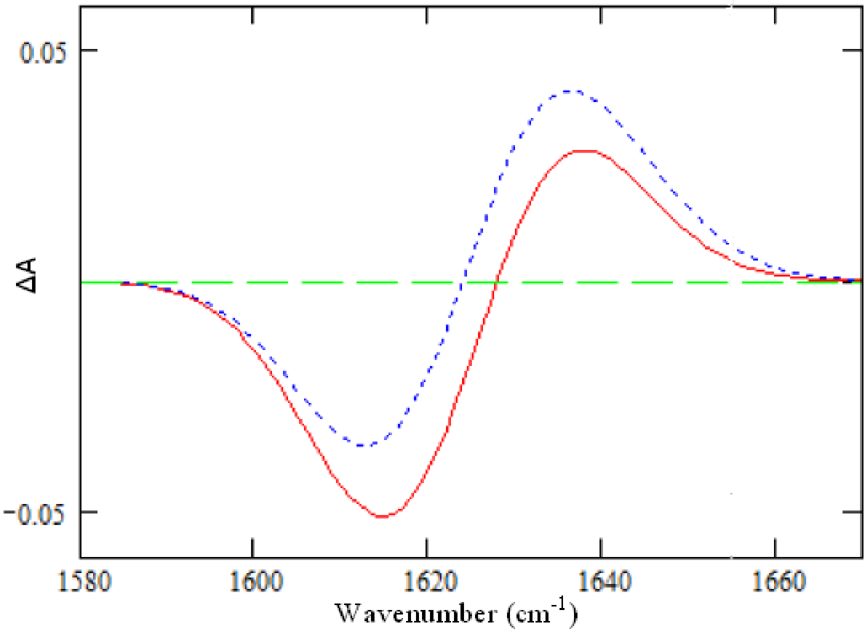

Figure 5. 9: Simulated IR difference spectra of a protonated amide (N—H) and a deuterated amide (N—D) after photoreaction of A. Predicted spectral signature of the amide I band using MathCad[15]. These spectra were simulated using three parameters (position, width and integrated absorbance) with a Gaussian shape. The solid red line shows the expected difference absorbance after photolysis, yielding protonated peptide (N—H) and the blue dotted curve shows the expected difference absorbance after photolysis yielding a deuterated peptide (N—D).

5.3.3.4 Proposed Scheme

On the basis of our time-resolved IR results, the following mechanism can be proposed for compound A (Scheme 5.3, for neutral pD). A detailed study of the

---

[15] Simulations performed by Martin Volk.

photochemical reactivity of a series of 2-nitrobenzyl derivatives has demonstrated that the predominant reaction arises from the singlet excited state[77, 159, 162, 167]. It has been reported that the excited state of a 2-nitrobenzyl compound decayed mostly by internal conversion (IC) to the ground state on the ps-time scale[159, 161]. On the basis of our observation of ~5% quantum yield, we suggest that the remaining ~95% of excited molecules proceed by IC.

After excitation of compound A the aci-nitro intermediate is formed via hydrogen abstraction from CH_2 in the N—CH_2—ϕ (5% yield) on the ps-time scale. As a note, the aci-nitro is the primary "intermediate" of all 2-nitrobenzyl photochemical reactions. It has been suggested that the aci-nitro intermediate has a low pKa of ~3.6 and that it ionizes with a rate constant of ~50 ns in pure water for 2-nitrotoluene[159, 163] and other compounds with larger caged groups[143]. We suggest that for caged peptides, the proton from the aci-nitro intermediate can attack the amide nitrogen before ionization of the aci-nitro intermediate (pathway B, scheme 5.3). This disscociation process is different from the standard mechanism shown in Scheme 5.1, and would explain the observed very fast dissociation of the caged compound (~50 ns). This different and fast mechanism may be due to the amide linkage, whose nitrobenzyl photodissociation has not been studied in detail before.

Upon formation of the aci-nitro intermediate, two isomers of the aci-nitro intermediate are possible, intermediate **I_1-A** (where the amide-N is not in the direction of the aci-nitro proton – pathway A) and **I_1-B** (where the amide-N is in the direction of the aci-nitro proton – pathway **B**) (scheme 5.3). As a note, before I_1, the proton is initially pointing in the direction of N (see **I_1-B**) before the formation of **I_1^-**[162]. After the formation of **I_1^-** and re-deuteration, the deuterated oxygen could be in either of the two isomers (close to N or away from N).

Reaction Pathway A

Upon excitation of compound **A**, the aci-nitro intermediate **I_1-A**[16] is formed. In **I_1-A**, the amide-N is not in the direction of the aci-nitro group, and it is not possible for the proton to attack the amide-nitrogen. The aci-nitro intermediate **I_1-A** follows the standard mechanism proposed by Pelliccioli and Wirz[159, 161]. The authors observed that the aci-nitro intermediate undergoes deprotonation in water at pH 7 with rates of ~50 ns. The deprotonation rate is governed by the pKa of the aci-nitro intermediate depending on the solution conditions. Furthermore, occasional re-protonation (in our case re-deuteration) occurs before the reaction can proceed to the final compound[159, 161] (see Scheme 5.3). As shown in Scheme 5.3, the intermediate **I_1-A** decays to form a cyclic benzisoxazoline intermediate **4**. We suggest that the intermediate **4** is formed on the time scale of ~4 µs, since this is a typical time scale for the decay of the aci-nitro intermediate. The time constant τ_4 reflects some partial recovery of the original amide and the benzylic vibrations (see the difference spectrum **Inst-A1-A2-A3-A4).** The intermediate **4** then decays to form intermediate **5** followed by a slow release of the backbone caged peptide (**B**) and the nitroso compound **C** on the time scale of ~10 s. The latter suggestion is based on the observation that Rhee and coworkers[80] observed a slow rising component at 1635 cm^{-1} on the time scale of ~10 s. As a note, Rhee et al tried to introduce an additional carbonyl aldehyde intermediate and assigned it to the slow rising component observed at 1635 cm^{-1}. However, their assignment cannot be correct, since aldehyde carbonyl frequencies are normally around 1680 cm^{-1} and not 1635 cm^{-1}[162]. Therefore, we suggest that the slow rise in the absorbance at 1635 cm^{-1} observed by Rhee et al reflects cleavage of the backbone caged peptide via pathway A.

Reaction Pathway B

Upon excitation of compound **1,** the intermediate **I_1-B** forms on the ps-time scale[162]. The intermediate **I_1-B** is different from intermediate **I_1-A** in that the amide-N is

---

[16] After excitation of 1, the aci-nitro intermediate is initially protonated. After ionization of the aci-nitro on the time scale of ~50 ns, re-deuteration occurs to form I1-A before the reaction proceeds to the final compound.

close to the aci-nitro proton in **I_1-B**. Therefore, it is possible for the hydrogen from the aci-nitro to attack the amide-N (see arrow in scheme 5.3). Upon hydrogen transfer to the amide-N, cleavage of the backbone caged peptide (**B′**) occurs within ~50 ns. It is important to point out that this is essentially stopped by the deprotonation to **I_1^-**, which is known to occur on the 50 ns-time scale, see above. The peptide then undergoes H/D exchange to form the deuterated peptide (**B**) on the time scale ~360 μs (see discussion above). Concurrent with the cleavage of the backbone caged peptide, a cyclic intermediate is formed (**2**). This intermediate then reacts with D_2O/OD^- (see Scheme 5.3) to form the intermediate **3** on the time scale of ~30 μs. The time constant τ_5 is assigned as the decay of the intermediate 3 due to the fact that there are slight spectral changes in the ring region (see Figure 5.7, **Inst-A1-A2-A3-A4-A5** spectrum). It is possible that the reaction from intermediates **2** to **3** would affect the ring virbration, but not significantly, sine conjugation and ring strain are similar. The intermediate then proceed to the final compound **C** on the time scale of ~10 s. This is based on the slow formation of the final compound observed by Rhee and coworkers[80].

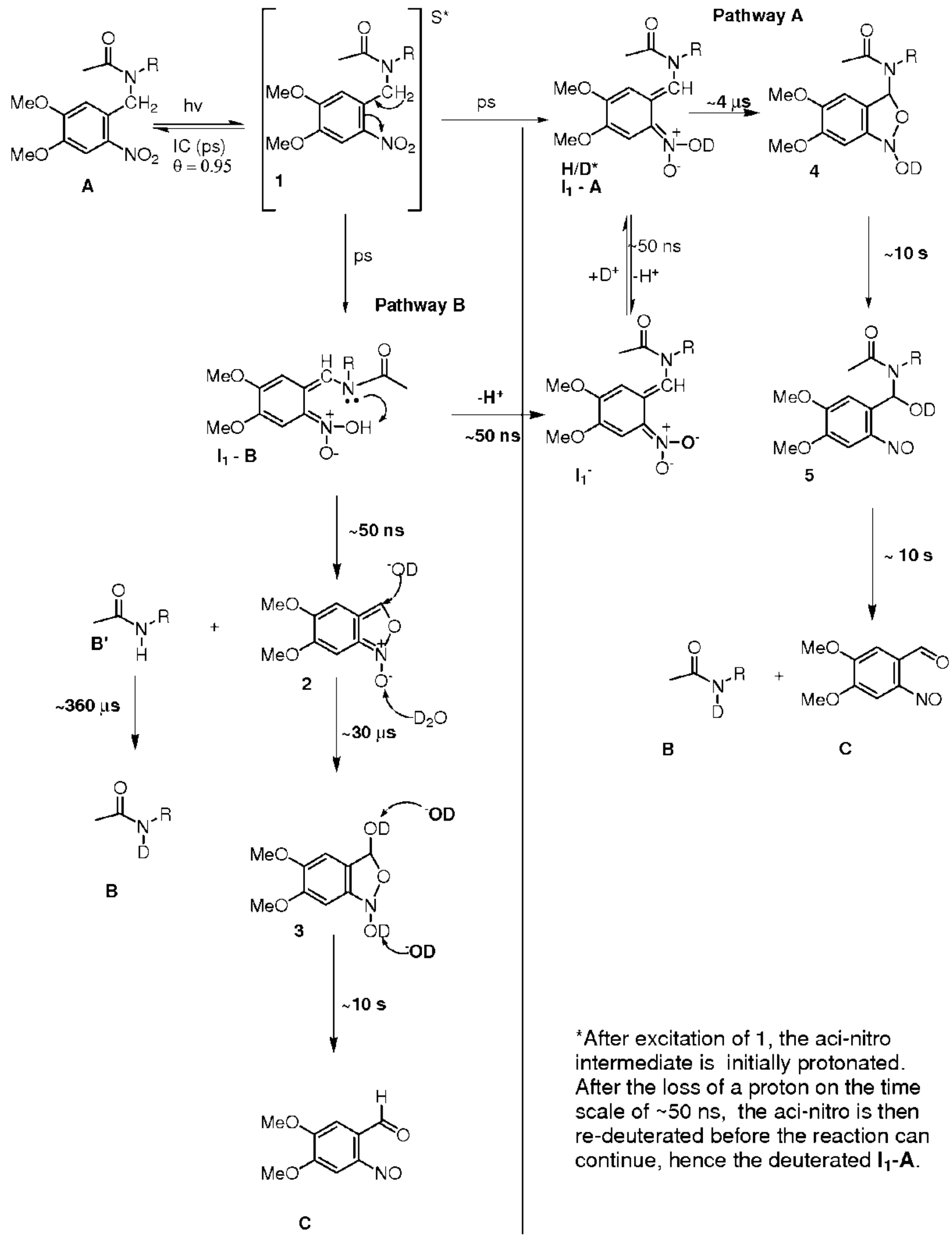

*After excitation of 1, the aci-nitro intermediate is initially protonated. After the loss of a proton on the time scale of ~50 ns, the aci-nitro is then re-deuterated before the reaction can continue, hence the deuterated **I_1-A**.

Scheme 5. 3: Proposed mechanism for photodissociation of compound A at pD 7.

5.3.4 Dissociation Monitored by Photoacoustic Calorimetry

The PAC technique is suitable for studying the dissociation of the backbone caged peptide. This is because PAC monitors the overall volume and enthalpy changes and the rate at which a photoinduced reaction occurs[172] (see Chapter 5.2.5). The PAC measurements were performed by Jaroslava Mikšovská at FIU.

The sample and reference acoustic waves measured at 20 °C are shown in Figure 5.10 for the dissociation of the backbone caged peptide from the nitrobenzyl moiety. As shown in the Figure 5.10, the sample trace overlays in phase with the reference wave, indicating that no additional volume and enthalpy changes were observable between 50 ns and 10 µs. This can be concluded from the absence of the phase shift between the sample and the reference acoustic wave[172, 173]. Furthermore, the amplitude of the sample acoustic wave is slightly smaller than the reference wave due to the presence of the volume and enthalpy changes associated with the dissociation of the caged peptide within 50 ns (see Chapter 5.2.5).

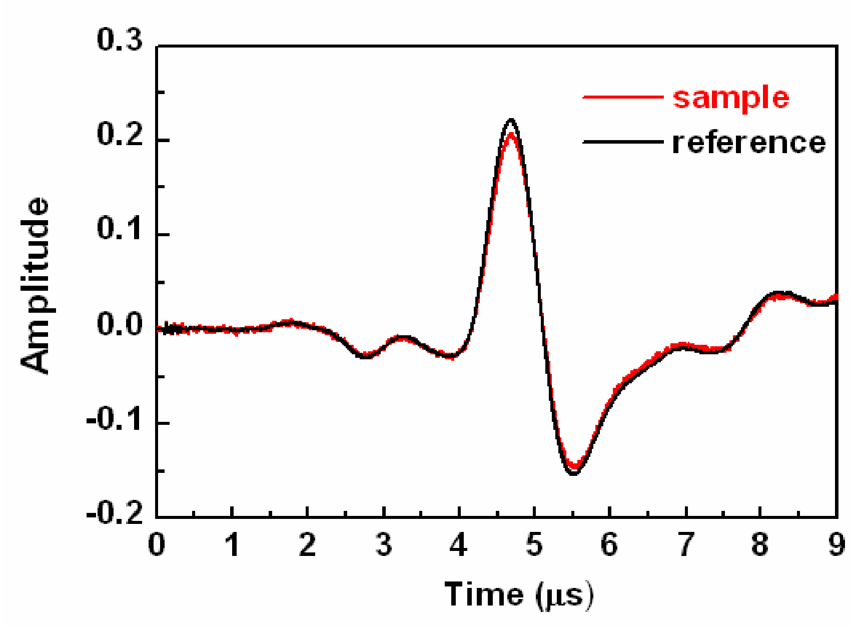

Figure 5. 10: Acoustic traces obtained from the photo-excitation of the compound A and the reference compound, benzaldehyde, measured at 20 °C. The sample acoustic trace is shown in red and the reference acoustic trace is shown in black[17].

---

[17] Results by Jaroslava Mikšovská at Florida International University.

A plot of the ratio of sample and reference acoustic amplitudes as a function of $C_p\rho/\beta$ is shown in Figure 5.11. The quantity of $C_p\rho/\beta$ was varied by changing the temperature between 16 °C and 35 °C.

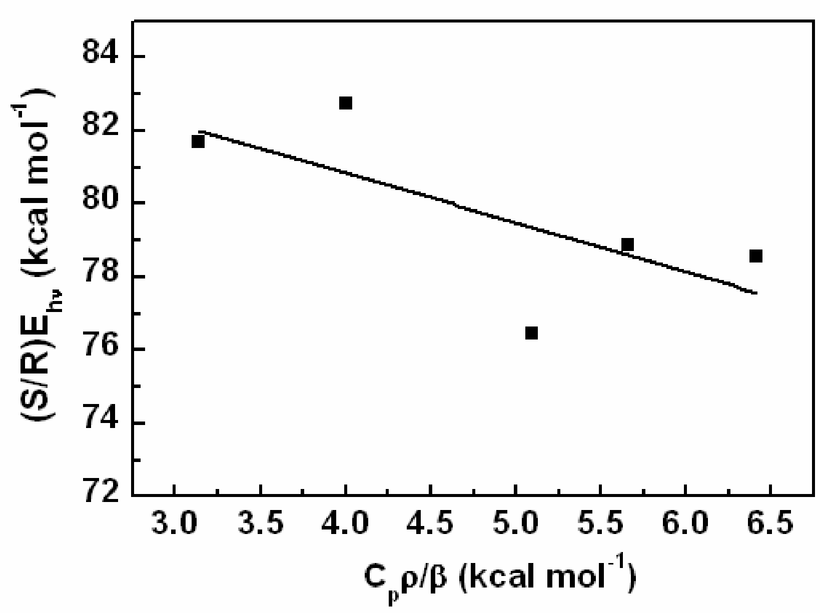

Figure 5. 11: Plot of $(S/R)E_{h\nu}$ vs $C_p\rho/\beta$ for cleavage of the N—C band in compound A

The reaction volume and enthalpy changes associated with the dissociation of the backbone caged peptide from the nitrobenzyl derivative were extrapolated from the linear fit shown in Figure 5.10 using equations 5.5 to 5.7. With a quantum yield of 0.05, the volume and enthalpy changes obtained for the dissociation of the backbone caged peptide are $\Delta V = -28\pm16$ ml/mol and $\Delta H = -11\pm80$ kcal/mol, respectively.

The reaction volume and enthalpy changes measured here for the dissociation of the backbone caged peptide are similar to those determined for the dissociation of caged ATP[178]. The slight difference is probably due to a different extent of solvation of the photo-released groups[178]. Also, the release time measured for the backbone caged peptide is much faster than that of caged ATP, showing that caging through a C—N bond increases the photo-release rate in comparison to photorelease through a C—O.

The release time of ~50 ns observed here for the dissociation of the backbone caged peptide is compatible with our results, even though PAC only gives an upper limit of the release rate. More importantly, the PAC result shows that all energy absorbed by the sample is released within ~50 ns, in agreement with our suggestion of a 95% yield for the reaction via internal conversion back to the ground state.

5.4 Conclusions

It has been suggested that the photolysis of a nitrobenzyl group is useful for triggering protein and peptide secondary structural changes. However, the potential of this method for triggering fast folding processes has yet to be determined. Here, we have investigated the photochemical reaction of a peptide backbone caged by a photolabile linker, 4,5-dimethoxy-2-nitrobenzyl using TR-IR spectroscopy. Our experimental results show that cleavage of the backbone peptide is very fast, on the time scale of ~50 ns, so that the phototriggering technique is valid for observing the fast dynamics of peptides and proteins on the nanosecond/microsecond timescale.

FTIR spectroscopy was used to monitor the changes in the IR bands upon photolysis. Upon irradiation, the symmetric and asymmetric NO_2 stretches disappear and the amide I band of the uncaged peptide appears. We estimate that the quantum yield is on the order of a few percent (~ 5%).

From our TR-IR measurements, the observed quantum yield was ~0.03. Though the quantum yield is relatively small, sufficient photo-release of the backbone caged peptide occurs on the time scale of 50 ns. The release time for the backbone caged peptide determined using PAC also was on the time scale of ~50 ns and is compatible with TRIR results. Because of its rapid photorelease, this technique is useful for triggering even the fastest protein folding processes.

PUBLICATIONS ARISING FROM THIS PhD

Conference Abstract:

R. P. Whynes; M. Gonzales Barriuso; R. Cosstick; M. Volk. *Biophysical Journal*, **2009**, 96, 324a

Publication:

R. Whynes; S. M. Tavender; M. Towrie; M. Volk. *Central Laser Facility Annual Report* **2007/2008**, 169

REFERENCES

[1] N. J. Darby and T. E. Creighton, *Protein Structure, Chapters 1-4, IRL Press, Oxford University Press* **1993**, 1-60.
[2] D. Voet, J. G. Voet and C. W. Pratt, *Fundamentals of Biochemistry, John Wiley & Sons, Inc: New York* **2002**, 78 - 156.
[3] C. Levinthal, *Journal De Chimie Physique Et De Physico-Chimie Biologique* **1968**, *65*, 44-46.
[4] M. Bucciantini, E. Giannoni, F. Chiti, F. Baroni, L. Formigli, J. Zurdo, N. Taddei, G. Ramponi, C. M. Dobson and M. Stefani, *Nature* **2002**, *416*, 507-511.
[5] C. M. Dobson, *Trends in Biochemical Sciences* **1999**, *24*, 329-332.
[6] C. M. Dobson, *Nature* **2003**, *426*, 884-890.
[7] R. J. Ellis and T. J. T. Pinheiro, *Nature* **2002**, *416*, 483-484.
[8] J. A. Hardy and G. A. Higgins, *Science* **1992**, *256*, 184-185.
[9] C. Hetz and C. Soto, *Cellular and Molecular Life Sciences* **2003**, *60*, 133-143.
[10] D. J. Selkoe, *Nature Cell Biology* **2004**, *6*, 1054-1061.
[11] O. B. Ptitsyn, *Protein Engineering* **1994**, *7*, 593-596.
[12] K. A. Dill, *Biochemistry* **1985**, *24*, 1501-1509.
[13] K. A. Dill, *Science* **1990**, *250*, 297-297.
[14] K. A. Dill, S. Bromberg, K. Yue, K. M. Fiebig, D. P. Yee, P. D. Thomas and H. S. Chan, *Protein Science* **1995**, *4*, 561-602.
[15] V. Daggett and A. Fersht, *Nature Reviews Molecular Cell Biology* **2003**, *4*, 497-502.
[16] A. R. Fersht, *Proceedings of the National Academy of Sciences of the United States of America* **1995**, *92*, 10869-10873.
[17] A. R. Fersht, *Current Opinion in Structural Biology* **1997**, *7*, 3-9.
[18] L. Pauling and R. B. Corey, *Nature* **1951**, *168*, 550-551.
[19] S. A. Petty, *University of Liverpool, PhD Thesis* **2004**.
[20] S. Sharma, *University of Liverpool, MPhil Thesis* **2006**.
[21] M. P. Brown and C. Royer, *Current Opinion in Biotechnology* **1997**, *8*, 45-49.
[22] V. Kumar, V. K. Sharma and D. S. Kalonia, *International Journal of Pharmaceutics* **2005**, *294*, 193-199.
[23] J. R. Lakowicz, *Journal of Biochemical and Biophysical Methods* **1980**, *2*, 91-119.
[24] P. A. Thompson, V. Munoz, G. S. Jas, E. R. Henry, W. A. Eaton and J. Hofrichter, *Journal of Physical Chemistry B* **2000**, *104*, 378-389.
[25] J. Sabelko, J. Ervin and M. Gruebele, *Journal of Physical Chemistry B* **1998**, *102*, 1806-1819.
[26] R. W. Woody and M. L. J. a. G. K. A. Jo M. Holt in *Circular Dichroism of Protein-Folding Intermediates*, *Vol. Volume 380* Academic Press, **2004**, pp. 242-285.
[27] R. W. Woody and A. Koslowski, *Biophysical Chemistry* **2002**, *101-102*, 535-551.
[28] S. A. Asher, A. Ianoul, G. Mix, M. N. Boyden, A. Karnoup, M. Diem and R. Schweitzer-Stenner, *Journal of the American Chemical Society* **2001**, *123*, 11775-11781.
[29] S. A. Asher, A. V. Mikhonin and S. Bykov, *Journal of the American Chemical Society* **2004**, *126*, 8433-8440.
[30] R. D. JiJi, G. Balakrishnan, Y. Hu and T. G. Spiro, *Biochemistry* **2006**, *45*, 34-41.
[31] I. K. Lednev, V. V. Ermolenkov, W. He and M. Xu, *Analytical and Bioanalytical Chemistry* **2005**, *381*, 431-437.

[32] I. K. Lednev, A. S. Karnoup, M. C. Sparrow and S. A. Asher, *Journal of the American Chemical Society* **1999**, *121*, 8074-8086.

[33] I. K. Lednev, A. S. Karnoup, M. C. Sparrow and S. A. Asher, *Biophysical Journal* **1999**, *76*, A119.

[34] I. K. Lednev, A. S. Karnoup, M. C. Sparrow and S. A. Asher, *Journal of the American Chemical Society* **1999**, *121*, 4076-4077.

[35] I. K. Lednev, A. S. Karnoup, M. C. Sparrow and S. A. Asher, *Journal of the American Chemical Society* **2001**, *123*, 2388-2392.

[36] A. V. Mikhonin, Z. Ahmed, A. Ianoul and S. A. Asher, *Journal of Physical Chemistry B* **2004**, *108*, 19020-19028.

[37] A. V. Mikhonin and S. A. Asher, *Journal of Physical Chemistry B* **2005**, *109*, 3047-3052.

[38] A. V. Mikhonin and S. A. Asher, *Journal of the American Chemical Society* **2006**, *128*, 13789-13795.

[39] A. V. Mikhonin, S. A. Asher, S. V. Bykov and A. Murza, *Journal of Physical Chemistry B* **2007**, *111*, 3280-3292.

[40] A. V. Mikhonin, S. V. Bykov, N. S. Myshakina and S. A. Asher, *Journal of Physical Chemistry B* **2006**, *110*, 1928-1943.

[41] A. V. Mikhonin, N. S. Myshakina, S. V. Bykov and S. A. Asher, *Journal of the American Chemical Society* **2005**, *127*, 7712-7720.

[42] J. L. R. Arrondo and F. M. Goni, *Progress in Biophysics and Molecular Biology* **1999**, *72*, 367-405.

[43] J. L. R. Arrondo, A. Muga, J. Castresana and F. M. Goni, *Progress in Biophysics and Molecular Biology* **1993**, *59*, 23-56.

[44] E. Goormaghtigh, V. Cabiaux and J.-M. Ruysshaert, *Biochemistry* **1994**, *23*, 329-362.

[45] E. Goormaghtigh, V. Cabiaux and J.-M. Ruysshaert, *Biochemistry* **1994**, *23*, 363-403.

[46] E. Goormaghtigh, V. Cabiaux and J.-M. Ruysshaert, *Biochemistry* **1994**, *23*, 405-450.

[47] P. I. Haris and D. Chapman, *Trends in Biochemical Sciences* **1992**, *17*, 328-333.

[48] M. Jackson, P. I. Haris and D. Chapman, *Biochimica et Biophysica Acta (BBA) - Protein Structure and Molecular Enzymology* **1989**, *998*, 75-79.

[49] M. Jackson and H. H. Mantsch, *Critical Review in Biochemistry and Molecular Biology* **1994**, *30*, 95-120.

[50] F. Siebert and S. Kenneth in *Infrared Spectroscopy Applied to Biochemical and Biological Problems, Vol. 246* Academic Press, **1995**, pp. 501-526.

[51] R. B. Dyer, F. Gai and W. H. Woodruff, *Accounts of Chemical Research* **1998**, *31*, 709-716.

[52] A. Jabs, *A. Homepage of IMB Jena (Image Library of Biological Macromolecules). In http://www.imb-jena.de/ImgLibDoc/ftir/IMAGE_FTIR.html* **1999**.

[53] A. Barth, *Biochimica et Biophysica Acta (BBA) - Bioenergetics* **2007**, *1767*, 1073-1101.

[54] M. Volk, Y. Kholodenko, H. S. M. Lu, E. A. Gooding, W. F. DeGrado and R. M. Hochstrasser, *Journal of Physical Chemistry B* **1997**, *101*, 8607-8616.

[55] E. R. Blout and M. Idelson, *Journal of the American Chemical Society* **1956**, *78*, 497-498.

[56] Chirgadze.Y and Brazhnik.E, *Biopolymers* **1974**, *13*, 1701-1712.

[57] P. Doty, A. M. Holtzer, J. H. Bradbury and E. R. Blout, *Journal of the American Chemical Society* **1954**, *76*, 4493-4494.

[58] R. Gilmanshin, S. Williams, R. H. Callender, W. H. Woodruff and R. B. Dyer, *Biochemistry* **1997**, *36*, 15006-15012.

[59] D. K. Graff, B. Pastrana-Rios, S. Y. Venyaminov and F. G. Prendergast, *Journal of the American Chemical Society* **1997**, *119*, 11282-11294.

[60] C. Y. Huang, J. W. Klemke, Z. Getahun, W. F. DeGrado and F. Gai, *Journal of the American Chemical Society* **2001**, *123*, 9235-9238.

[61] D. F. Kennedy, M. Crisma, C. Toniolo and D. Chapman, *Biochemistry* **1991**, *30*, 6541-6548.

[62] W. K. Surewicz, H. H. Mantsch and D. Chapman, *Biochemistry* **1993**, *32*, 389-394.

[63] J. H. Werner, R. M. Fesinmeyer, N. H. Andersen and R. B. Dyer, *Abstracts of Papers of the American Chemical Society* **2001**, *221*, U395.

[64] S. Williams, T. P. Causgrove, R. Gilmanshin, K. S. Fang, R. H. Callender, W. H. Woodruff and R. B. Dyer, *Biochemistry* **1996**, *35*, 691-697.

[65] P. Doty and J. T. Yang, *Journal of the American Chemical Society* **1956**, *78*, 498-500.

[66] M. C. R. Shastry, S. D. Luck and H. Roder, *Biophysical Journal* **1998**, *74*, 2714-2721.

[67] S. Takahashi, S. R. Yeh, T. K. Das, C. K. Chan, D. S. Gottfried and D. L. Rousseau, *Nature Structural & Molecular Biology* **1997**, *4*, 44-50.

[68] C. K. Chan, Y. Hu, S. Takahashi, D. L. Rousseau, W. A. Eaton and J. Hofrichter, *Proceedings of the National Academy of Sciences, USA* **1997**, *94*, 1779-1784.

[69] B. Gruenewald, C. U. Nicola, A. Lustig and G. Schwarz, *Biophysical Chemistry* **1979**, *9*, 137-147.

[70] G. Schwarz, *Biopolymers* **1968**, *6*, 1263-1277.

[71] G. G. Hammes and P. B. Roberts, *Journal of the American Chemical Society* **1969**, *91*, 1812-1816.

[72] C. M. Jones, E. R. Henry, Y. Hu, C. K. Chan, S. D. Luck, A. Bhuyan, H. Roder, J. Hofrichter and W. A. Eaton, *Proceedings of the National Academy of Sciences, USA* **1993**, *90*, 11860-11864.

[73] T. Pascher, J. P. Chesick, J. R. Winkler and H. B. Gray, *Science* **1996**, *271*, 1558-1560.

[74] J. H. Clark, S. L. Shapiro, A. J. Campillo and K. R. Winn, *Journal of the American Chemical Society* **1979**, *101*, 746-748.

[75] J. Bredenbeck, J. Helbing, A. Sieg, T. Schrader, W. Zinth, c. Renner, R. Behrendt, L. Moroder, J. Wachtveitl and P. Hamm, *Proceedings of the National Academy of Sciences, USA* **2005**, *102*, 2379-2384.

[76] H. S. M. Lu, M. Volk, Y. Kholodenko, E. Gooding, R. M. H. Hochstrasser and W. F. DeGrado, *Journal of the American Chemical Society* **1997**, *119*, 7173-7180.

[77] J. A. McCray and D. R. Trentham, *Annual Review of Biophysics and Biophysical Chemistry* **1989**, *18*, 239-270.

[78] S. R. Adams and R. Y. Tsien, *Annual Review of Physiology* **1993**, *55*, 755-784.

[79] Y. Tatsu, T. Nishigaki, A. Darszon and N. Yumoto, *FEBS Letters* **2002**, *525*, 20-24.
[80] H. Rhee, J. S. Lee, J. Lee, C. Joo, H. Han and M. Cho, *Journal of Physical Chemistry B* **2008**, *112*, 2128-2135.
[81] R. H. Callender, R. B. Dyer, R. Gilmanshin and W. H. Woodruff, *Annual Review of Physical Chemistry* **1998**, *49*, 173-202.
[82] W. A. Eaton, V. Muñoz, S. J. Hagen, G. S. Jas, L. J. Lapidus, E. R. Henry and J. Hofrichter, *Annual Review of Biophysics and Biomolecular Structure* **2000**, *29*, 327-359.
[83] M. Volk, *European Journal of Organic Chemistry* **2001**, 2605-2621.
[84] Q. L. Zhang, L. Wang, Y. X. Weng, X. G. Qiu, W. C. Wang and J. X. Yan, *Chinese Physics* **2005**, *14*, 2484-2490.
[85] P. A. Thompson, W. A. Eaton and J. Hofrichter, *Biochemistry* **1997**, *36*, 9200-9210.
[86] G. S. Jas, W. A. Eaton and J. Hofrichter, *Journal of Physical Chemistry B* **2001**, *105*, 261-272.
[87] E. A. Gooding, A. Pozo Ramajo, J. W. Wang, C. Palmer, E. Fouts and M. Volk, *Chemical Communications* **2005**, 5985-5987.
[88] A. Pozo Ramajo, S. A. Petty, A. Starzyk, S. M. Decatur and M. Volk, *Journal of the American Chemical Society* **2005**, *127*, 13784-13785.
[89] A. Pozo Ramajo, S. A. Petty and M. Volk, *Chemical Physics* **2006**, *323*, 11-20.
[90] T. Wang, D. Du and F. Gai, *Chemical Physics Letters* **2003**, *370*, 842-848.
[91] T. Wang, Y. Zhu, Z. Getahun, D. Du, C. Y. Huang, W. F. DeGrado and F. Gai, *Journal of Physical Chemistry B* **2004**, *108*, 15301-15310.
[92] A. Pozo Ramajo, *University of Liverpool, PhD Thesis* **2006**.
[93] C. Y. Huang, J. W. Kemke, Z. Getahun, W. F. DeGrado and F. Gai, *Proceedings of the National Academy of Sciences, USA* **2002**, *99*, 2788-2793.
[94] W. O. Wray, T. Aida and R. B. Dyer, *Applied Physics B-Lasers and Optics* **2002**, *74*, 57-66.
[95] D. F. Duxbury, *Chemical Reviews* **1993**, *93*, 381-433.
[96] J. Hobley, Y. Kuge, S. Gorelik, M. Kasuya, K. Hatanaka, S. Kajimoto and H. Fukumura, *Physical Chemistry Chemical Physics* **2008**, *10*, 5256-5263.
[97] D. Ben-Amotz and C. B. Harris, *The Journal of Chemical Physics* **1987**, *86*, 4856-4870.
[98] B. Nolting, R. Golbik and A. R. Fersht, *Proceedings of the National Academy of Sciences, USA* **1995**, *92*, 10668-10672.
[99] B. Nolting, R. Golbik, J. L. Neira, A. S. Soler-Gonzalez, G. Schreiber and A. R. Fersht, *Proceedings of the National Academy of Sciences, USA* **1997**, *94*, 826-830.
[100] H. Galster, *pH Measurement. Fundamentals, Methods, Applications, Instrumentation, VCH: Weinheim* **1991**.
[101] C. M. Phillips, Y. Mizutani and R. M. Hochstrasser, *Proceedings of the National Academy of Sciences, USA* **1995**, *92*, 7292-7296.
[102] A. Mokhatari, L. Fini and J. Chesnoy, *The Journal of Chemical Physics* **1987**, *87*, 3429-3435.
[103] V. Sundström, T. Gillbro and H. Bergström, *Chemical Physics* **1982**, *73*, 439-458.
[104] S. A. Petty and M. Volk, *Physical Chemistry Chemical Physics* **2004**, *6*, 1022-1030.
[105] P. K. Jain, X. Huang, I. H. El-Sayed and M. A. El-Sayed, *Accounts of Chemical Research* **2008**, *41*, 1578-1586.

[106] S. Link and M. A. El-Sayed, *Annual Review of Physical Chemistry* **2003**, *54*, 331-366.
[107] R. Maximilian, C. B. Jan, P. Gero von and S. Ulrich, *Small* **2008**, *4*, 607-610.
[108] M. Perner, P. Bost, U. Lemmer, G. von Plessen, J. Feldmann, U. Becker, M. Mennig, M. Schmitt and H. Schmidt, *Physical Review Letters* **1997**, *78*, 2192.
[109] C. Sonnichsen, T. Franzl, T. Wilk, G. v. Plessen and J. Feldmann, *New Journal of Physics: An Institute of Physics and Deutsche Physikalische Gesellschaft Journal* **2002**, *4*, 93.91-93.98.
[110] R. Levy, N. T. K. Thanh, R. C. Doty, I. Hussain, R. J. Nichols, D. J. Schiffrin, M. Brust and D. G. Fernig, *Journal of the American Chemical Society* **2004**, *126*, 10076-10084.
[111] R. Levy, *ChemBioChem* **2006**, *7*, 1141-1145.
[112] M. Brust and C. J. Kiely, *Colloids and Colloid Assemblies* **2004**, 96-119.
[113] M. Brust and C. J. Kiely, *Colloids and Surfaces A: Physicochemical and Engineering Aspects* **2002**, *202*, 175-186.
[114] M. Brust, M. Walker, D. Bethell, D. J. Schiffrin and R. Whyman, *Chemical Communications* **1994**, 801-802.
[115] M. C. Daniels and D. Astruc, *Chemical Reviews* **2004**, *104*, 293-346.
[116] A. C. Templeton, M. P. Wuelfing and R. W. Murray, *Accounts of Chemical Research* **2000**, *33*, 27-36.
[117] R. L. Whetten, M. N. Shafigullin, J. T. Khoury, T. G. Schaaff, I. Vezmar, M. M. Alvarez and A. Wilkinson, *Accounts of Chemical Research* **1999**, *32*, 397-406.
[118] I. H. El-Sayed, X. Huang and M. A. El-Sayed, *Cancer Letters* **2006**, *239*, 129-135.
[119] C. Loo, A. Lowery, N. Halas, J. West and R. Drezek, *Nano Letters* **2005**, *5*, 709-711.
[120] D. Pissuwan, S. M. Valenzuela and M. B. Cortie, *Trends in Biotechnology* **2006**, *24*, 62-67.
[121] A. G. Skirtach, C. Dejugnat, D. Braun, A. S. Susha, A. L. Rogach, W. J. Parak, H. Mohwald and G. B. Sukhorukov, *Nano Letters* **2005**, *5*, 1371-1377.
[122] J. Stehr, C. Hrelescu, R. A. Sperling, G. Raschke, M. Wunderlich, A. Nichtl, D. Heindl, K. Kurzinger, W. J. Parak, T. A. Klar and J. Feldmann, *Nano Letters* **2008**, *8*, 619-623.
[123] X. Huang, I. H. El-Sayed, W. Qian and M. A. El-Sayed, *Journal of the American Chemical Society* **2006**, *128*, 2115-2120.
[124] E. Arbely, T. J. Rutherford, T. D. Sharpe, N. Ferguson and A. R. Fersht, *Journal of Molecular Biology* **2009**, *387*, 986-992.
[125] S. S. Mande, S. Sarfaty, M. D. Allen, R. N. Perham and W. G. Hol, *Structure* **1996**, *4*.
[126] M. M. Garcia-Mira, M. Sadqi, N. Fischer, J. M. Sanchez-Ruiz and V. Muñoz, *Science* **2002**, *298*, 2191-2195.
[127] A. N. Naganathan, U. Doshi and V. Muñoz, *Journal of the American Chemical Society* **2007**, *129*, 5673-5682.
[128] A. N. Naganathan, R. Perez-Jimenez, J. M. Sanchez-Ruiz and V. Muñoz, *Biochemistry* **2005**, *44*, 7435-7449.
[129] P. Li, F. Y. Oliva, A. N. Naganathan and V. Muñoz, *proceedings of the National Academy of Sciences, USA* **2009**, *106*, 103-108.

[130] M. Sadqi, D. Fushman and V. Muñoz, *Nature* **2006**, *442*, 317-321.
[131] N. Ferguson, P. J. Schartau, T. D. Sharpe, S. Sato and A. R. Fersht, *Journal of Molecular Biology* **2004**, *344*, 295-301.
[132] H. Neuweiler, T. D. Sharpe, T. J. Rutherford, C. M. Johnson, M. D. Allen, N. Ferguson and A. R. Fersht, *Journal of Molecular Biology* **2009**, *390*, 1060-1073.
[133] H. Neuweiler, T. D. Sharpe, C. M. Johnson, D. P. Teufel, N. Ferguson and A. R. Fersht, *Journal of Molecular Biology* **2009**, *387*, 975-985.
[134] M. Sadqi, L. J. Lapidus and V. Muñoz, *Proceedings of the National Academy of Sciences, USA* **2003**, *100*, 12117-12122.
[135] N. Ferguson, T. D. Sharpe, P. J. Schartau, S. Sato, M. D. Allen, C. M. Johnson, T. J. Rutherford and A. R. Fersht, *Journal of Molecular Biology* **2005**, *353*, 427-446.
[136] H. Neuweiler, T. D. Sharpe, C. M. Johnson, D. P. Teufel, N. Ferguson and A. R. Fersht, *Journal of Molecular Biology* **2009**, *387*, 975-985.
[137] T. Maniatis, J. Sambrook and E. F. Fristch, *Molecular Cloning: A Laboratory Manual, Cold Spring Harbor Laboratory Publications, Plainview, NY, 2nd Ed.* **1989**.
[138] R. Gilmanshin, R. H. Callender and R. B. Dyer, *Nature Structural Biology* **1998**, *5*, 363-365.
[139] R. Gilmanshin, S. Williams, R. H. Callender, W. H. Woodruff and R. B. Dyer, *Proceedings of the National Academy of Sciences, USA* **1997**, *94*, 3709-3713.
[140] J. Kubelka, W. A. Eaton and J. Hofrichter, *Journal of Molecular Biology* **2003**, *329*, 625-630.
[141] D. M. Vu, J. K. Myers, T. G. Oas and R. B. Dyer, *Biochemistry* **2004**, *43*, 3582-3589.
[142] S. A. Petty and M. Volk, *Biophysical Journal* **2004**, *86*, 617A.
[143] S. Abbruzzetti, M. Carcelli, D. Rogolino and C. Viappiani, *Photochemical and Photobiological Sciences* **2003**, *1*, 796-800.
[144] S. Abbruzzetti, S. Sottini, C. Viappiani and J. E. T. Corrie, *Journal of the American Chemical Society* **2005**, *127*, 9865-9874.
[145] I. Aujard, C. Benbrahim, M. Gouget, O. Ruel, J.-B. Baudin, P. Neveu and L. Jullien, *Chemistry: A European Journal* **2006**, *12*, 6865-6879.
[146] X. Bai, Z. Li, S. Jockusch, N. J. Turro and J. Ju, *Proceedings of the National Academy of Sciences, USA* **2003**, *100*, 409-413.
[147] A. Barth, K. Hauser, W. Maentele, J. E. T. Corrie and D. R. Trentham, *Journal of the American Chemical Society* **1995**, *117*, 10311-10316.
[148] Q. Cheng, M. G. Steinmetz and V. Jayaraman, *Journal of the American Chemical Society* **2002**, *124*, 7676-7677.
[149] J. E. T. Corrie, A. Barth, V. R. N. Munasinghe, D. R. Trentham and M. C. Hutter, *Journal of the American Chemical Society* **2003**, *125*, 8546-8554.
[150] Y. E. Goldman, M. G. Hibberd, J. A. McCray and D. R. Trentham, *Nature* **1982**, *300*, 701-705.
[151] H. Görner, *Photochemical and Photobiological Sciences* **2005**, *4*, 822-828.
[152] D. Gravel, J. Hebert and D. Thoraval, *Canadian Journal of Chemistry* **1983**, *61*, 400-410.
[153] D. Gravel, R. Giasson, D. Blanchet, R. W. Yip and D. k. Sharma, *Canadian Journal of Chemistry* **1991**, *69*, 1193-1200.

[154] M. Gutman and E. Nachliel, *Biochimica et Biophysica Acta (BBA) - Bioenergetics* **1990**, *1015*, 391-414.

[155] Y. V. Il'ichev, M. A. Schwörer and J. Wirz, *Journal of the American Chemical Society* **2004**, *126*, 4581-4595.

[156] T. Milburn, N. Matsubara, A. P. Billington, J. B. Udgaonkar, J. W. Walker, B. K. Carpenter, W. W. Webb, J. Marque, W. Denk, J. A. McCray and G. P. Hess, *Biochemistry* **1989**, *28*, 49-55.

[157] S. K. Nandy, R. S. Agnes and D. S. Lawrence, *Organic Letters* **2007**, *9*, 2249-2252.

[158] A. Patchornik, B. Amit and R. B. Woodward, *Journal of the American Chemical Society* **1970**, *92*, 6333-6335.

[159] A. P. Pelliccioli and J. Wirz, *Photochemical and Photobiological Sciences* **2002**, *1*, 441-458.

[160] D. Ramesh, R. Wieboldt, A. P. Billington, B. K. Carpenter and G. P. Hess, *the Journal of Organic Chemistry* **1993**, *58*, 4599-4605.

[161] M. A. Schwörer and J. Wirz, *Helvetica Chimica Acta* **2001**, *84*, 1441-1458.

[162] M. Gaplovsky, Y. V. Il'ichev, Y. Kamdzhilov, S. V. Kombarova, M. Mac, M. A. Schwörer and J. Wirz, *Photochemical and Photobiological Sciences* **2005**, *4*, 33-42.

[163] J. W. Walker, G. P. Reid, J. A. McCray and D. R. J. Trentham, *Journal of the American Chemical Society* **1988**, *110*, 7170.

[164] F. G. Cruz, J. T. Koh and K. H. Link, *Journal of the American Chemical Society* **2000**, *122*, 8777-8778.

[165] M. Ghosh, I. Ichetovkin, X. Song, J. S. Condeelis and D. S. Lawrence, *Journal of the American Chemical Society* **2002**, *124*, 2440-2441.

[166] W. F. Veldhuyzen, Q. Nguyen, G. McMaster and D. S. Lawrence, *Journal of the American Chemical Society* **2003**, *125*, 13358-13359.

[167] H. A. Morrison, *The Photochemistry of the nitro and nitroso groups. In The chemistry of the Nitro and Nitroso Groups, Wiley, New York, Edited by H. Feuer* **1969**, *1*, 165-213.

[168] J. F. Wootton and D. R. Trentham, *NATO ASI Series C* **1989**, *272*, 277-296.

[169] D. R. Trentham, J. E. T. Corrie and G. P. Reid, *Biophsical Journal* **1992**, *61*, A295.

[170] L. Peng and M. Goeldner, *The Journal of Organic Chemistry* **1996**, *61*, 185-191.

[171] R. Wieboldt, D. Ramesh, E. Jabri, P. A. Karplus, B. K. Carpenter and G. P. Hess, *Journal of Organic Chemistry* **2002**, *67*, 8827-8831.

[172] J. Mikšovská, S. Horsa, M. F. Davis and S. Franzen, *Biochemistry* **2008**, *47*, 11510-11517.

[173] T. Gensch and C. Viappiani, *Photochemical and Photobiological Sciences* **2003**, *2*, 699-721.

[174] C. A. Rohl, J. M. Scholtz, E. J. York, J. M. Stewart and R. L. Baldwin, *Biochemistry* **1992**, *31*, 1263.

[175] S. W. Englander, N. W. Downer and H. Teitelbaum, *Annual Review of Biochemistry* **1972**, *41*, 903.

[176] J. J. Englander, D. B. Calhoun and S. W. Englander, *Analytical Biochemistry* **1979**, *92*, 517.

[177] Y. Bai, J. S. Milne, L. Mayne and S. W. Englander, *Proteins: Structure, Function, and Genetics* **1993**, *17*, 75-86.

[178] J. Choi and M. Terazima, *Photochemical and Photobiological Sciences* **2003**, *2*, 767-773.